8-2009

Fluorescence Polarization of Atomic, Dissociated Atomic, and Molecular Transitions Induced by Spin-Polarized Electron Impact

Jack W. Maseberg
University of Nebraska at Lincoln, maseberg@huskers.unl.edu

Maseberg, Jack W., "Fluorescence Polarization of Atomic, Dissociated Atomic, and Molecular Transitions Induced by Spin-Polarized Electron Impact" (2009). *Theses, Dissertations, and Student Research: Department of Physics and Astronomy*. 6.
http://digitalcommons.unl.edu/physicsdiss/6

FLUORESCENCE POLARIZATION OF ATOMIC, DISSOCIATED ATOMIC, AND MOLECULAR TRANSITIONS INDUCED BY SPIN-POLARIZED ELECTRON IMPACT

by

Jack William Maseberg

A DISSERTATION

Presented to the Faculty of

The Graduate College at the University of Nebraska

In Partial Fulfillment of Requirements

For the Degree of Doctor of Philosophy

Major: Physics and Astronomy

Under the Supervision of Professor Timothy J. Gay

Lincoln, Nebraska

August, 2009

FLUORESCENCE POLARIZATION OF ATOMIC, DISSOCIATED ATOMIC, AND MOLECULAR TRANSITIONS INDUCED BY SPIN-POLARIZED ELECTRON IMPACT

Jack William Maseberg, Ph.D.
University of Nebraska, 2009

Advisor: Timothy J. Gay

Excitation of atoms by spin-polarized electron impact yields fluorescence that can generally exhibit both linear and circular polarization. For experiments where the scattered electrons are not detected, symmetry requires that the electron beam be spin-polarized in order for non-zero circular polarization to be observed. Extensive theoretical and experimental investigations have been performed regarding fluorescence polarizations (Stokes parameters) resulting from spin-polarized electron impact excitation of atoms. Measurement of fluorescence polarization provides insight into the angular momentum coupling that exists in the atomic state of interest. It also enables the measurement of electron spin polarization and experimental benchmarking of theoretical atomic structure calculations.

In an extension of previous atomic investigations, fluorescence polarization from polarized electron impact dissociation and excitation of simple diatomic molecules is considered. Stokes parameters are presented for dissociated atomic transitions in H, D, and N. Rotationally resolved molecular Fulcher band transitions in H_2 and D_2, as well as partially resolved transitions in N_2, are also presented. Non-zero circular polarizations are observed for both the dissociation and molecular excitation processes. For the rotationally resolved molecular transitions, lower circular polarizations are observed for higher values of rotational states.

Preface

Content in Chap. 3 is published in [1].

Content in Chap. 2, Sec. 2.3.4, is published in [2].

Content in Chap. 5, Sec. 5.2.2, is published in [3].

Content from Chap. 5, Secs. 5.1 and 5.2.1 has been submitted for publication in the Journal of Physics: Conference Series (JPCS).

Acknowledgements

I express immense gratitude to my thesis advisor, Prof. Tim Gay, for his continual guidance, good-natured suffering of my struggling intellect, and services in procuring financial support for this work from the National Science Foundation. I also extend my thanks to the other members of my supervisory committee, Profs. Herman Batelaan, Kees Uiterwaal, and Brian Robertson, for their comments and time spent reviewing this dissertation. Similarly, I have benefited from conversations with emeritus Profs. Paul Burrow and Gordon Gallup. I am also grateful for the role my undergraduate mentors, Profs. Kayvan Aflatooni and Itzik Ben-Itzhak, performed in shaping my early scientific career.

I acknowledge my fellow co-workers, Josh Machacek and Jon Reyes, for many useful discussions and assistance with the creation of various figures. My predecessors, Drs. Adam Green, Ben Birdsey, Hasan Al-Khateeb, John Furst, and Ken Trantham, also deserve recognition for illuminating conversations and laboratory assistance. The faculty and technical staff of the Department of Physics and Astronomy at the University of Nebraska-Lincoln are entitled to my appreciation as well. In particular, Bob Kelty of the electronics shop and Les Marquart of the student instrument shop have graciously helped me fabricate apparatus and repair components that I destroyed.

I thank my parents for their support and encouragement to pursue a career in the field of physics. I am indebted to my sisters for their continual assistance with proofreading my documents, and my brother for his ever-inspiring outlook. Finally, I would like to thank my wife for enduring my fiendish behavior this past decade.

Contents

List of Figures

List of Tables

Chapter 1. Introduction

Electron-atom and electron-molecule collisions have proven to be a valuable method with which to explore both classical and quantum mechanical phenomena. Interactions between projectiles (electrons) and targets (atoms or molecules), as well as subsequent interactions within the targets themselves, are manifested in several different ways. For inelastic processes, energy is transfered from the incident electrons to the targets, and this can be observed either by measurement of the scattered projectiles, measurement of residual targets (or target fragments), or both. Targets can be investigated by observation of spontaneous emission; excited atoms and molecules decay to lower energy states by emitting light, and the properties of this light (its intensity, wavelength, and polarization) provide information about the collision dynamics. Historically, the discrete nature of such detected photon spectra played a major role in the development of quantum physics. To this day, these types of experiments remain an active area of research [4].

Many studies have been performed over the past century regarding the properties of light emission from electron-atom, and, to a lesser extent, electron-molecule collisions. The amount, or intensity, of fluorescence measured as a function of incident electron beam energy is referred to as an optical excitation function. A comprehensive article by Heddle and Gallagher [5] illustrates that experimental excitation functions have been acquired from roughly half of the elements in the periodic table. Fluorescence polarization is often measured in conjunction with optical excitation functions. For experiments where unpolarized targets are excited by an unpolarized electron beam, the fluorescence observed perpendicular to the beam can exhibit linear polarization, P_1, with respect to the beam direction. (It is assumed here that the scattered electrons are not detected.) This linear polarization provides information about the relative magnetic sublevel populations in the excited target states [6], and is related to how oblate or prolate the charge cloud is with respect to the electron beam axis.

With the advent of spin-polarized electron sources, even more information could be gleaned from studying the fluorescence resulting from excitation by spin-polarized electron impact. If the photons are detected perpendicular to the electron beam and parallel to the incident electron spin polarization direction, additional polarizations can be observed. These polarizations consist of another linear polarization, P_2 (defined with respect to an axis canted at 45° to the beam axis), as well as the circular polarization, P_3 [7–9]. The polarizations P_2 and P_3 can provide additional insight into spin-dependent collision dynamics [8].

Experiments involving fluorescence polarization and spin-polarized electron impact were first proposed by Farago and Wykes [10, 11], who derived expressions which related the circular polarization of fine-structure-resolved transitions in Hg, Cd, and Zn elements to the value of incident electron spin polarization. Spin-polarized beams are generally partially polarized, and the actual degree of spin polarization, P_e, must be determined. The proposed relations by Farago and Wykes provided an alternative method to traditional Mott polarimetry for the characterization of spin-polarized beams. The first experimental measurement based on this suggestion was conducted by Eminyan and Lampel [12] using zinc atoms. Soon after, P_2 and P_3 measurements were acquired for the case of mercury targets [13]. Gay then pointed out that an unresolved fine-structure multiplet in helium gives a similar relation between the observed fluorescence polarizations and the value of P_e [14], and this group later demonstrated that resolved fine-structure transitions in Ne, Ar, Kr, and Xe could be utilized for optical polarimetry as well [15, 16].

1.1 Implications of fluorescence polarizations

The Stokes parameters (intensity and optical polarizations P_1, P_2, and P_3) are related to the angular momenta of the emitting target. The intensity is related to the optical excitation cross section, and the polarization P_1 is a measure of the alignment of angular momenta (and also the alignment of the charge cloud) with respect to the electron beam axis. Both the intensity and P_1 are independent of P_e. Generally P_1 is non-zero for electron impact excitation, with the notable exception that for excited S atomic states (where $L = M_L = 0$), P_1 is required to be zero if the fine structure is unresolved due to symmetry considerations [9]. A technical consequence of detecting light with non-zero P_1 in a direction perpendicular to the electron beam is that the collected intensity will not be directly proportional to the total intensity due to the angular anisotropy of emission. However, it is well known that the true intensity can be reconstructed from the measured intensity and P_1, and this issue will be further discussed in Chap. 2.

The polarization P_2 is also a measure of alignment, but with respect to an axis tilted by 45° from the beam direction. This polarization, if non-zero, indicates that the charge cloud is aligned and rotated with respect to the electron beam axis. When the scattered electrons are not detected and no external fields are present, P_2 is required to be zero for unpolarized electron impact excitation. When the incoming electrons are spin polarized, however, P_2 may be non-zero. Its value depends on the dynamical processes at work in the collision complex. Bartschat and Blum [7] have demonstrated that exchange excitation of a well-*LS* coupled state cannot provide a finite P_2. For light atoms, two mechanisms can yield non-zero P_2. One mechanism requires exchange excitation to a non-well *LS* coupled state (intermediately coupled with different values of L and S combining to give the same J). The first observation of this sort was completed by Bartschat *et al.* [13]. For the other mechanism, “higher order scattering processes” involving eventual excitation of a well-*LS* coupled state preceded by a period in a non-*LS* coupled intermediate state (or states) should allow for $P_2 \neq 0$ [17]. A search for P_2 due to this situation is presented in Chap. 3, where an experiment is reported regarding the Stokes parameters from a well-*LS* coupled state in helium. The investigated fluorescence received cascade contributions from temporary negative ion resonances, which conceivably allows for a non-zero P_2.

Finally, the spin-dependent polarization P_3 is a measure of the orientation of angular momenta. For spin-polarized electron-impact excitation with no detection of scattered electrons, the orbital angular momentum $\boldsymbol{L}$ of excited states cannot initially be oriented. However, the total angular momentum $\boldsymbol{J}$ can be. (Here the nuclear angular momentum $\boldsymbol{I}$ is ignored.) This orientation of $\boldsymbol{J}$ is due to LS coupling; $\boldsymbol{L}$ and $\boldsymbol{S}$ couple to form the spatially fixed $\boldsymbol{J}$, as shown in the classical vector coupling model in Fig. 1.1a. The initial orientation of $\boldsymbol{S}$ (due to non-zero P_e), when coupled with un-oriented $\boldsymbol{L}$, is thus able to orient $\boldsymbol{J}$. The time average of $\boldsymbol{L}$ also becomes oriented, due to the precession of $\boldsymbol{L}$ and $\boldsymbol{S}$ about $\boldsymbol{J}$. Such precession timescales are typically much shorter than the lifetime of the fluorescing state. Thus, P_3 is obtained for exchange excitation of states by spin-polarized electrons, and can be observed for resolved, or unresolved, fine-structure transitions. However, as was the case for P_1 from atomic S states, the unresolved fine-structure situation requires $L > 0$.

1.2 Moving from atoms to molecules

A relatively large number of experimental and theoretical Stokes parameter investigations have been performed for spin-polarized impact excitation of atoms [9, 18]. Extending these types of measurements to molecular targets offers new challenges with the reward of an improved understanding of molecular angular momentum dynamics. A limited number of such experiments for diatomic targets have already been executed. The Münster group in Germany made the first foray into this field with molecular nitrogen. They measured the Stokes parameters for the N_2 $C\,^3\Pi_u(v' = 0) \rightarrow B\,^3\Pi_g(v'' = 0)$ 337.1 nm band (second positive system) excited by spin-polarized electrons. Interestingly, P_3/P_e was found to be zero within an uncertainty of 2×10^{-3} at an energy corresponding to the cross section maximum [19]. This null result was somewhat surprising, given that triplet transitions in atoms give sizable non-zero circular polarizations.

Following this puzzling nitrogen experiment, our group made measurements using molecular hydrogen. Green *et al.* observed non-zero circular polarization of fluorescence from excited H_2 triplet molecular states produced by spin-polarized electron impact. Values of $P_3/P_e \sim 0.1$ were found for a mixture of unresolved Fulcher band transitions in the 595-605 nm wavelength region [20]. These results represented the first observation of circular polarization from diatomic molecules excited by spin-polarized electrons. Circular polarization was also observed in H_α emission caused by dissociative excitation [20, 21]. Examples of dissociation leading to spin polarized H, D, and N are treated in Chap. 4.

1.2.1 Molecular notation and some Hund's cases

In order to better understand the polarization results (and expectations) for molecular fluorescence, a brief explanation of molecular notation and angular momentum coupling schemes for simple diatomic molecules is in order. Molecular state designations are slightly different from those of atoms, due to the change from spherical to cylindrical symmetry. Molecular states are categorized by the term symbol ${}^{2S+1}\Lambda^{(+/-)}_{\Omega,(g/u)}$, which is preceded by a letter to indicate the electronic state configuration (X for ground states, A, B, C, etc., for excited states of the same multiplicity as the ground state, and a, b, c, etc., for excited states of different multiplicity). The S that appears in the multiplicity superscript represents the total spin quantum number, Λ is the projection of electron orbital angular momentum $\boldsymbol{L}$ along the internuclear axis, and Ω is the projection of the total angular momentum $\boldsymbol{J}$ (excluding nuclear spin) onto the internuclear axis. The values of Λ ($0, \pm 1, \pm 2, \ldots$) are represented as capital Greek letters (Σ, Π, Δ, $\ldots$). Use of a $+$ or $-$ superscript indicates the symmetry of the wave function upon reflection through an arbitrary plane containing the nuclei. For homonuclear molecules, inversion of electron coordinates through the center of the internuclear axis can yield symmetric (g) or antisymmetric (u) states, and this is analogous to atomic parity.

The various molecular angular momenta couple together similarly to the way LS coupling works in atoms. However, the coupling is more complex due to the additional angular momentum $\boldsymbol{R}$ of nuclear rotation. Different coupling schemes were proposed by Hund to aid in choosing a "correct" (maximally diagonal) basis for the Hamiltonian. The cases differ according to the relative interaction strengths (electrostatic, spin-orbit, or spin-rotation) of a given molecular state, and represent limiting scenarios. Hund's cases (a) and (b) will be described here as they are of primary interest to this work.

Figure 1.1f depicts Hund's case (a). The strong electrostatic interaction between the electrons and the nuclei constrains $\boldsymbol{L}$ to precess around the internuclear axis (with projection Λ upon it); spin-orbit coupling then causes $\boldsymbol{S}$ to precess around the internuclear axis as well (with projection Σ—this Σ should not be confused with the Σ corresponding to $\Lambda = 0$ in the term symbol!). The coupling of $\boldsymbol{\Lambda}$ with $\boldsymbol{\Sigma}$ forms $\boldsymbol{\Omega}$, which lies along the internuclear axis. The nuclear rotational momentum $\boldsymbol{R}$ is always perpendicular to the internuclear axis. It couples with $\boldsymbol{\Omega}$ to form $\boldsymbol{J}$, thus $\Omega = \Sigma + \Lambda$ is the projection of J onto the internuclear axis. The vector $\boldsymbol{J}$ has constant magnitude and direction in space, such that a projection M_J can be defined with respect to some laboratory coordinate. The good quantum numbers for this case are S, Σ, Λ, J, Ω, and M_J. Note that R and L are not sharply defined (they are unquantized).

Hund's case (b) is shown in Figs. 1.1b and 1.1c. The strong electrostatic interaction still causes $\boldsymbol{L}$ to precesses around the internuclear axis. However, in this case $\boldsymbol{\Lambda}$ couples to $\boldsymbol{R}$ to form the total orbital angular momentum $\boldsymbol{N}$ because the spin-orbit interaction is relatively weak. The coupling of $\boldsymbol{N}$ and $\boldsymbol{S}$ then creates $\boldsymbol{J}$. The good quantum numbers consist of S, Λ, N, J, and M_J. Note that here Σ and Ω are not quantized.

It should also be mentioned that in older literature the vectors $\boldsymbol{R}$ and $\boldsymbol{N}$ often appear as $\boldsymbol{N}$ and $\boldsymbol{K}$, respectively. Table 1.1 provides a summary of the discussed cases. The

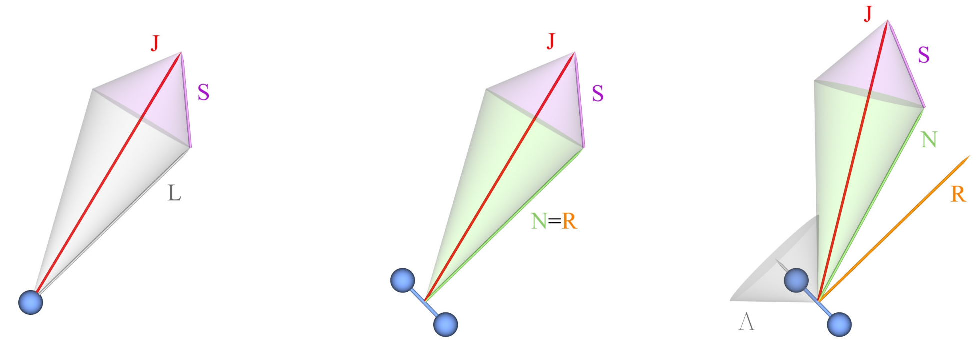

(a) Atomic *LS* coupling. (b) Hund's case (b), $\Lambda = 0$. (c) Hund's case (b), $\Lambda = 1$.

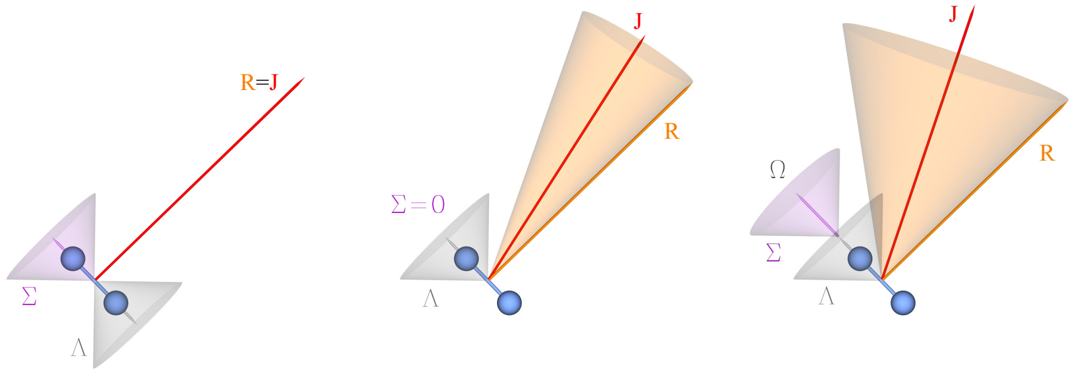

(d) Hund's case (a), $\Omega = 0$. (e) Hund's case (a), $\Omega = 1$. (f) Hund's case (a), $\Omega = 2$.

Figure 1.1: Angular momentum coupling in atoms and molecules. The atomic *LS* coupling scheme is shown in 1.1a. The molecular Hund's case (b) situations are depicted in 1.1b and 1.1c. Hund's case (a) situations are shown in 1.1d, 1.1e, and 1.1f. Note that for singlet states ($S = 0$), the distinction between Hund's cases (a) and (b) disappears and $J = N$.

Table 1.1: Summary of Hund's cases (a) and (b) describing the angular momentum coupling in diatomic molecules.

Hund's case	Good quantum numbers	Relative interaction strengths
(a)	$S, \Sigma, \Lambda, J, \Omega, M_J$	$\Delta E_{el} \gg A\Lambda \gg BJ$
(b)	S, Λ, N, J, M_J	$\Delta E_{el} \gg BJ \gg A\Lambda$

electrostatic interaction between the electrons and charged nuclei is related to the ΔE_{el} term in the Table. The relative importance of this interaction is gauged by ΔE_{el}, which represents the energy splitting between the molecular state of interest and the nearest electronic state with a different value of Λ [22]. For the other interaction strengths shown, A represents the state's spin-orbit constant and B is the rotational constant. Generally light molecules such as H_2 and D_2 conform to Hund's case (b), while larger molecules like N_2 are better described by Hund's case (a), provided that $\Lambda > 0$. Note that states having $\Lambda = 0$ must be in Hund's case (b) because then $A\Lambda = 0$. Similarly, low-valued rotational states in N_2 are usually well described by Hund's case (a), but higher valued rotational states can transition to Hund's case (b) if the BJ term in Table 1.1 surpasses the value of $A\Lambda$ as J becomes large [23].

Using this knowledge of Hund's cases, the mechanism for circular polarization production in molecules can be considered in a similar manner to that in atoms. Comparing Figs. 1.1a and 1.1b, it is apparent that there is a strong similarity between atoms and molecules in excited Σ states. Thus, one would expect that molecules with $S > 0$ should exhibit circularly-polarized fluorescence if excited by spin-polarized electrons. Further, given that J depends on S for all coupling cases shown in Fig. 1.1, it appears that an orientation of S should yield an orientation of J, thus providing for non-zero circular polarization. In this context, the results of the German group led by Hanne are somewhat unexpected. What specific effects could work to eliminate nitrogen's circular polarization, but not that of hydrogen? This question largely motivated this work. In an effort to address this issue, data was acquired with emphasis on rotational isolation of molecular spectral lines. Chapter 5 contains Stokes parameter measurements for such rotationally isolated transitions in H_2, D_2, and N_2 molecules.

Chapter 2. Experimental Apparatus and Data Analysis

The apparatus used to acquire the data presented in this dissertation has been previously discussed [24, 25] and is shown in Fig. 2.1. A brief description is given here, and notable improvements made during the course of this work are discussed. Several procedures and issues related to the operation of the experiment and data acquisition are addressed.

Generally speaking, the apparatus provides a means with which to excite atoms or molecules by spin-polarized electron impact. The intensity and polarization of the resulting fluorescence is observed in a direction perpendicular to the electron beam and parallel to the beam's spin polarization direction. The apparatus comprises a spin-polarized electron source, a beam transport and target gas cell system, and an optical polarimeter.

2.1 Polarized electron source

The polarized electron source has been previously described [24–26], and many of the procedures are also similar to those discussed in Ref. [27]. Photoemission from an unstrained GaAs crystal irradiated with circularly polarized (785 nm) light provides a continuous beam of spin-polarized electrons [28]. Polished Zn doped *p*-type GaAs bulk wafers (0.3 mm thick, $\langle 100 \rangle$ orientation) were obtained from Crystal Specialties, with a typical doping carrier concentration of $\sim 2 \times 10^{19}$ cm^{-3}. In preparation for insertion into the source, a crystal is cut from a wafer such that the rectangular dimensions are approximately 5×18.5 mm. The previous chemical etching procedure (outlined in Ref. [29]) has been abandoned; etching vs. not etching does not appear to affect the spin-polarization or quantum efficiency. The crystal is carefully mounted such that it is "gripped" between the coils of two tungsten springs (0.25 mm diam. tungsten wire is wound on a 1.60 mm diam. cylinder to form right-handed springs which are twisted onto 2–56 stainless steel

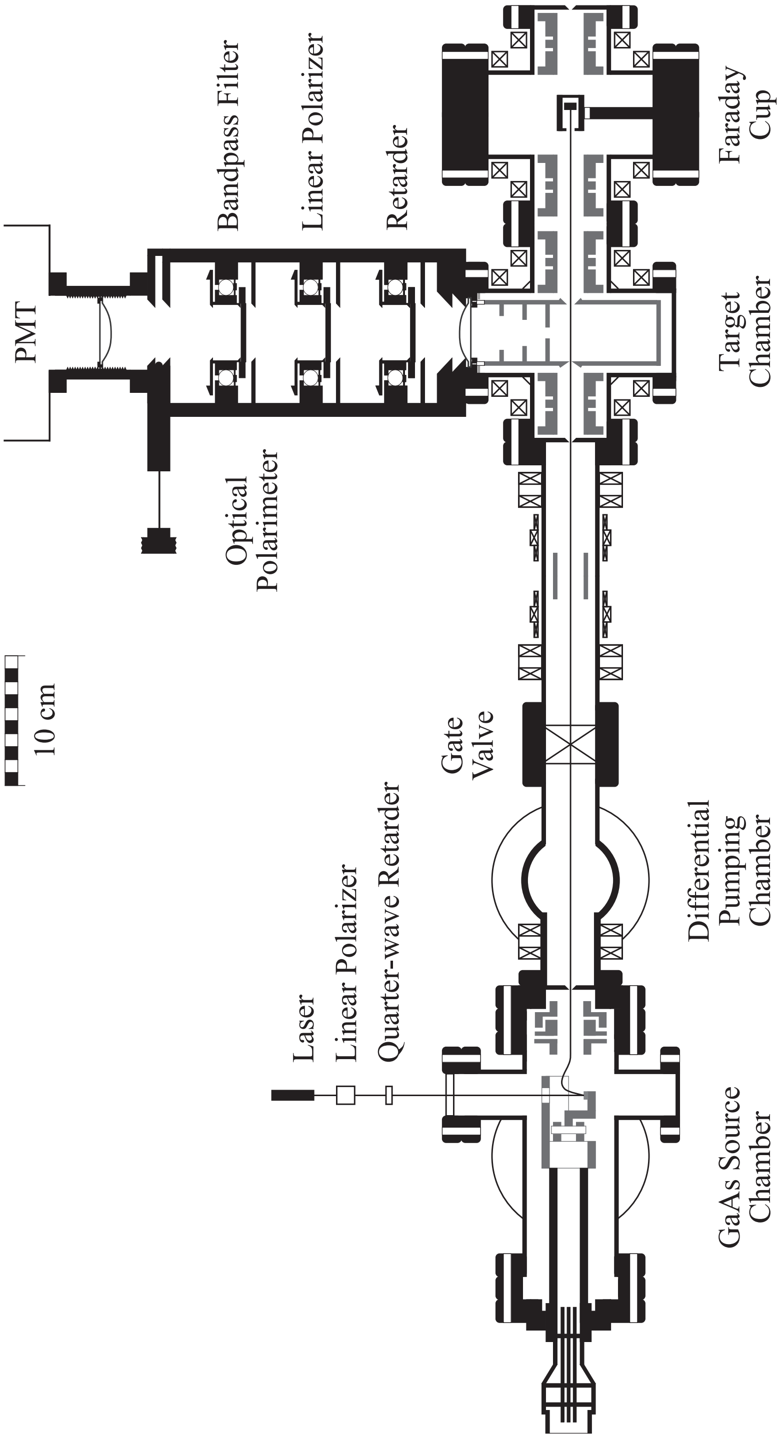

Figure 2.1: Experimental apparatus. The z-axis is taken to be along the electron beam direction, and the y-axis is collinear with the optical path.

mounting screws). Four cesium dispensers (SAES Getters 5G0050 or 5G0055) are also installed in the source chamber such that there exists a line of sight (∼4 cm) between the dispensers and the crystal surface. After the installation of a crystal and fresh cesiators, the chamber is pumped down overnight in preparation for bake-out. An AC current (∼1 A) is applied through the crystal while a DC current of 3.75 A is used to sequentially outgas each cesium dispenser for ∼5 min. each. Note that the crystal heating current value is only approximate as it depends on the exact dimensions of the crystal. The current is adjusted to achieve a visual red-orange color temperature from the crystal. Care must be taken to not overheat the crystal because preferential evaporation of As_2 begins at temperatures above ∼660 °C [28], leaving the crystal with a "frosty" appearance (actual Ga droplets may form in the case of extreme overheating).

After the cesiators and crystal have been outgassed, a heating shroud is assembled and the source chamber is baked at 160 °C for ∼4 days to achieve a base pressure of 5×10^{-11} Torr. This pressure is measured with a nude ionization gauge. The source chamber turbo pump has been replaced by an ion pump (Gamma Vacuum 200T 160 ℓ/s differential diode) and non-evaporable getter (NEG) pump (SAES Getters CapiciTorr CF 35 with C 400 cartridge) combination in order to obtain a cleaner vacuum and to extend the lifetime of photoemission. These alterations have resulted in an improved base pressure (5×10^{-11} vs. 2×10^{-10} Torr). The NEG pump complements the ion pump due to its large pumping speed of H_2 and CO gases (>200 ℓ/s). The ion pump is operated during bake-out and contains its own heating elements. The NEG pump is "activated" at the end of the bake-out cycle by means of its controller, which provides a timed heater current for a duration of 1 hr. After the NEG activation is complete, the bake is terminated.

When the chamber has cooled, surface preparation ("activation") of the GaAs crystal is required to lower the work function so that polarized electrons excited to the conduction band can escape into the vacuum. The source laser used to populate the conduction band is a Thorlabs HL7851G 50 mW single mode 785 nm diode driven by a LDI-800 controller. The laser is passed through a polarizing cube beamsplitter followed by a precision polymer quarter-wave retarder (Meadowlark Optics NQM-050-780, 780 nm) to produce left- or right-circularly polarized light. The actual retardance of the quarter-wave retarder at the 785 nm laser wavelength is 89.1°, and the retarder is mounted in a motorized rotation stage (Standa 8MR150-1). The entire laser optical system is mounted on two translational stages (orthogonal arrangement) above a $2\frac{3}{4}$" Conflat viewport (MDC #450002). The laser spot is centered on the crystal by adjusting the translational stages with the aid of a hand-held mirror (2.5 cm diam.) and a CCD camera or an IR viewer.

To activate the surface, the GaAs is heat cleaned to a red-orange color for 5 min. and then cooled while a current of $\sim$4 A is applied through a cesium dispenser. The crystal is biased to -250 V, and an autoranging picoammeter (Keithley model 485) is connected in series between this bias potential and the crystal to measure the amount of photoemission. After a few hours, a small peak is observed in the photocurrent (see Fig. 2.2). When the crystal becomes overcesiated, the photocurrent begins to decrease. The cesiator current is then turned down (typically to 50% of its initial value), and O_2 (99.998% "ultrahigh purity") is admitted to the source chamber using a Granville-Phillips Series 203 variable leakvalve at partial pressures of $\sim 1 \times 10^{-9}$ Torr. Another peak is then observed that should exhibit a greater maximum than that of the previous one. If admission of O_2 does not lead to greater photocurrent, the solution is to heat clean the crystal again at a higher temperature and/or longer duration. A newly installed crystal can require several heat cleanings before favorable response to O_2 is observed. After admission of O_2 is stopped, the cesiator current is turned back up and the process continues. This "yo-yo" activation procedure [29] is performed until the point of diminishing returns, which usually occurs in 5–10 cycles. The final cesiator current is carefully adjusted (to a smaller value than that used for activation) in order to maintain long-term stability of

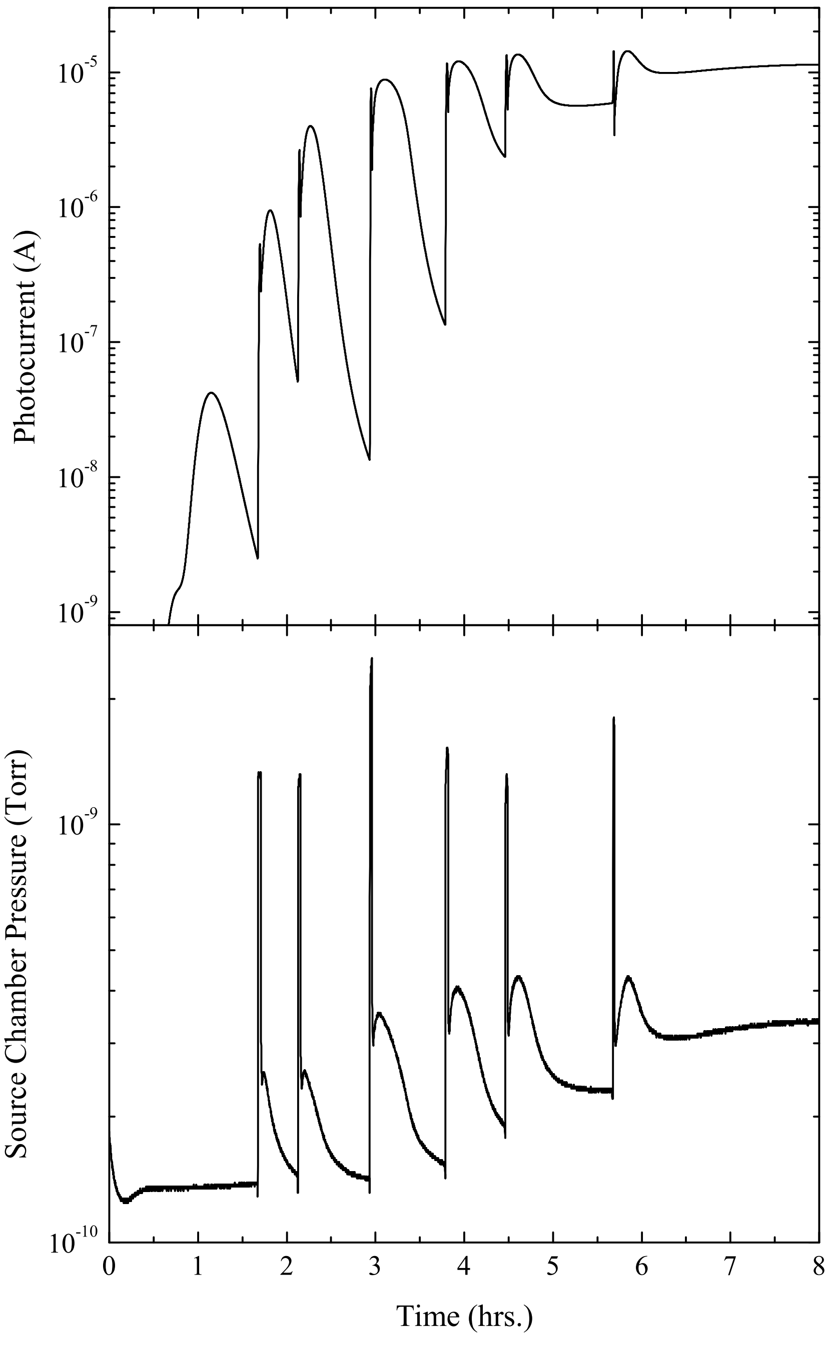

Figure 2.2: Typical “yo-yo” GaAs activation. Top plot shows photocurrent emitted from GaAs crystal as a function of time. Lower plot shows the source chamber pressure as read by an ionization gauge. Broad peaks are due to cesiation; narrow peaks correspond to admission of O_2 into the source chamber.

photoemission.

The source laser is typically operated at a relatively low power of ∼3 mW. (If the laser is set to provide more power, the photocurrent is observed to decay more rapidly.) As shown in Fig. 2.2, photocurrents of ∼10 μA/3 mW are typical. This corresponds to a quantum efficiency (QE, number of outgoing electrons over the number of incoming photons) of ∼0.5%. The electron beam energy distribution width (FWHM) is ∼0.3 eV [1, 30].

The time-decay of photocurrent is believed to be due to sputtering of Cs and O from the activated surface. There is evidence that this sputtering is caused by ion back bombardment [31], meaning that the electron beam creates ions which then impinge upon the activated surface due to its large negative potential. A better vacuum can reduce the rate of sputtering; continuous cessation also combats the problem. The installation of the aforementioned ion and NEG pumps has led to "easier" activations (shorter timescales and less heat cleaning cycles) and has roughly doubled the photocurrent lifetime. Typical lifetimes for the photocurrent are now on the order of 2–5 days. During an experiment, the partial pressure of target gas (H_2, D_2, N_2, or a noble gas) can be as high as 5×10^{-8} Torr, but fortunately these gases are relatively inactive and do not strongly affect photoemission. (However, they likely contribute to ion back bombardment.) Other gases, such as O_2, cannot be used as a target gas because over-oxygenation due to the partial pressure in the source chamber would kill the photocurrent within seconds. Activations performed with (Cs-F) are reported to be more thermally stable than those with (Cs-O_2) [32]. The (Cs-F) activation also seems to resist the effects of vacuum contamination (CO) better than (Cs-O_2), and the reported lifetime is an order of magnitude longer for the case of (Cs-F) vs. (Cs-O_2) [32]. It should also be noted that the Continuous Electron Beam Accelerator Facility at Jefferson Laboratory uses (Cs-NF_3) for activations [31, 33]. This suggests that future investigation regarding the use of (Cs-F or Cs-NF_3) instead of (Cs-

O_2) is warranted to improve the performance of the source. Better differential pumping seems desirable as well to reduce the effect of ion back bombardment.

The actual value of electron beam spin polarization P_e is defined as

$$P_e = \frac{N_\uparrow - N_\downarrow}{N_\uparrow + N_\downarrow}, \tag{2.1}$$

where $N_\uparrow (N_\downarrow)$ represents the number of electrons found with spin $\hbar/2(-\hbar/2)$ by a measurement of spin along the y-axis [8]. To measure the electron spin polarization, the method of optical polarimetry is used [14–16]. Typically, values of ∼0.25 are measured.

2.2 Electron beam transport and target gas cell

Photoemitted electrons from the GaAs crystal undergo a 90° bend in their trajectories due to the electrostatic deflector above the crystal. The crystal potential is held at −250 V, and the deflector potential is typically set near −275 V. The electron spin-polarization is not affected by this deflection, so the electron beam acquires transverse polarization. A Helmholtz coil wrapped around the Conflat flange joining the ion pump with the source chamber is used to help cancel the residual static magnetic field near the crystal region due to the large permanent magnets in the ion pump. A larger Helmholtz coil (65 × 130 cm) surrounds the entire apparatus and is used to cancel the vertical component of the Earth's magnetic field.

After being deflected, the electron beam passes through a three-element Einzel lens in the source chamber. The first and last elements are grounded (0 V), and the middle element is split horizontally to allow for vertical deflection as well as focusing. Typical voltages are −270 V for the upper half and −200 V for the lower half of this split lens element. A differential pumping aperture (∼4 mm diameter) directly follows the lens structure. The next section of the chamber is for differential pumping; the source chamber pressure needs to be isolated from the pressure in the target gas cell. This intermediate chamber is pumped with two Pfeifer-Balzers model TMU 065 turbo pumps (65 ℓ/s). The pumps are mounted facing one another, and due to this opposing arrangement the magnetic fields associated with the spinning turbines tend to cancel each other. There is a single tube electrostatic lens in this chamber, which is typically set at a potential of approximately -150 V. Another differential pumping aperture exists at the end of this section (~4 mm diam.).

The target chamber consists of a $4\frac{1}{2}$" Conflat 6-way cross, which houses the target gas cell and two three-element Einzel lenses. The diameter of the entrance aperture of the cell is 1.0 mm, and the exit aperture diameter is 3.1 mm. The distance between these apertures is ~40 mm. Two gas lines are attached to the target cell. One is connected to an external Granville-Phillips Series 203 variable leak valve that allows gas into the target. The other is connected to an external Granville-Phillips model 275 Convectron gauge for measurement of pressure in the target cell. The Convectron gauge does not provide precise readings at low pressures (10^{-4} Torr range), so a linear calibration is performed using the ionization gauge (Varian Bayard-Alpert type) connected to the target cell chamber. This calibration is performed for each gas species used. All pressure gauges on the apparatus are read with two Granville-Phillips Series 307 controllers. A Seiko Seiki model STP-300 turbo pump (340 ℓ/s) is used to pump the target chamber. A 6" Conflat full nipple lowers the pump 27 cm below the target cross so that the magnetic fields it produces are negligible in the target cell region.

A 4-way $4\frac{1}{2}$" cross directly follows the target chamber, and contains two more sets of three-element Einzel lenses. A Faraday cup was added in this 4-way cross for this work; previous measurements of transmitted beam current were performed by collecting electrons on the Einzel lenses behind the target cell [24, 25], which was not ideal. The stainless steel Faraday cup consists of an inner electrode (12.7 mm diam.) surrounded by a shroud (the outer diameter of the shroud face is 25.4 mm and its inner diameter is 12.7 mm). A 9-volt battery biases the inner electrode to be more positive than the outer shroud, which is connected to 30 V through a Keithley 485 ammeter. Thus current is measured using both electrodes. Another turbo pump (Pfeifer-Balzers model TPU 520 M) helps evacuate the target chamber indirectly, as it is attached to a large chamber not shown in Fig. 2.1. This large chamber, connected to the flange on the right-hand side of Fig. 2.1, houses a Mott polarimeter that was not used for this work.

The voltages applied to the electrodes in the apparatus are manually adjustable by a voltage divider box equipped with several 300 kΩ 10-turn 5 W potentiometers. A Philbrick Researches R-100B power supply provides the rail of the voltage divider box with −300 V (5.1 W). A software-controlled power supply (Sorensen model XT 120-0.5) referenced to the crystal bias voltage (provided by two Agilent E3612A power supplies connected in series) is used to vary the potential difference between the crystal and target cell, thus varying the kinetic energy of the incident electron beam in the target cell.

Various different voltages have been applied to the Einzel lenses immediately before (and after) the target cell. Ultimately, it is desired that for all electron energies the beam be transmitted through the target cell with no loss of current. However, this ideal transmission is not observed in practice for low energies. During the course of this work, the back (or "downstream") 3.1 mm aperture was electrically isolated from the cell to allow for current collection on the face of this aperture (15 mm outer diameter). A Keithley 485 picoammeter is connected between the target cell and the applied target cell potential, and another Keithley 485 is connected between this applied potential and the isolated back aperture. This arrangemtent allows for separate current measurements on the front and back target cell apertures. For low electron beam energies (from ∼5–35 eV) non-zero current is collected on the back aperture. It was hoped that beam tunings could be found to guide the beam through the back aperture without striking it, but this has not proved possible. For low energies the back aperture current can be comparable in magnitude to the transmitted current detected with the Faraday cup. (The electron beam is tuned to maximize the Faraday cup current and minimize the back aperture current.) It has been found that setting all the Einzel lenses surrounding the target cell and Faraday cup to 0 V provides a tuning as good any other.

The fact that the back aperture can obstruct the electron beam does not bode well for proper current normalization of excitation functions. Tunings can be obtained that result in no current reaching the Faraday cup (i.e. all the current is collected on the back aperture), and fluorescence is still measured, meaning the beam exists in the optically sensitive detection region. This suggests that it is advisable to use the sum of the currents collected on the back aperture and Faraday cup for normalization purposes. However, there is still no guarantee that the resulting normalized excitation function will be correct. Given the circumstances, this seems to be an acceptable mode of operation if one accepts that the excitation functions obtained with this apparatus are susceptible to this systematic error. Previous measurements of excitation functions using this apparatus likely suffer from the same issue and are therefore not extremely reliable. Measurement of the light polarizations, however, are not expected to be affected by this issue, because polarizations are defined such that systematic intensity errors of this sort cancel.

2.3 Optical polarimeter

The optical polarimeter depicted in Fig. 2.1 is a light-tight box that houses optical components that are used to measure the the intensity and polarization of fluorescence with wavelength selectivity. A plano-convex BK7 lens (Esco model A620040, 50.8 mm diam., 101.6 mm EFL, 546 nm) tops the target cell and focuses light into the polarimeter such that the rays are approximately parallel. Inside the polarimeter, two rotatable stages with 2" diam. mounts and 1.5" apertures are controlled by stepper motors operated in halfstep mode (400 steps / motor revolution). The motors are connected to the stages by miter gears with a 4:1 ratio, providing an overall ratio of 40 steps / 9° of stage rotation. The lowest rotatable stage typically contains an optical retarder (sheet material from International Polarizer), while the middle stage houses a linear polarizer (sheet material from Rolyn Optics, #65.5305). A narrow bandpass filter is placed in the third stage near the top of the polarimeter and can be tilted (with an axis of rotation perpendicular to the optical axis) for the purpose of angle-tuning the bandpass towards bluer wavelengths [34]. This tilting stage is spring loaded such that it tends to return to its horizontal position, and a string connects the edge of the filter mount to the stepper motor shaft. As the stepper motor turns, the string is wound on the shaft, thus lifting the edge of the filter stage and providing tilt. The three stepper motors are driven by two Arrick Robotics MD2 controllers. The motorized rotation capability of the middle stage and the tilting design of the upper stage were added during the course of this work.

At the top of the optical polarimeter, another BK7 lens (identical to the first) directs the transmitted light onto the GaAs photocathode of a photomultiplier tube (PMT). The PMT is a Hamamatsu model R943-02 and is housed in an Amherst Scientific Corp. model 4501 enclosure. The tube is cooled to −20 °C for low-noise pulse counting, and the tube voltage is held at −1750 V by a Fluke 412B power supply. An Ortec VT120C fast-timing preamplifier (×20 gain, noninverting) accepts signals directly from the PMT. The amplified pulses are then routed to a Phillips Scientific model 6930 discriminator operating in Lower Level Threshold (LLT) mode, with the threshold set to −50 mV. The discriminator output provides TTL pulses with a 100 ns width. Due to this width, the true count rate (TCR) is different from the observed count rate (CR) by [35]

$$TCR = \frac{CR}{1-(10^{-7})CR}. \tag{2.2}$$

This effect is neglected due to the low count rates from the experiment.

The optical system is sensitive to the UVA, visible, and NIR wavelength regions due to the transmission of the lenses and response of the GaAs PMT. The combined detection efficiency of the BK7 lenses and PMT is shown in Fig. 2.3. The use of narrow bandpass filters allows for the isolation of desired atomic or molecular transitions. The following subsections describe techniques used to measure the properties of fluorescence.

2.3.1 Stokes parameters and Mueller matrices

The intensity and polarization of a beam of light can be described by the Stokes parameters. These are represented as a four-component column vector

$$S = I \begin{bmatrix} 1 & P_1 & P_2 & P_3 \end{bmatrix}^T, \tag{2.3}$$

where I is the beam's intensity, P_1 and P_2 are measures of linear polarizations, and P_3 is a measure of circular polarization. The Stokes parameters are subject to the the following constraints: $0 \leqslant I$, $-1 \leqslant P_i \leqslant 1$, and $(P_1^2 + P_2^2 + P_3^2)^{\frac{1}{2}} \leqslant 1$. In this work, emission is observed in a direction perpendicular to the electron beam axis (z-axis) and parallel to the axis of electron spin polarization (y-axis). For this detection geometry, the fluorescence polarizations are defined as

$$P_1 = \frac{I_{0^\circ} - I_{90^\circ}}{I}, \; P_2 = \frac{I_{45^\circ} - I_{135^\circ}}{I}, \text{ and } P_3 = \frac{I_{RHC} - I_{LHC}}{I}, \tag{2.4}$$

where

$$I = I_{0^\circ} + I_{90^\circ} = I_{45^\circ} + I_{135^\circ} = I_{RHC} + I_{LHC}. \tag{2.5}$$

The subscripts in Eqs. (2.4) and (2.5) indicate the polarization filters through which the corresponding intensities are transmitted. The values given in degrees indicate the orien-

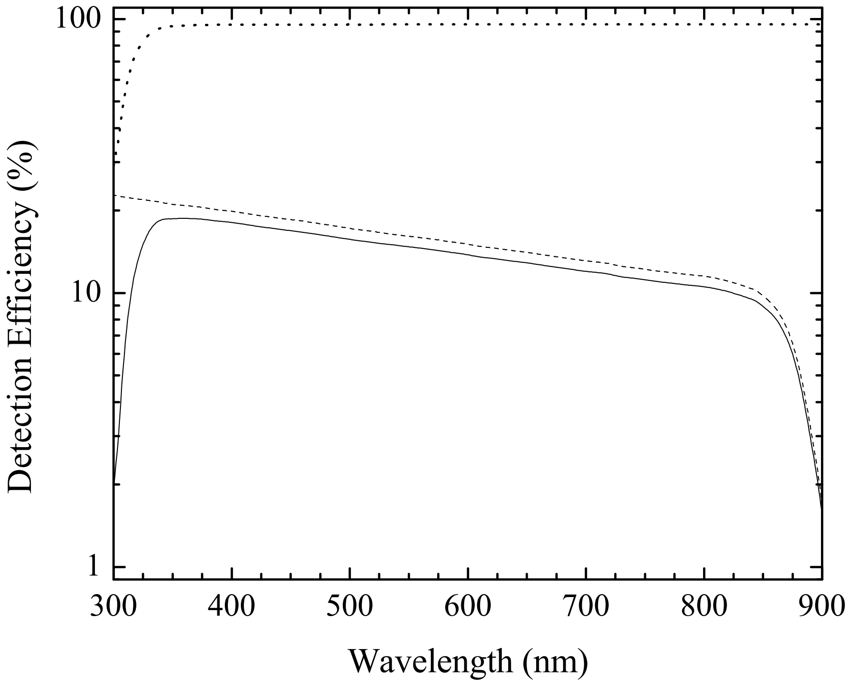

Figure 2.3: Approximate detection efficiency of the optical polarimeter (excluding polarizer, retarder, and bandpass filter elements) as a function of wavelength. The dotted line represents the transmission of BK7 optical glass (∼1 cm thickness), the dashed line represents the QE of the PMT, and the solid line is the square of the dotted line times the dashed line. The efficiency reaches a maximum of ∼19% near 360 nm, and is >10% in the 315–825 nm range and >5% in the 310–880 nm region.

tation of an ideal linear polarizer with respect to the z-axis, while RHC(↻) and LHC(↺) correspond to ideal circular polarizers which pass photons with negative (σ^-) and positive (σ^+) helicities, respectively. Angles are defined in the counterclockwise (CCW) sense when looking into the light beam, with 0° being the direction of electron beam propagation. The P_3 parameter is defined in accordance with classical optics such that its sign is opposite the sign of photon helicity [9], and for this reason $-P_3$ will be reported throughout this work.

Measurement of the Stokes parameters is accomplished by recording intensities transmitted through rotatable optical elements (polarizer or retarder-polarizer combination). These optical elements can be described by Mueller matrices, and matrix multiplication describes the modification of a Stokes vector by a given physical arrangement of optical elements.

The Mueller matrix for a non-ideal linear polarizer described by k is

$$\boldsymbol{LP} = \begin{bmatrix} 1 & k & 0 & 0 \\ k & 1 & 0 & 0 \\ 0 & 0 & \sqrt{1-k^2} & 0 \\ 0 & 0 & 0 & \sqrt{1-k^2} \end{bmatrix}, \tag{2.6}$$

where a preceding factor of $\frac{1}{2}(k_1+k_2)$ has been omitted; for relative Stokes parameter measurements the overall transmission of optical elements need not be taken into account. Here k_1 is the polarizer transmittance observed when pure linearly-polarized light is incident parallel to the pass axis, while k_2 is the transmittance observed when pure linearly-polarized light is incident perpendicular to the pass axis [36]. The k appearing in the the $\boldsymbol{LP}$ matrix is defined as

$$k = \frac{k_1 - k_2}{k_1 + k_2}, \tag{2.7}$$

and can assume values ranging from 0 (no polarizer) to 1 (perfect polarizer). For a linear retarder (wave plate) of retardance δ the Mueller matrix is

$$\boldsymbol{WP} = \begin{bmatrix} 1 & 0 & 0 & 0 \\ 0 & 1 & 0 & 0 \\ 0 & 0 & \cos(\delta) & \sin(\delta) \\ 0 & 0 & -\sin(\delta) & \cos(\delta) \end{bmatrix}. \tag{2.8}$$

For these matrices, the $\boldsymbol{LP}$ pass axis and $\boldsymbol{WP}$ fast axis are taken to be parallel to the z-axis. In order to describe rotations, a rotator matrix acts on some matrix $\boldsymbol{M}$ by $\boldsymbol{R}(-\theta)\boldsymbol{M}\boldsymbol{R}(\theta)$, where

$$\boldsymbol{R}(\theta) = \begin{bmatrix} 1 & 0 & 0 & 0 \\ 0 & \cos(2\theta) & \sin(2\theta) & 0 \\ 0 & -\sin(2\theta) & \cos(2\theta) & 0 \\ 0 & 0 & 0 & 1 \end{bmatrix}. \tag{2.9}$$

This rotation of the element is CCW when looking towards the light source (the same as is done in the lab).

The order of the matrix multiplication is important as the Mueller matrices do not commute. Thus, the Mueller matrices act on the Stokes vector from the left, and the ordering must be done such that the matrix representing the element nearest to the light source is nearest to the Stokes vector. For this work, only the first row element in the resulting Stokes vector, the intensity I', is of interest because this is what is measured. To extract this parameter only, a row matrix

$$\boldsymbol{F} = \begin{bmatrix} 1 & 0 & 0 & 0 \end{bmatrix} \tag{2.10}$$

can be applied from the far left.

2.3.2 Measuring Stokes parameters

Using the results of Sec. (2.3.1), expressions for the measured intensity I' as a function of optical element angle(s) can be generated. For the rotation of a single polarizer,

$$\begin{aligned} I_i' &= \boldsymbol{F} \cdot \boldsymbol{R}(-\alpha_i - \alpha_0) \cdot \boldsymbol{LP} \cdot \boldsymbol{R}(\alpha_i + \alpha_0) \cdot \boldsymbol{S} \\ &= I\left[1 + kP_1 \cos\left(2(\alpha_i + \alpha_0)\right) + kP_2 \sin\left(2(\alpha_i + \alpha_0)\right)\right]. \end{aligned} \tag{2.11}$$

Here $\alpha_i + \alpha_0$ has replaced the θ in Eq. (2.9), and although use of two angles is redundant, it is convenient to consider α_0 as a constant, initial offset angle (typically $\approx$0°), while α_i can represent different angles of rotation. Rotation of a polarizer does not allow measurement of Stokes parameter P_3. To measure I, P_1, and P_2, it is convenient to take four measurements with $\alpha_1 = 0°$, $\alpha_2 = 45°$, $\alpha_3 = 90°$, and $\alpha_4 = 135°$. If only three Stokes parameters are desired (I, P_1, and P_2), then only three different intensity measurements should be required. These measurements could consist of $\alpha_1 = 0°$, $\alpha_2 = 60°$, and $\alpha_3 = 120°$, for example. However, there is no particular advantage to using only three measurements, as the statistical uncertainties are similar for both methods assuming identical data accumulation times. The four-measurement method is typically used as it is conceptually preferred. If P_2 is known or assumed to be zero, only two measurements are needed to measure I and P_1, with $\alpha_1 = 0°$ and $\alpha_2 = 90°$ (or if I and P_2 are desired, $\alpha_1 = 45°$ and $\alpha_2 = 135°$). Table 2.1 gives the statistical (Poisson) uncertainties for these different measurement methods in terms of the total collected counts I_T.

Care must be taken when using the rotating polarizer technique to ensure that the detection system (in this case the combination of bandpass filter and PMT) is insensitive to polarization. To circumvent possible detection polarization dependence, a quarter-wave plate can be placed after the polarizer, with the fast axis offset from the polarizer pass axis by 45°. If the elements are then rotated together the subsequent light always has

Table 2.1: Statistical uncertainties in Stokes parameters related to Eq. (2.11) for different measurement methods (see text) assuming $k = 1$ and $\alpha_0 = 0$. The total collected counts are represented by I_T.

Uncertainty	2-pt method (I and P_1)	2-pt method (I and P_2)	4-pt method (I, P_1, and P_2)
$\Delta I/I$	$(I_T)^{-\frac{1}{2}}$	$(I_T)^{-\frac{1}{2}}$	$(I_T)^{-\frac{1}{2}}$
ΔP_1	$(1-P_1^2)^{\frac{1}{2}}(I_T)^{-\frac{1}{2}}$	—	$(2-P_1^2)^{\frac{1}{2}}(I_T)^{-\frac{1}{2}}$
ΔP_2	—	$(1-P_2^2)^{\frac{1}{2}}(I_T)^{-\frac{1}{2}}$	$(2-P_2^2)^{\frac{1}{2}}(I_T)^{-\frac{1}{2}}$

$P_1 \approx P_2 \approx 0$ and $P_3 \approx 1$, effectively eliminating the problem of polarization sensitivity.

An alternative method that can be used to measure I, P_1, and P_2 is to rotate a retarder (half-wave plate, $\delta = 180°$) in front of a fixed polarizer. For a half-wave plate at angle $\beta_i + \beta_0$ ($\beta_0 \approx 0°$), I, P_1, and P_2 can be measured using $\beta_1 = 0°$, $\beta_2 = 22.5°$, $\beta_3 = 45°$, and $\beta_4 = 67.5°$ with the same statistical uncertainty as the rotating polarizer technique. This method also allows for measurement of all the Stokes parameters (including P_3) if $0° < \delta < 180°$. When a rotatable retarder (at angle $\beta_i + \beta_0$) is followed by a fixed polarizer (at angle α_0),

$$
\begin{aligned}
I_i' &= \boldsymbol{F} \cdot \boldsymbol{R}(-\alpha_0) \cdot \boldsymbol{LP} \cdot \boldsymbol{R}(\alpha_0) \cdot \boldsymbol{R}(-\beta_i - \beta_0) \cdot \boldsymbol{WP} \cdot \boldsymbol{R}(\beta_i + \beta_0) \cdot \boldsymbol{S} \\
&= I \Big\{ 1 + \tfrac{1}{2} k P_1 \Big[\cos(2\alpha_0)\big[(1+\cos\delta) + (1-\cos\delta)\cos\big(4(\beta_i + \beta_0)\big)\big] \\
&\qquad\qquad + \sin(2\alpha_0)\big[(1-\cos\delta)\sin\big(4(\beta_i + \beta_0)\big)\big]\Big] \\
&\quad + \tfrac{1}{2} k P_2 \Big[\cos(2\alpha_0)\big[(1-\cos\delta)\sin\big(4(\beta_i + \beta_0)\big)\big] \\
&\qquad\qquad + \sin(2\alpha_0)\big[(1+\cos\delta) - (1-\cos\delta)\cos\big(4(\beta_i + \beta_0)\big)\big]\Big] \\
&\quad - k P_3 \sin(\delta) \sin\big(2(\beta_i + \beta_0 - \alpha_0)\big)\Big\}.
\end{aligned}
\tag{2.12}
$$

In order to measure all the Stokes parameters using this method, eight measurements can be taken at $\beta_i = 0°$, 22.5°, 45°, 67.5°, 90°, 112.5°, 135°, and 157.5°, or $\beta_i = (i-1) \times 22.5°$ with $1 \leqslant i \leqslant 8$.

Since only four Stokes parameters are being measured, a minimum of four measurements must be made, but here eight are being used. A 4-pt method has been described by Daniels [37] which serves to measure the Stokes parameters with "maximum accuracy". This 4-pt method involves the rotation of both a retarder ($\delta = 120°$) and polarizer, and consists of four measurements taken with the following optical orientations: $\beta = \alpha = C$, $-\beta = -\alpha = C$, $\beta = -\alpha = C$, and $-\beta = \alpha = C$, where the angle $C = \frac{1}{4}\cos^{-1}\left(-\frac{1}{3}\right) \approx 27.4°$. A comparison of statistical uncertainties achieved by the 4-pt and 8-pt methods is given in Table 2.2. For simplicity, the 8-pt method uncertainties pertain only to the $P_1 = P_2 = P_3 = 0$ case, and a choice of $\delta = 126.9°$ gives nearly equal values for $\Delta I/I$, ΔP_1, ΔP_2, and ΔP_3. This choice of δ gives uncertainties in P_1, P_2, and P_3 that are only ∼2% greater than those from Daniels' method, with an increase in $\Delta I/I$ by a factor of ∼1.8 for this null polarization case. When δ is chosen to be 90°, the uncertainty in P_3 is minimized. In practice, values of delta between ∼90° and ∼130° are all acceptable. For this work, the 8-pt method is used over the one offered by Daniels due to its simplicity and the fact that polarization-dependent detection is not an issue because the final polarizer remains fixed.

Stokes parameters can be extracted by fitting Eqs. (2.11) or (2.12) to data acquired by rotating the corresponding optical element in appropriate increments, or, alternatively, the equations can be inverted using a Fourier transform [38]. For the latter method, multiplication of Eq. (2.11) by the sinusoidal and cosinusoidal terms which exist in the

Table 2.2: Statistical uncertainties in Stokes parameters related to Eq. (2.12) for different measurement methods (see text) assuming $k = 1$. For the 8-pt method ($\alpha_0 = \beta_0 = 0°$), δ should be greater than ∼70° for these approximate expressions to remain valid, and for simplicity only the $P_1 = P_2 = P_3 = 0$ case is considered. The total collected counts are represented by I_T.

Uncertainty	Daniels' method ($\delta = 120°$)	8-pt method ($70° < \delta < 180°$)
$\Delta I/I$	$(I_T)^{-\frac{1}{2}}$	$(3 + 2\cos\delta + 3\cos^2\delta)^{\frac{1}{2}}(1 - \cos\delta)^{-1}(I_T)^{-\frac{1}{2}}$
ΔP_1	$(3 - P_1^2)^{\frac{1}{2}}(I_T)^{-\frac{1}{2}}$	$2(2)^{\frac{1}{2}}(1 - \cos\delta)^{-1}(I_T)^{-\frac{1}{2}}$
ΔP_2	$(3 - P_2^2 + \sqrt{3}P_1)^{\frac{1}{2}}(I_T)^{-\frac{1}{2}}$	$2(2)^{\frac{1}{2}}(1 - \cos\delta)^{-1}(I_T)^{-\frac{1}{2}}$
ΔP_3	$(3 - P_3^2 - \sqrt{3}P_1)^{\frac{1}{2}}(I_T)^{-\frac{1}{2}}$	$(2)^{\frac{1}{2}}(\sin\delta)^{-1}(I_T)^{-\frac{1}{2}}$

expression and summing over all optical orientations i (where $\alpha_i = 0°, 45°, 90°$, and $135°$) gives

$$I = \frac{1}{4}\sum_{i=1}^{4} I'_i, \qquad P_1 = \frac{1}{2Ik}\sum_{i=1}^{4} I'_i \cos\left(2(\alpha_i + \alpha_0)\right),$$
$$\text{and} \qquad P_2 = \frac{1}{2Ik}\sum_{i=1}^{4} I'_i \sin\left(2(\alpha_i + \alpha_0)\right). \tag{2.13}$$

Applying this procedure to Eq. (2.12) similarly gives

$$\begin{aligned}
I &= f_0 - \frac{f_1\cos(4\alpha_0) + f_2\sin(4\alpha_0)}{2(1-\cos\delta)(1+\cos\delta)^{-1}}, & P_1 &= \frac{f_1\cos(2\alpha_0) + f_2\sin(2\alpha_0)}{Ik(1-\cos\delta)},\\
P_2 &= \frac{f_2\cos(2\alpha_0) - f_1\sin(2\alpha_0)}{Ik(1-\cos\delta)}, & P_3 &= \frac{-f_3}{Ik\sin(\delta)},\\
f_0 &\equiv \frac{1}{8}\sum_{i=1}^{8} I'_i, & f_1 &\equiv \frac{1}{2}\sum_{i=1}^{8} I'_i \cos\left(4(\beta_i + \beta_0)\right),\\
f_2 &\equiv \frac{1}{2}\sum_{i=1}^{8} I'_i \sin\left(4(\beta_i + \beta_0)\right), \quad \text{and} & f_3 &\equiv \frac{1}{4}\sum_{i=1}^{8} I'_i \sin\left(2(\beta_i + \beta_0 - \alpha_0)\right),
\end{aligned} \tag{2.14}$$

where $\beta_i = (i-1) \times 22.5°$ with $1 \leqslant i \leqslant 8$.

2.3.3 Measuring optical component characteristics

Sections 2.3.1 and 2.3.2 dealt with parameters k and δ, but no mention was made of how these values are obtained for a given optical component. Both of these parameters depend on the optical wavelength (i.e. the interference filter used for an experiment) and, in principle, data provided by the manufacturer can be used to obtain these values. However, it is generally advisable to double check such specifications, as it is plausible that k and δ might change over time. For this work, the values of k and δ were always independently measured.

For measurement of k, two polarizers can be used in conjunction with an unpolarized light source (white LED). The polarizer k value at a given wavelength (interference filter) can be measured by fitting data acquired by rotating one polarizer with respect to the other [38]

$$\begin{aligned} I_i' &= \boldsymbol{F} \cdot \boldsymbol{R}(-\alpha_i - \alpha_0) \cdot \boldsymbol{LP} \cdot \boldsymbol{R}(\alpha_i + \alpha_0) \cdot \boldsymbol{LP} \cdot \boldsymbol{S}\big|_{(P_1=P_2=0)} \\ &= \boldsymbol{F} \cdot \boldsymbol{LP} \cdot \boldsymbol{R}(-\alpha_i - \alpha_0) \cdot \boldsymbol{LP} \cdot \boldsymbol{R}(\alpha_i + \alpha_0) \cdot \boldsymbol{S}\big|_{(P_1=P_2=0)} \\ &= I\left[1 + k^2 \cos\left(2(\alpha_i + \alpha_0)\right)\right]. \end{aligned} \tag{2.15}$$

If the detection system exhibits significant polarization sensitivity, the polarizer closest to the unpolarized light source should be rotated. It is assumed here that the polarizers are of the same material and thus have identical k values.

Measurement of the retardance δ ($0° \leqslant \delta \leqslant 180°$) of a linear wave plate can be accomplished by rotating it between two parallel polarizers with identical, known k values:

$$\begin{aligned} I_i' &= \boldsymbol{F} \cdot \boldsymbol{LP} \cdot \boldsymbol{R}(-\beta_i - \beta_0) \cdot \boldsymbol{WP} \cdot \boldsymbol{R}(\beta_i + \beta_0) \cdot \boldsymbol{LP} \cdot \boldsymbol{S}\big|_{(P_1=P_2=P_3=0)} \\ &= I\left\{1 + k^2\left[\cos^2\left(2(\beta_i + \beta_0)\right) + \cos(\delta)\sin^2\left(2(\beta_i + \beta_0)\right)\right]\right\}. \end{aligned} \tag{2.16}$$

This method is capable of determining the angular locations of the retarder's axes, but does *not* determine if a given axis is fast or slow. If this information is unknown a reference retarder can be used to make these assignments. Combination of retarders with similar δ values will either result in a nonzero-wave plate (fast axes parallel), or a zero-wave plate (fast axes perpendicular) device. If the combined retarders are then rotated between parallel polarizers, the transmitted intensity will be strongly modulated if the fast axes are parallel, and will not be significantly affected if the fast axes are perpendicular. In this way, the correct assignment of fast and slow axes can be performed. If a reference retarder is not available, reflection from a stainless steel mirror can serve as a substitute [39].

When measuring an unknown retarder using this procedure, it is impossible to know whether the fitted retardance is δ or $360° - \delta$, meaning the actual retardance of the device may lie in the range $180° < \delta < 360°$ rather than $0° \leqslant \delta \leqslant 180°$. However, it is acceptable to assume the retardance is in the $0° \leqslant \delta \leqslant 180°$ range even if it is actually not. This is because the Mueller matrix for a retarder described by δ is identical to the matrix obtained by replacing δ with $360° - \delta$, provided this second matrix is rotated by 90°. This rotation corresponds to a perceived interchange of the true fast and slow axes. Using a reference retarder of similar δ to that which was fitted to make the perceived fast and slow axes assignments remains valid. Thus, when fitting Eq. (2.16) to data, only δ values in the range $0° \leqslant \delta \leqslant 180°$ need be considered.

2.3.4 Polarization dependence of optical excitation functions

Section 2.3.2 describes methods to measure the intensity and polarization of light emitted by atoms or molecules detected in an infinitesimal solid angle perpendicular to the electron beam and parallel to the incident electron spin polarization. The intensity recorded in this manner is generally not directly proportional to the total emission, I_{em}, because it depends on the linear polarization of the light, which varies as a function of electron energy. If only the optical excitation function is desired, only the intensity need be measured. However, to remove this dependence on polarization, a polarizer is typically set at the magic angle (≈54.7°) with respect to the electron beam axis (assuming light is collected perpendicular to the electron beam). The existing literature for the derivation of the magic angle value assumes this polarizing element is perfect ($k = 1$). The following derivation (published in [2]) gives an expression for the magic angle that accounts for the use of an imperfect polarizer ($0 < k < 1$).

The fluorescence radiation from an atomic or molecular source is modeled by three

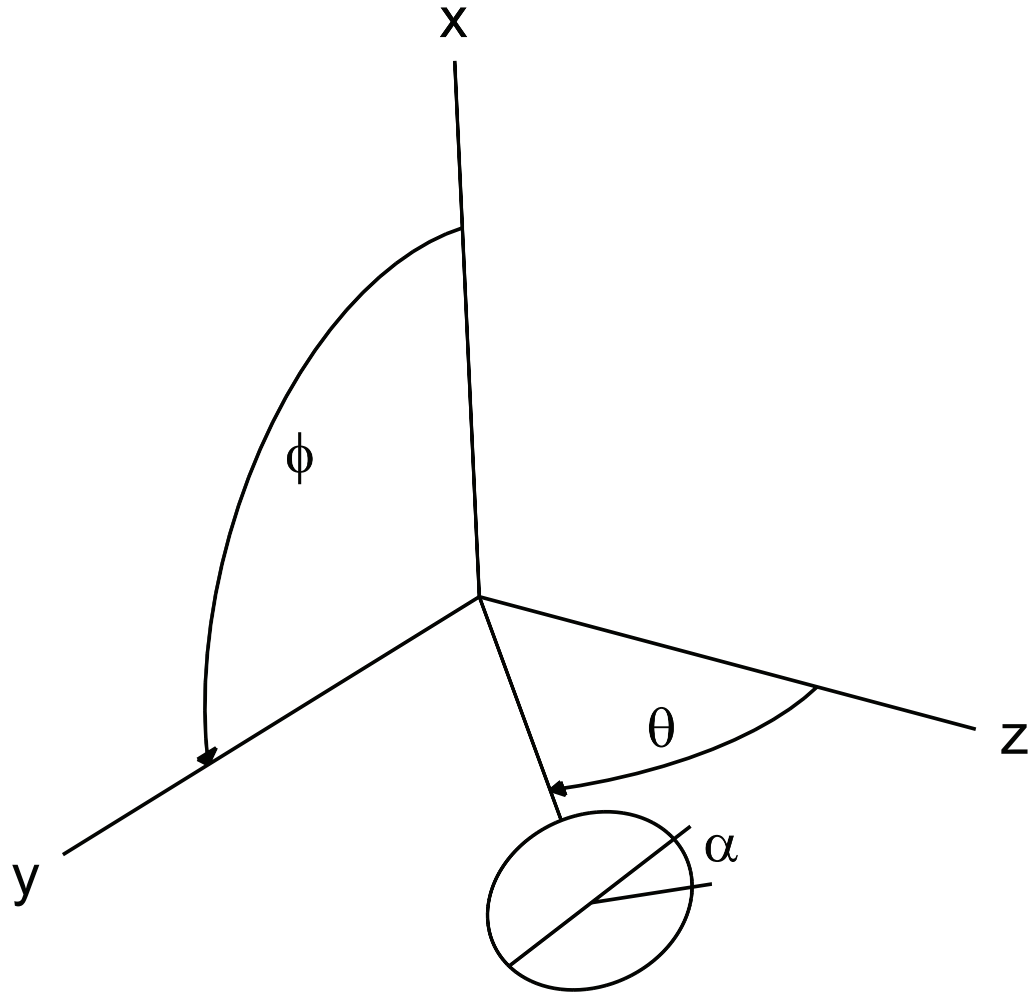

Figure 2.4: Coordinate system for a light source characterized by linear polarization P_1, as defined by Eq. (2.19). Incoherent emitting dipoles along the axes give rise to intensities I_x, I_y, and I_z. By imposing cylindrical symmetry, $I_x = I_y = I_{xy}$. The value of θ for this work is 90°. Light is detected through an imperfect linear polarizer (described by k) at an angle α with respect to the yz-plane.

incoherent dipoles oriented along the coordinates shown in Fig. 2.4 [5, 40–42]. These radiating dipoles give rise to three intensities per unit solid angle: I_x, I_y, and I_z (measured perpendicular to the corresponding dipoles at some fixed radius from the origin). The electron beam is taken to be along the z-axis. Imposing cylindrical symmetry requires that $I_x = I_y = I_{xy}$. It is sufficient to consider only one particular value of ϕ, and $\phi = 90°$ is chosen here. The imperfect analyzing power of a linear polarizer (pass axis oriented at an angle α with respect to the yz-plane) can be described by k such that the first row of its Mueller matrix is represented as

$$\boldsymbol{M} = \tfrac{1}{2}(k_1 + k_2)\begin{bmatrix} 1 & k\cos(2\alpha) & k\sin(2\alpha) & 0 \end{bmatrix}. \tag{2.17}$$

Equation (2.17) is merely the first row of $\boldsymbol{R}(-\alpha)\cdot\boldsymbol{LP}\cdot\boldsymbol{R}(\alpha)$ from Sec. 2.3.1, but the $\frac{1}{2}(k_1 + k_2)$ factor has not been omitted in the $\boldsymbol{LP}$ matrix definition here. The intensity transmitted through the polarizer for some detection angle θ and polarizer orientation α is

$$\frac{dI(\theta,\alpha)}{d\Omega} = \tfrac{1}{2}(k_1 + k_2)\Big\{I_z \sin^2(\theta)\left[1 + k\cos(2\alpha)\right] + I_{xy}\cos^2(\theta)\left[1 + k\cos(2\alpha)\right] + I_{xy}\left[1 - k\cos(2\alpha)\right]\Big\}. \tag{2.18}$$

Using the standard definition of the linear polarization,

$$P_1 = \frac{I_z - I_{xy}}{I_z + I_{xy}}, \tag{2.19}$$

Eq. (2.18) can be expressed as

$$\frac{dI(\theta,\alpha)}{d\Omega} = \tfrac{1}{2}(k_1 + k_2)(I_z + I_{xy})\Big\{1 + P_1 k\cos(2\alpha) - P_1\cos^2(\theta)\left[1 + k\cos(2\alpha)\right]\Big\}. \tag{2.20}$$

The total intensity in the solid angle is the sum of two intensities taken with orthogonal polarizer positions, namely

$$\frac{dI(\theta)}{d\Omega}=\frac{dI(\theta,\alpha)}{d\Omega}+\frac{dI(\theta,\alpha+\pi/2)}{d\Omega}=(k_1+k_2)(I_z+I_{xy})\left[1-P_1\cos^2(\theta)\right]. \tag{2.21}$$

Integrating this over $d\Omega=\sin(\theta)d\theta d\phi$ gives the total emitted intensity

$$I_{em}=4\pi(k_1+k_2)(I_z+I_{xy})(1-\tfrac{1}{3}P_1). \tag{2.22}$$

Using Eq. (2.22), Eq. (2.20) can be multiplied by unity in the form

$$\frac{I_{em}}{4\pi(k_1+k_2)(I_z+I_{xy})(1-\frac{1}{3}P_1)}=1 \tag{2.23}$$

to obtain

$$\frac{dI(\theta,\alpha)}{d\Omega}\propto I_{em}\left[\frac{1+P_1k\cos(2\alpha)-P_1\cos^2(\theta)\left[1+k\cos(2\alpha)\right]}{1-\frac{1}{3}P_1}\right]. \tag{2.24}$$

Thus, for the measured intensity to be independent of P_1, it is desired that

$$-\tfrac{1}{3}P_1=P_1k\cos(2\alpha)-P_1\cos^2(\theta)\left[1+k\cos(2\alpha)\right]. \tag{2.25}$$

If $k=0$, meaning there is no polarizer, the solution of Eq. (2.25) is the magic angle (and its supplement) $\theta=\cos^{-1}\left(\frac{\pm1}{\sqrt{3}}\right)$. If $0<k\leq1$ then solving Eq. (2.25) for α $\left(-\frac{\pi}{2}\leq\alpha\leq\frac{\pi}{2}\right)$ in terms of k and θ gives

$$\alpha=\pm\frac{1}{2}\cos^{-1}\left(\frac{\cos^2(\theta)-\frac{1}{3}}{k\sin^2(\theta)}\right). \tag{2.26}$$

Equation (2.26) gives possible polarizer orientations α as a function of θ and k, and is identical to the expression given in [43] except for the inclusion of k dependence. Figure 2.5 shows plots of α vs. k for various values of θ. When θ equals the magic angle (or its supplement), Eq. (2.26) requires that the polarizer be set at 45°. As shown above, however, no polarizer is required at this collection angle. Note that for $k < 1$ this method is only valid if the instrumental polarizations of the detection elements following the polarizer are negligible, but this is often a good approximation.

An alternative method to remove polarization dependence from optical excitation functions is to measure both I and P_1. It is well known that with these two measurements, the polarization dependence can be accounted for [40]. When detection is performed perpendicular to the beam, examination of Eqs. (2.21) and (2.22) with $\theta = 90°$ shows that the measured intensity, I, is proportional to $(I_z + I_{xy})$, and the total emitted intensity, I_{em}, is proportional to $(I_z + I_{xy})(1 - \frac{1}{3}P_1)$. Thus, neglecting the constant of proportionality, the emitted intensity can be defined as

$$I_{em} = I(1 - \tfrac{1}{3}P_1). \tag{2.27}$$

In the preceding analysis it was assumed that $P_2 = P_3 = 0$. For the case of unpolarized electron impact excitation, symmetry considerations require that $P_2 = P_3 = 0$ if the photons are not collected in coincidence with the scattered electrons (as is the case here), while $P_1 \neq 0$ is permitted. For polarized electron impact excitation, symmetry permits $P_1 \neq 0$, $P_2 \neq 0$, and $P_3 \neq 0$ [7]. However, for this detection geometry the value of P_1 is the same as that for the case of unpolarized electrons [8]. Thus, even if polarized electrons are used, applying one of the above corrections still results in intensities that are identical to those that would be obtained from unpolarized electron impact excitation.

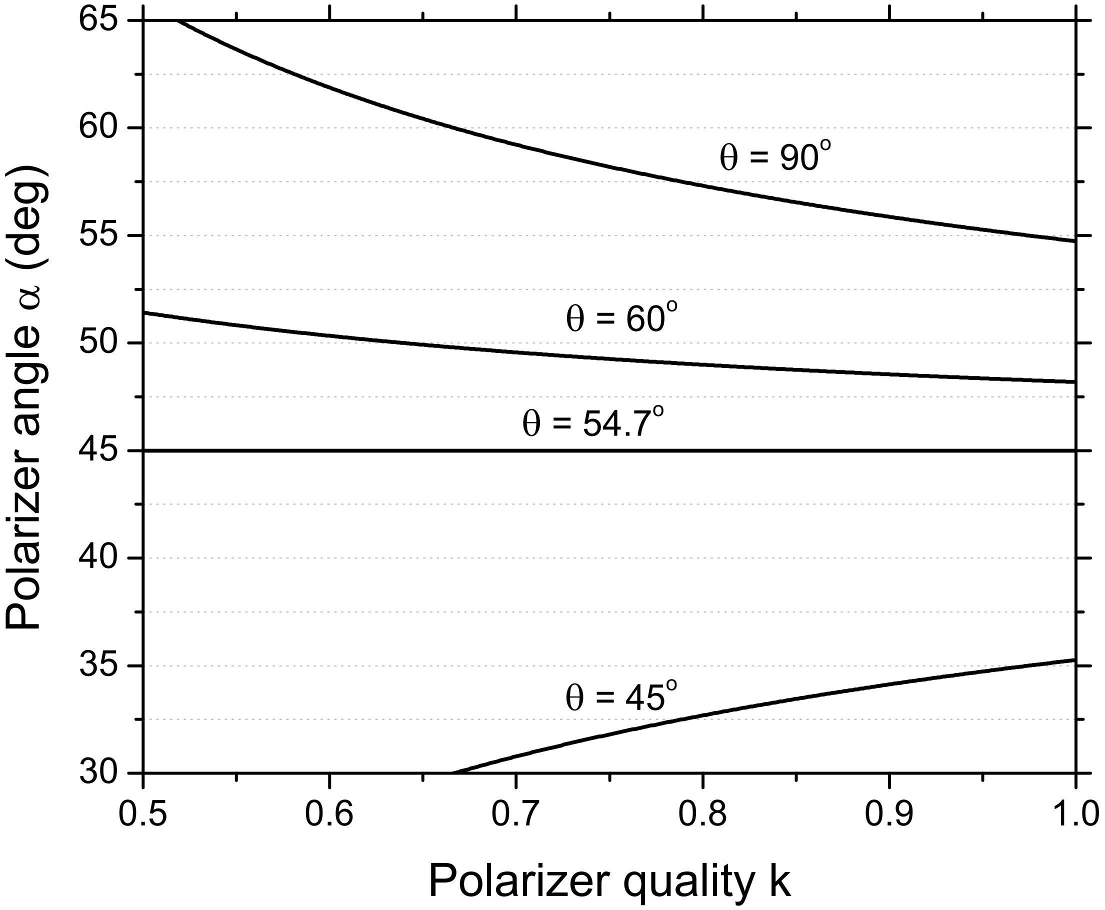

Figure 2.5: Polarizer orientation α as given by Eq. (2.26) required to obtain optical excitation functions independent of target alignment.

2.3.5 Effect of finite solid angle detection on Stokes parameters

Due to the finite optical detection solid angle and possible electron beam divergence in the experiment, the measured P_1, P_2, P_3, and I_{em} values differ from the true values. Approximate expressions to correct for these effects have been presented [44]. The half angle of the optical detection solid angle, ψ_m, is 11° in this experiment, and the approximate half angle for the electron beam is 3° (as defined by the entrance and exit apertures of the target cell). The approximate corrected polarization P_1^C can be expressed as

$$P_1^C \approx \frac{P_1}{1-\epsilon(1-P_1)-\zeta(3-P_1)}, \tag{2.28}$$

where $\epsilon = \frac{1}{4}\psi_m^2 = 9\times 10^{-3}$ and $\zeta = \frac{1}{4}\theta_m^2 = 7\times 10^{-4}$. The corrected I_{em}^C is then given as

$$I_{em}^C \approx I\left[\frac{1-\frac{1}{3}P_1^C}{1-(\epsilon+\zeta)P_1^C}\right]. \tag{2.29}$$

It is stated in Refs. [24, 27] that Eq. (2.28) can also be used to obtain corrected P_2 and P_3 polarizations (by replacing P_1 with P_2 or P_3). This notion is incorrect, as the derivation of Eq. (2.28) does not address the situation where $P_2 \neq 0$ and $P_3 \neq 0$.

Due to the small values of ϵ and ζ, $|P_1^C - P_1| < 3\times 10^{-3}$ for the polarization range relevant to this work. It is not even clear whether the electron beam divergence correction should be applied, and neglecting it gives $|P_1^C - P_1| < 2\times 10^{-3}$. Similarly, $|I_{em}^C - I_{em}|/I_{em} < 4\times 10^{-3}$. As the magnitudes of these corrections are smaller than the typical reported uncertainties, the corrections provided by Eqs. (2.28) and (2.29) have not been applied to the data presented in this work. The effect of the collecting lens on light polarization is negligible [45].

2.4 Data acquisition

Data acquisition and automated control of the experiment is performed using National Instruments (NI) LabVIEW 7.0 software installed on a modern personal computer (PC). The PC (Windows XP operating system) contains a 2.0 GHz single-core CPU (AMD Athlon 64 3200+) and 512 MB of RAM. It is outfitted with a NI PCI-6024E hardware card, a NI PCI-GPIB hardware card, two parallel (printer) ports, and the typical complement of USB ports.

The experimental parameters controllable with software are the electron beam energy and the angular positions of all optical components. The potential difference between the crystal and target cell is adjustable using the Sorensen DC power supply (equipped with GPIB interface). The angular position of the source-laser quarter-wave retarder is varied by the Standa rotation stage (USB connection between the stepper motor hardware driver and PC). The optical polarimeter stepper motors with Arrick Robotics MD2 hardware drivers are interfaced with the PC via the two parallel ports (software drivers were purchased from TEM Consulting for use with LabVIEW).

Measured quantities consist of pressures, currents, and counts from the PMT. Pressures are measured by routing the analog outputs of the Granville-Phillips Series 307 controllers to 12-bit analog inputs on the NI PCI-6024E card. Currents from the Keithley 485 picoammeters are communicated to the PC via GPIB signals. Pulses (TTL) from the Phillips Scientific discriminator are counted using a 24-bit counter on the PCI-6024E card.

For fixed settings of the electron beam energy and optical component angular positions (source and polarimeter retarders), measurements of pressures, currents, and counts are performed concurrently during a given dwell period (5 s is typically used). The PCI-6024E card contains two counters; while one counts pulses, the other is configured to measure the actual dwell period. This is done because the desired dwell setting is sometimes not strictly obeyed by the software, so measurement of the actual dwell is needed to accurately determine the count rate. (The 100 kHz clock rate of this second counter indicates that the maximum dwell that can be used is <167 s because of the 24-bit restriction.) While the counters are operating, the pressures and currents are sampled every 500 ms (2 Hz). Thus, for a 5 s dwell setting, 10 samples of each pressure and current channel are taken and the average is returned. (This 2 Hz sample rate restriction is due to the Keithley 485 GPIB ammeters.) Thus, a "Counter.vi" LabVIEW subroutine accepts a dwell input and returns the number of counts, the measured dwell period, the average of the current measurements, and the average of the pressure measurements.

Data is acquired either by scanning all the desired beam energies before incrementing the polarimeter retarder angle, or by stepping through the polarimeter retarder angles before incrementing the beam energy. The method wherein the energies are scanned first will hereafter be referred to as the SEF method, and the latter technique of first stepping through the polarimeter retarder angles will be called the SAF method.

For the SEF method, the acquisition proceeds as follows. First, the electron beam energy is set to the lowest desired energy, and the Counter.vi subroutine is then initiated to make measurements at this particular energy. When the subroutine is finished, the energy is incremented and the process continues until measurements for all desired beam energies are completed. The angle of the polarimeter retarder is then incremented by 22.5° and another energy scan is performed, and so on. After the retarder has been returned to its original position (one full rotation), the source quarter-wave retarder is rotated by 90°, changing the sign of the electron spin polarization P_e. A typical "run" lasts ∼48 hrs., and measuring ∼20 energy points with a 5 s dwell means that ∼25 complete rotations of the source quarter-wave retarder are performed.

The SAF method begins in a similar way; after the lowest energy is set, the Counter.vi is initiated. After the Counter.vi returns the first measurement, the polarimeter retarder is rotated by 22.5° and another measurement is made. This continues until a full rotation of the retarder is completed. The beam energy is then incremented, and so on. After all energies have been scanned, the source quarter-wave retarder is rotated by 90°. The dwell is typically lengthened to 10 s for this method to increase efficiency by reducing the time spent rotating optics. (It takes ∼2 s to rotate a polarimeter stage by 22.5°.) The SEF method is thus more efficient, and it might be expected to provide a more accurate energy dependence of the optical excitation cross sections in light of possible temporal drifts, while the SAF method may be expected to provide more accurate polarizations. Over the relatively small energy ranges used for this work (∼20 eV), no statistically significant differences have been observed for the polarizations obtained using the two different schemes. Thus, the majority of data presented in this work have been acquired using the SEF method.

2.5 Data analysis

A Fortran code (see Appendix A) was developed to analyze data acquired by one of the two methods (SEF or SAF) described in Sec. 2.4. Each line of a data file generated by the LabVIEW acquisition program contains the energy, polarimeter retarder angle, source quarter-wave plate angle, collected counts, measured dwell period, measured average current, and measured average pressure data. This data is loaded into arrays by the Fortran program. Count rates are constructed by dividing collected counts by their respective measured dwell periods. A linear relation is applied to scale the pressure measured by the optical polarimeter ion gauge so that it is representative of the pressure in the target gas cell. The currents measured on the back aperture of the target cell and in the Faraday cup are negated (collected electrons yield negative currents) and summed to be used for signal normalization.

The data are sorted into arrays such that the constructed count rates, pressures, and currents corresponding to degenerate energy and angle settings are grouped. The term "degenerate" angles implies that measurements taken with the polarimeter (or source) retarder at angular position β are grouped with all other measurements taken at later times with angle β, as well as with all measurements taken with angle $\beta + 180°$ due to the half-rotation symmetry of optical retarders. For the polarimeter retarder, one full rotation consists of sixteen measurements taken in 22.5° increments. Due to the retarder half-rotation symmetry, this number is reduced to eight, hence the summation limit in Eq. (2.14). For the source quarter-wave retarder, four measurements are made every 90°, and these are combined into just two groups (0° and 90°). When the source quarter-wave plate angular position is at 0° or 180°, the sign of the electron spin polarization P_e is positive (spin "up" in the lab), and for angles 90° or 270°, the sign is negative (spin "down" in the lab). When scattered electrons are not detected, non-zero measurements of Stokes parameters P_2 and P_3 are proportional to P_e [7, 13], thus the spin-normalized ratios P_2/P_e and $-P_3/P_e$ are reported (the origin of the minus sign preceeding P_3 was discussed on p. 23).

The above "grouping" procedure is done in preparation for combining the data to form means and uncertainty estimates. For near-threshold experiments, a few energy points ($\sim$ 5) are measured below the threshold for excitation of the fluorescing state(s) of interest. These points are used to determine the background signal, which must be subtracted. First, however, the energy threshold must be determined. To accomplish this, all count rates for a given energy are temporarily grouped together regardless of angular dependence. Chauvenet's criterion [46] is then applied in order to eliminate outliers (anomalous spikes from the PMT). The resulting distributions are averaged and the standard deviation of the mean is used to indicate the statistical uncertainties. This data is then used to determine the threshold energy, which is taken to coincide with the first count rate that deviates by greater than $\sim 2.5\sigma_{\mu}$ from the below-threshold horizontal background. (This background is typically consistent with the PMT dark count rate of ~ 2 Hz).

Once the threshold energy has been determined, below threshold counts are averaged (and subjected to Chauvenet's criterion) to determine a background count rate. An option exits in the code so that this can be done for the eight individual groups corresponding to the unique polarimeter retarder angles to check if the background is polarized. These individual averaged backgrounds are found to be statistically consistent with each other, indicating there is no significant polarization of the background light. Thus all below-threshold counts are grouped to determine the background count rate, which is then subtracted from all count rates taken at all energies.

After the background count rate is subtracted, the count rates at and above the threshold energy are normalized to their corresponding measured pressure and current values. This is done by simply dividing the count rates by the pressures and currents, and multiplying the result by the average pressure and current (computed for the threshold energy value). The normalized count rate distributions for the unique energy and angle values are then subjected to Chauvenet's criterion. The application of Chauvenet's criterion to distributions typically results in less than 1% of the data being discarded. The resulting averages and standard deviations of the means can then be used to compute the Stokes parameters.

For each energy and sign of the spin polarization, the count rates and uncertainties for the eight retarder angles are used to compute a set of Stokes parameters. This is done by applying Eq. (2.14) from Sec. 2.3.1. Here I_i' refers to the background-subtracted, pressure- and current-normalized count rates corresponding to a polarimeter retarder angle β_i. The values of k and δ are independently measured. The linear polarizer offset angle α_0 and retarder offset β_0 are ideally zero, but serve to account for physical misalignments (meaning that the optical axes may not be exactly parallel to the electron beam axis). These angles can be determined using the data for cases where large linear and circular polarizations are measured. It is initially assumed that $\alpha_0 = 0$. The β_0 parameter is then varied in the analysis code and chosen such that the resulting energy average of P_e-sign-normalized P_3 values is maximized. This value of β_0 is then stored, and will be referred to here as β_C. The α_0 parameter is then varied, and for each distinct value β_0 is set equal to $\alpha_0 + \beta_C$. The value of α_0 is selected which provides a minimum for the energy average of P_e-sign-unnormalized P_2 values (the energy average of P_1 values is concurrently found to be maximized).

Propagation of uncertainties is done numerically [46]. The uncertainties for k, δ, α_0, and β_0 are neglected as they do not contribute largely to the overall uncertainties. The statistical uncertainties in the normalized count rates are propagated by sequentially evaluating the Stokes parameters in Eq. (2.14) with the count rate uncertainties added to (or subtracted from) their corresponding count rates. These evaluations are used to compute the deviations for the functions, which are then squared and combined in quadrature to form the final error estimates. Finally, the Stokes parameters for both spin polarizations ("up" and "down") must be combined. To this end, the P_2 and P_3 data are divided by the signed value of P_e, and the weighted mean and error of the weighted mean is then constructed for I, P_1, P_2/P_e, and $-P_3/P_e$.

Chapter 3. Helium Negative Ion Resonances

Helium resonance structures located above the ionization potential were first discovered in a transmission experiment by Kuyatt *et al.* [47]. Two features having energies near 57.2 and 58.3 eV were then tentatively classified as He^- $(2s^2 2p)\,^2P$ and $(2s2p^2)\,^2D$ states by Fano and Cooper [48]. These designations have since been confirmed [49, 50]. An accurate measurement of the resonance energies performed by Hicks *et al.* [51] found values of 57.22(4) and 58.30(4) eV, respectively, which are in excellent agreement with other experimental and theoretical results [52, 53].

Numerous researchers have done electron transmission and energy-loss experiments to characterize these and other helium negative-ion resonances [54]. Another method of investigation consists of monitoring the fluorescence from states which receive cascade contributions due to decay of the negative-ion resonances. In particular, the intensity and linear polarization of the $3\,^3D \rightarrow 2\,^3P$ transition have been studied with unpolarized incident electron beams [55–59]. (The resonance features in this transition are particularly pronounced.) This experiment is similar, but the incident electron beam is spin-polarized. The Stokes parameters are measured in the 55–60 eV region for the process:

$$\begin{aligned} e + \mathrm{He}\,(1s^2)\,^1S &\rightarrow \mathrm{He}^-\,(2s^2 2p)\,^2P \text{ or } \mathrm{He}^-\,(2s2p^2)\,^2D \\ &\rightarrow \mathrm{He}\,(1s3d)\,^3D + e \\ &\rightarrow \mathrm{He}\,(1s2p)\,^3P + e + \gamma(587.6\,\mathrm{nm}). \end{aligned} \tag{3.1}$$

Interference between these channels and the direct excitation of the $3\,^3D$ state produces resonant features in the observed intensity characterized by Beutler-Fano profiles [60, 61]. Cascade contributions from the 4p, 5p, and 6p levels are responsible for ~50% of the observed 587.6 nm radiation in the 50-60 eV energy range [59]. However, the effects of the resonances on the emitted radiation from the 4p and 5p states are known to be small [56], and we expect the same for the 6p state. Therefore, subsequent cascades from these states to the $3\,^3$D level do little to affect the resonance features discussed below and will be ignored.

The Stokes parameters are known to be sensitive to exchange effects and magnetic forces [15]. As mentioned in Sec. 2.3.4, when the electron beam is transversely spin-polarized and the scattered electrons are not detected, Stokes parameters P_2 and P_3 are not required to be zero as they are in the unpolarized case [7]. The motivation for this experiment was to investigate these values carefully in the energy region of the resonances, as observed features could be a signature of relativistic magnetic forces acting during the resonance lifetime. While such forces are generally small in light atoms, the resonance lifetime (∼10 fs), roughly 50 times longer than the classical orbital period for $n = 2$ states of He, could reasonably be expected to enhance their influence. If electron spin precession occurred in the triply-excited resonance due to magnetic forces, measurement of a non-zero value of P_2 and variations in P_3 would be allowed because spin could no longer be factored out of the interaction Hamiltonian. Equivalently, one could say that the compound ion state was not well-*LS* coupled. In the case of P_2, discernable structures near the resonance energies would be a clear indication that magnetic forces are present. Resonance structures in P_3 can be caused by two processes, the first being the magnetic interactions discussed above. Alternatively, variations in P_3 might occur because Coulombic interactions are generally different for the interfering resonance and direct channels leading to $3\,^3$D formation. Since P_3 depends on the initial distribution of M_L states (which also affect P_1 [15]), any difference between the resonant and direct M_L distributions will yield a variation in P_3 across the resonance profile.

3.1 Relative emission

As discussed in Sec. 2.3.4, the measured Stokes parameter I is a quantity that represents the photon intensity collected in a small solid angle (0.12 sr in this experiment). It is not directly proportional to a relative emission cross section due to a dependence on the alignment. The relative emission can be computed using Eq. (2.27) to remove this dependence on Stokes parameter P_1. The intensity, relative emission cross section, and linear polarization fraction P_1 are all independent of the polarization of the incident electron beam, and thus can be directly compared to measurements taken using unpolarized incident electrons. The graph in Fig. 3.1 shows the relative emission cross section for the He $3\,^3\text{D}\rightarrow 2\,^3\text{P}$ transition. The values on the y-scale are representative of our experimental collection rate in Hz. The data sets of other references have been normalized to our lowest energy point. Helium pressure in the target cell was kept at $\sim$0.6 mTorr to minimize the effects of radiation trapping [59].

3.2 Linear polarization P_1

The observed intensity near the resonances can be described by the convolution of a beam energy profile with a modified Beutler-Fano function of the form

$$I^{\|,\perp} = I_b^{\|,\perp} + I_1^{\|,\perp}\left[\frac{(q_1^{\|,\perp}+\epsilon_1)^2}{1+(\epsilon_1)^2}\right] + I_2^{\|,\perp}\left[\frac{(q_2^{\|,\perp}+\epsilon_2)^2}{1+(\epsilon_2)^2}\right], \qquad (3.2)$$

where $\epsilon_r \equiv 2(E-E_r)/\Gamma_r$ and Γ_r is the FWHM of a given resonance with energy E_r. Here, the r indices 1 and 2 refer to the ^{2}P and ^{2}D peaks, respectively. The dimensionless shape parameter is given by q_r, and the superscripts indicate the collection of light with linear polarization oriented either parallel or perpendicular to the incident electron beam. The

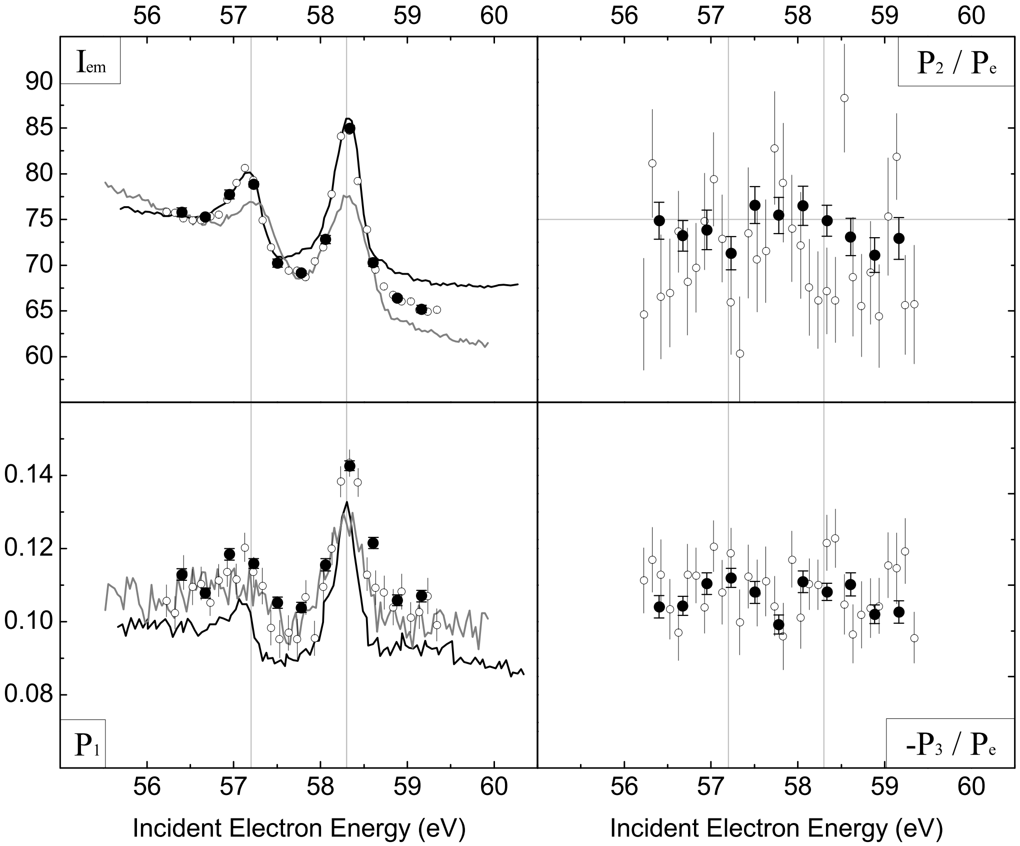

Figure 3.1: Relative emission cross section I_{em} (in arbitrary units) and polarizations P_1, P_2/P_e, and $-P_3/P_e$ for the He $3\,^3D \rightarrow 2\,^3P$ 587.6 nm transition. Our data are shown as empty and filled circles (two separate experimental runs), the values of Defrance [56] are displayed as black lines, and the work of Cvejanović *et al*. [59] is represented with gray lines. Resonance energies of 57.2 and 58.3 eV are indicated.

background far from the resonances is then

$$B^{\|,\perp} = I_b^{\|,\perp} + I_1^{\|,\perp} + I_2^{\|,\perp}, \tag{3.3}$$

where I_b is treated as a function of energy while I_1 and I_2 are taken as constants. The "resonance polarization" (with $\epsilon_1 = 0$ for the ^{2}P resonance and $\epsilon_2 = 0$ for the ^{2}D resonance) is then defined by Defrance [56] to be

$$P_r(\epsilon_1 \text{ or } \epsilon_2 = 0) = \frac{\left(I^{\|} - B^{\|}\right) - \left(I^{\perp} - B^{\perp}\right)}{\left(I^{\|} - B^{\|}\right) + \left(I^{\perp} - B^{\perp}\right)}. \tag{3.4}$$

As pointed out by Batelaan *et al.* [58], this definition of the resonance polarization depends not only on parameters associated with the resonant process, but also on the direct excitation cross section. Batelaan *et al.* [58] have shown that the light intensity for a given $3\,{}^3$D M_L state can be expressed as

$$I = I^{\text{dir}} + I^{\text{res}} - I^{\text{int}}_{\text{sym}} + I^{\text{int}}_{\text{asym}}, \tag{3.5}$$

where I^{dir} and I^{res} can be identified uniquely with the direct excitation and resonant excitation processes, and $I^{\text{int}}_{\text{sym}}$ and $I^{\text{int}}_{\text{asym}}$ correspond to symmetric and antisymmetric interference terms. Because I^{res} and $I^{\text{int}}_{\text{sym}}$ exhibit the same energy dependence, they are not distinguishable in this type of experiment. Equation (3.4) implicitly contains both these terms, and as such, cannot be formally identified as the "resonance polarization," i.e., the polarization associated with a purely resonant process.

This being said, we have evaluated P_r for the sake of comparison with earlier work. We not only analyze our data, but also that of Defrance [56] and Cvejanović *et al.* [59]. The data of Batelaan *et al.* [58] were excluded from this analysis because only the intensity values were published (and thus values for $I^{\|}$ and $I^{\perp}$ could not be constructed).

Resonance polarizations are calculated by fitting data of a given polarization state with a convolution of Eq. (3.2) with an apparatus profile describing the electron beam energy distribution. In order to approximate this distribution, the sum of a normalized triangle (T) and normalized Lorentzian (L) (both with identical widths) was used so that the profile could be expressed as $wT(E)+(1-w)L(E)$, where the weighting factor w obeys $0 \leqslant w \leqslant 1$. The convolution of this apparatus profile with Eq. (3.2) gives a tractable analytical expression [62], and the triangle term closely represents the numerical result obtained when using a Gaussian instead. This form is somewhat arbitrary, but it gives reasonable results and, lacking detailed knowledge of the beam profiles, seems justifiable. A quadratic form is chosen for the background dependence I_b. The resonance widths (0.071 and 0.047 eV [50]) and energy separation (1.094 eV) [52] are held fixed to facilitate convergence. Fitting is done with a nonlinear curve fitting routine (OriginLab software, Levenberg-Marquardt algorithm), and after convergence is obtained all parameters are fixed (assuming zero uncertainty in the fitting parameters) except for the I_1 and I_2 amplitudes. The subsequent error estimates for these values are used to determine the uncertainty in the resonance polarization.

The fits are shown in graphs (a), (b), and (c) of Fig. 3.2. The fitted values of the electron beam energy widths are 0.29, 0.43, and 0.33 eV, and the weighting factors w are approximately 0.3, 1.0, and 0.4 for the data in (a), (b), and (c), respectively. The resulting $q^{\parallel,\perp}$ values for the ^{2}P state are in the range of -2.6 to -11, and for the ^{2}D case lie between -11 and -42 for the fits. These are similar to results reported by Defrance and de Froment [55]. The reduced χ^2 values for all fits in Fig. 3.2 lie between 0.14 and 1.2. Previously reported resonant polarizations and the results from our fits are shown in Table 3.1.

Comparison of the previously reported results for P_r (first part of Table 3.1) shows that Cvejanović *et al.* [59] and Batelaan *et al.* [58] are in close agreement, while Defrance's

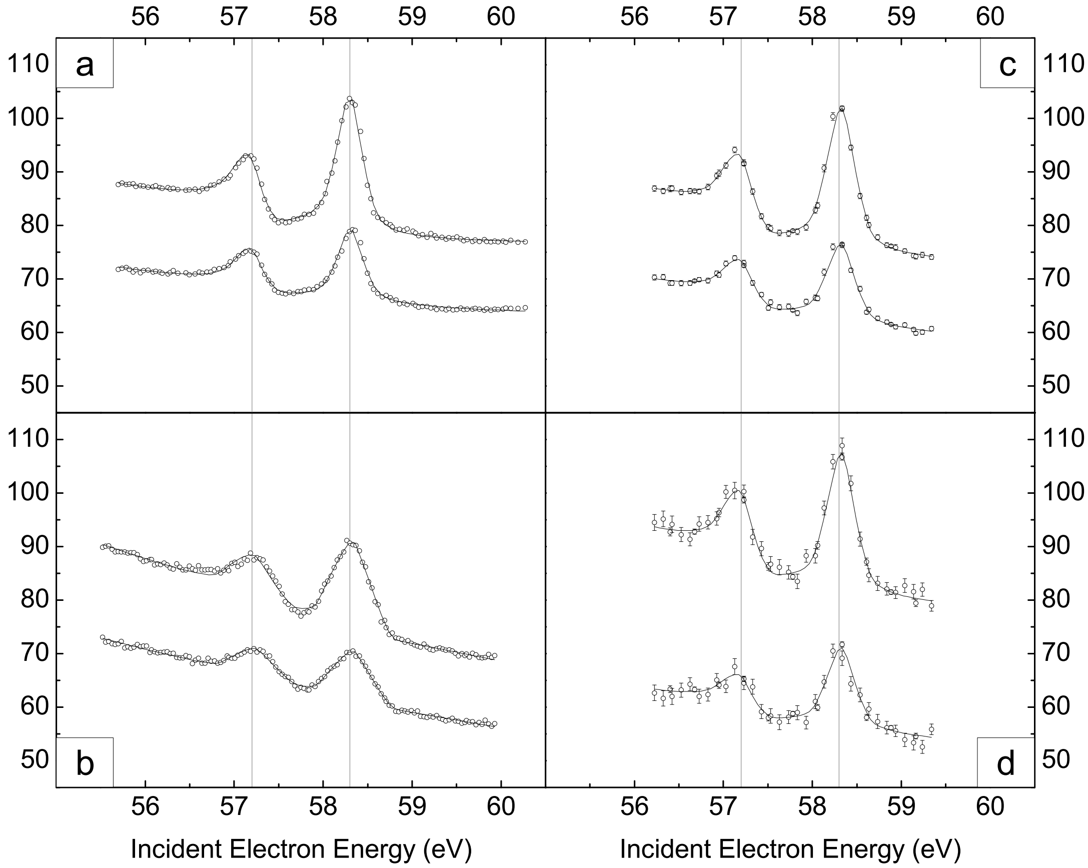

Figure 3.2: Graphs (a), (b), and (c) contain parallel and perpendicularly polarized intensities (in arbitrary units) from Defrance [56], Cvejanović *et al.* [59], and this work respectively. Graph (d) contains our σ^+ and σ^- polarized intensities normalized to electron spin. Fits to the data are represented as solid lines. Resonance energies of 57.2 and 58.3 eV are indicated.

Table 3.1: Linear polarization fractions for helium negative ion resonances (“resonance polarizations”) as defined by Defrance [56].

State	Present work	Cvejanović *et al.* [59]	Batelaan *et al.* [58]	Defrance [56]
Previously reported values				
^{2}P (57.2 eV)	—	0.13 ± 0.03	0.14 ± 0.02	0.24 ± 0.03
^{2}D (58.3 eV)	—	0.247 ± 0.001	0.25 ± 0.02	0.30 ± 0.03
Our results and results we obtained by fitting the data of Refs. [56, 59]				
^{2}P (57.2 eV)	0.22 ± 0.03	0.16 ± 0.02	—	0.13 ± 0.02
^{2}D (58.3 eV)	0.29 ± 0.01	0.27 ± 0.01	—	0.30 ± 0.01

values are about 3σ away for the ^{2}P resonance and less than 2σ away for the ^{2}D state. This seems to indicate that the results of Defrance are in error. By using the same values of the resonance widths and separation energy in our fits to all the available data, the situation changes somewhat (second part of Table 3.1). Our results for the ^{2}P resonance indicate that previous work is in good agreement and that our value is about 2σ larger, while for the ^{2}D resonance all polarizations are in reasonable agreement.

Our data support the interesting conclusion that P_r for both resonances is nearly consistent with the kinematically demanded value for non-interfering resonant state production, followed by decay to the He (1s3d)^{3}D state and an outgoing electron, with the outgoing electron in its lowest allowed angular momentum partial wave [56, 58]. In the case of the ^{2}P resonance, this is an $l = 1$ wave, and P_r is expected to be 0.24 as computed by van Ittersum [58, 63]. For the ^{2}D resonance, the outgoing electron can have $l = 0$ and for this case P_r should be 0.32 [63] (this is the same as that required for threshold polarization of the $3\,^3$D state). This is remarkable because, as mentioned earlier, the use of Eq. (3.4) does not allow measurement of the pure resonant polarization. Thus, we conclude as did Batelaan *et al.* [58] that the symmetric interference contribution $I^{\text{int}}_{\text{sym}}$ is either small or exhibits a similar M_L dependence as the resonant I^{res} term (which leads to equivalent light polarizations). Higher-order allowed outgoing partial waves could also contribute to some extent, which may account for the fact that our measurements are slightly lower than the required threshold values. No further conclusions can be drawn from the present experiment, but we note that the definitive measurement of resonant polarizations must involve some mechanism to distinguish between I^{res} and $I^{\text{int}}_{\text{sym}}$. The fitting procedure to extract resonant polarizations would also benefit from increased electron beam energy resolution.

3.3 Linear polarization P_2/P_e

Our data for P_2/P_e shown in Fig. 3.1 is comprised of two different experimental runs. The first run (open circles) contains more energy steps and greater statistical uncertainty. The weighted mean computed using all energies is −0.019(5) for the first data set and −0.006(3) for the second. Even though the $3\,^3$D state is well-*LS* coupled, it is possible that cascading from higher lying non-well-*LS* coupled states could produce non-zero values of P_2 [30]. If this were the case, one would expect the marginally non-zero P_2 values observed to be essentially independent of energy over the 55–60 eV range, given that resonant cascading is expected to be small (as previously mentioned). We are quite certain that the non-zero measured P_2 values are not due to stray magnetic fields or optical misalignments, as the offset angles α_0 and β_0 were chosen such that P_2 is zero for an unpolarized electron beam. However, we have no explanation for the statistical inconsistency between the two data sets. Therefore, we cannot be confident that our non-zero values of P_2 indicate higher-lying levels that are not well-*LS* coupled as the data sets are inconsistent.

The question of whether P_2/P_e reveals structures at the resonant energies is of greater importance. Resonant P_2 polarizations can be extracted using a similar procedure as that described for P_1 polarizations. This gives −0.22(9) and −0.04(3) for the P^2 and D^2 resonances, respectively. If there were no magnetic interactions, one would expect zero for both resonant polarizations; for the ^{2}P state the extracted value is 2.5σ away from zero. However, the filled circle data point at the ^{2}P resonance energy in Fig. 3.1 is 2σ off the zero line, (which is consistent with the above analysis), but due to the similar scatter of other data points, we do not attribute this to a feature. The reduced χ^2 of a linear fit (with zero slope) to the filled circle data points is 0.90, which argues against the presence of any statistically significant structure.

3.4 Circular polarization $-P_3/P_e$

Figure 3.1 shows $-P_3/P_e$, and there appears to be some structure at the resonance peaks. We attribute these features to Coulombic (as opposed to magnetic) interactions. There are two reasons for this. First, the lack of any obvious resonance structure in the P_2 data indicates that resonant magnetic effects are negligible, as discussed in the introduction. Secondly, the features we observe are consistent with a resonant cascade-free value of $-P_3/P_e$. In the absence of resonant processes, the direct excitation of the $3\,^3$D state via electron exchange produces a kinematically-required threshold polarization of 0.22 (see Appendix B, Sec. B.2). As cascading becomes more important at higher energies (55–60 eV), $-P_3/P_e$ decreases and we measure it to be ~0.19 (Fig. 3.1). The reduced χ^2 value from a linear fit to the filled circle $-P_3/P_e$ data is 2.6, strengthening our assertion that the structures are indeed real.

Using the same techniques as those used for calculating P_r, we determine that the “resonance circular polarizations” for the ^{2}P and ^{2}D features are 0.37(6) and 0.26(2), respectively. The fits are shown in graph (d) of Fig. 3.2. Since these are within 2σ of the threshold value of 0.25, we argue simply that resonant processes give a value of P_3 in agreement with cascade-free exchange excitation. This is not surprising, given that no variation in P_2 (i.e. no magnetic precession of electron spin in the transient resonant state) is observed.

3.5 Conclusion

Having found no statistically significant structure for Stokes parameter P_2 in the helium $3\,^3\mathrm{D} \rightarrow 2\,^3\mathrm{P}$ transition, we conclude that magnetic spin-orbit interactions in the negative ion $(2s^2 2p)\,^2\mathrm{P}$ and $(2s2p^2)\,^2\mathrm{D}$ resonant states are not important, and present an upper bound of $P_2/P_e \leqslant 0.02$ for this effect. Measured values for the linear "resonant polarization" fractions as defined by Defrance are consistent with the kinematically required threshold values for $3\,^3\mathrm{D} \rightarrow 2\,^3\mathrm{P}$ radiation, assuming the outgoing electron is in the lowest allowed angular momentum state. Our values for the circular "resonant polarization" are in fair agreement with the threshold value required by exchange excitation of the $3\,^3\mathrm{D}$ state, with the caveat that the computed resonance polarizations are not solely due to polarization from resonance state decays, but in principle can be coupled to polarization from the direct excitation of the $3\,^3\mathrm{D}$ state through interference phenomena.

Chapter 4. Stokes Parameters for Molecular Dissociation

When investigating electron-molecule collisions, fluorescence can be produced by two different processes. Molecular dissociation can yield excited atomic fragments which produce light; alternatively emission from molecular transitions can be observed directly. This chapter will discuss the dissociation process for atomic fragments H, D, and N. Data is presented in the following chapter regarding transitions in H_2, D_2, and N_2 molecules.

4.1 Dissociative excitation of H_α and D_α

In 1968 Van Brunt and Zare [64] predicted that atomic fragments resulting from molecular dissociation should be polarized if the angular distribution of the outgoing atoms is anisotropic *and* if a difference in the populations of magnetic sublevels exists in the excited atomic states. Later that year, Vroom and de Heer [65] observed such linear polarization in the H_α 656.3 nm signal from the dissociation of H_2, and reported that $P_1 \sim 0.04$ at an excitation energy of 50 eV.

The process for the production of H_α from H_2 (or D_α from D_2) is

$$\begin{aligned} \mathrm{e} + \mathrm{H}_2\, X\, {}^1\Sigma_g^+ &\rightarrow \mathrm{H}_2^* + \mathrm{e} \ \text{ or } \ \mathrm{H}_2^{**} + \mathrm{e} \\ &\rightarrow \mathrm{H}(3l) + \mathrm{H}(n'l') + \mathrm{e} \\ &\rightarrow \mathrm{H}(2l) + \mathrm{H}(n''l'') + \mathrm{e} + \gamma(656\,\mathrm{nm}). \end{aligned} \tag{4.1}$$

Other processes such as dissociative ionization leading to $H(nl)+H^+$ and dissociative attachment leading to $H(nl)+H^-$ are neglected here; the energy threshold for accessing dissociative ionization is greater than the energy range of the presented data [66], and the total cross section for dissociative attachment is known to be negligible in comparison to the pure dissociation process in Eq. (4.1) [66].

The Stokes parameter data for this experiment appears in Fig. 4.1 for the dissociation of H_2 and D_2. The intensity data shows the threshold to be at 16.6 eV [67], as well as a small "shoulder" that exists in the ∼3 eV range below this value. This ∼4 Hz below-threshold signal is due to contributions from molecular fluorescence in the wavelength region of the filter bandpass. The observed ratio of this contaminant signal to the atomic signal is roughly 1.2% for H_α and 1.9% for D_α. This H_α ratio is in fair agreement with the 1.6% level of contamination reported by Khayralla [66]. The effect of this contamination on the measured polarizations is neglected. The current results were acquired at a pressure of 0.5 mTorr, as Khayralla observed nonlinearity in the optical excitation cross section above 1 mTorr.

These results are compared with previous work in Fig. 4.2. The below-threshold contaminant polarizations are omitted for clarity in these plots. Where available, some experimental parameters for the various experiments are collected in Table 4.1. These parameters consist of the target gas pressure, photon detection solid angle, and optical bandpass filter width. The "P_1 adjusted" column indicates if the data has been corrected for the linear polarization P_1, i.e., whether or not Eq. (2.27) has been applied.

Table 4.1: Experimental parameters for the production of H_α (656.3 nm) and D_α (656.1 nm) from molecular dissociation.

Data ref.	Pressure (mTorr)	Detection angle (sr)	Filter FWHM (nm)	P_1 adjusted
Vroom & de Heer [65]	—	—	4	No
Khayrallah [66]	0.005	0.48	1.5	No
Glass-Maujean [68]	—	—	—	NA
Karolis & Harting [34]	0.2	0.09	1.2	Yes
Kedzierski *et al.* [69]	—	—	1	NA
Green *et al.* [20]	12	0.03	0.9	No
Williams & Yu [21]	—	—	1	NA
Current work	0.5	0.12	0.9	Yes

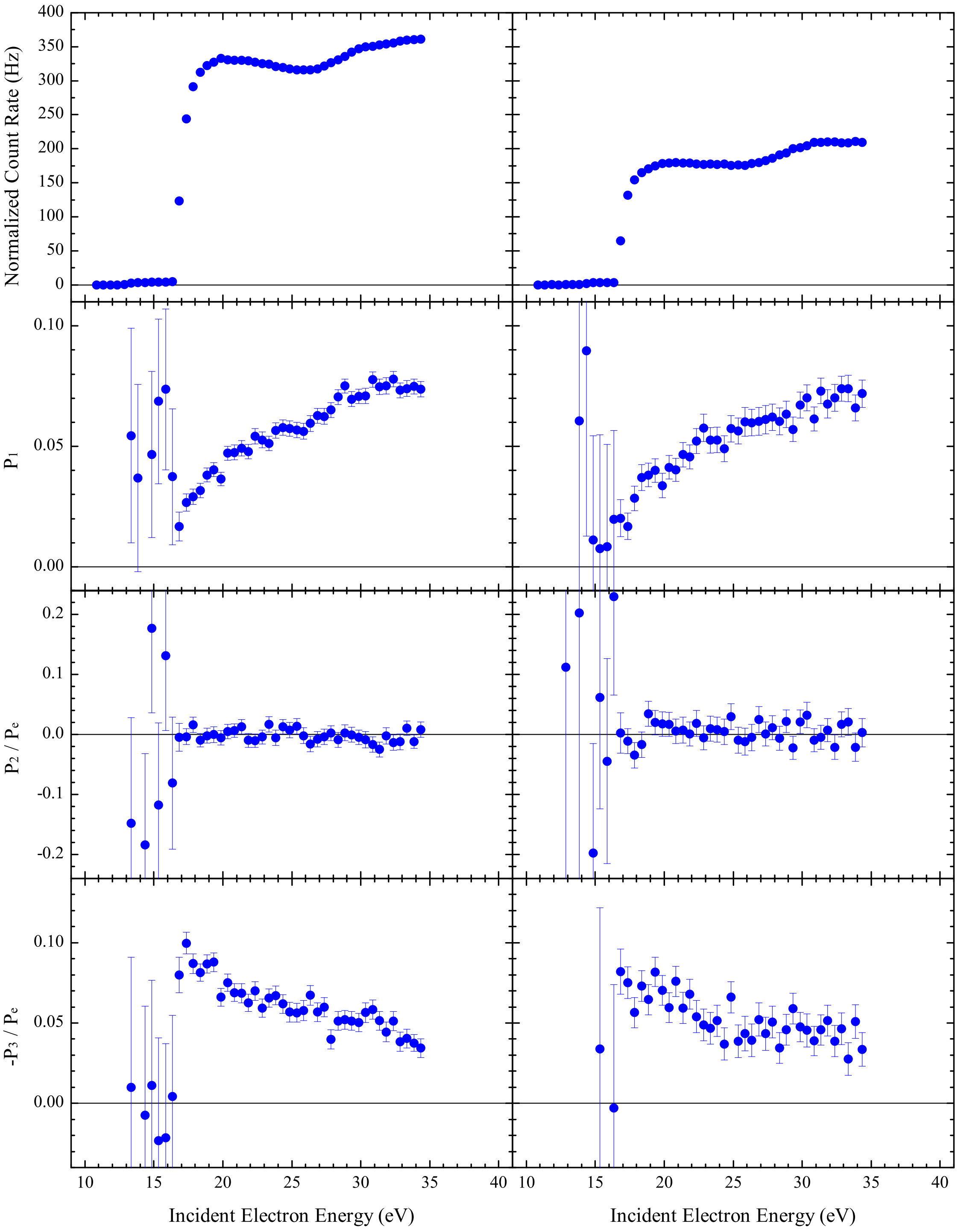

Figure 4.1: Left panel: Stokes parameters for hydrogen (656.3 nm); right panel: Stokes parameters for deuterium (656.1 nm). Threshold for (n=3) production of H and D is at 16.6 eV. The below-threshold polarizations with large error bars are due to molecular contamination (see text).

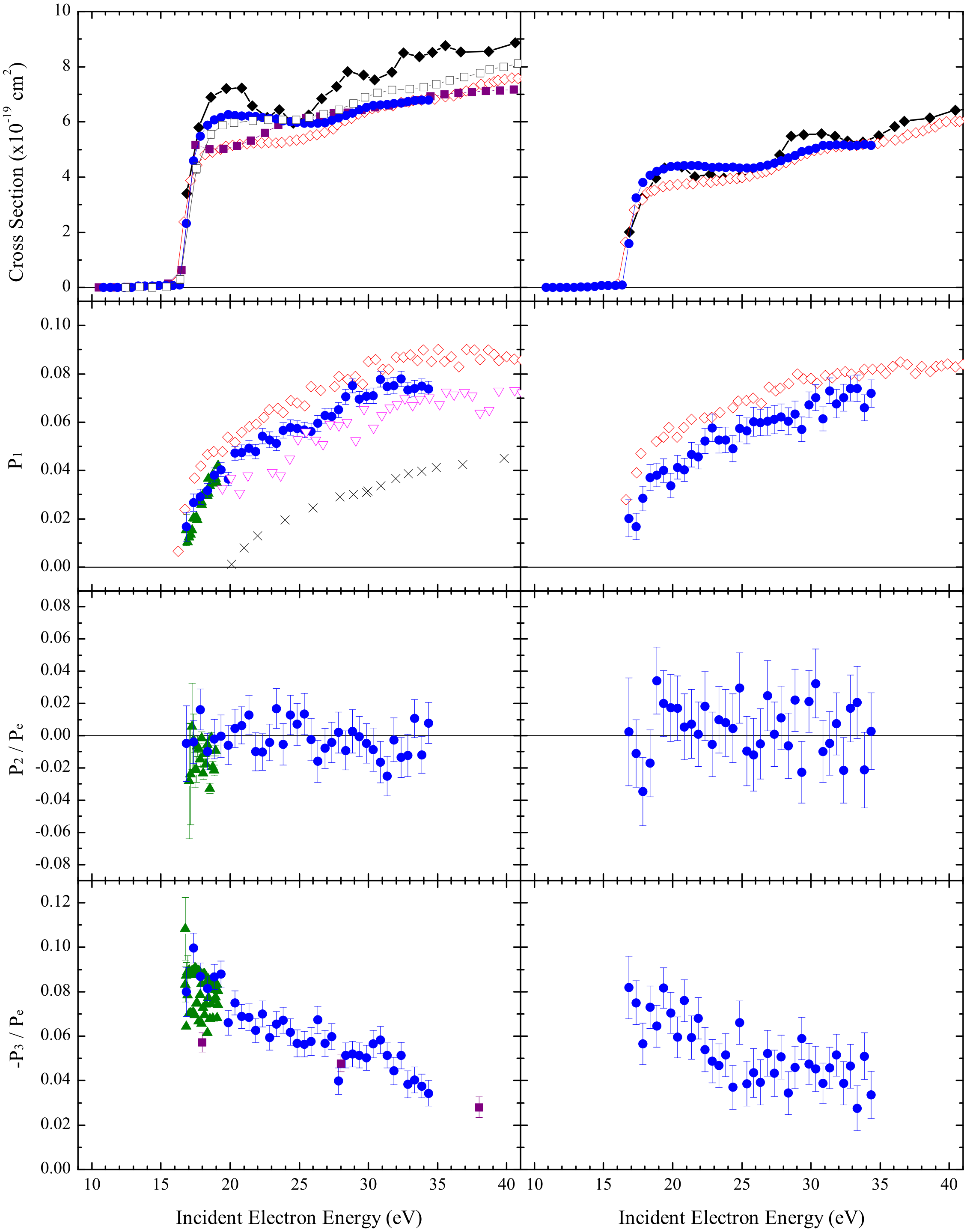

Figure 4.2: Comparisons with existing data. Stokes parameters for dissociated hydrogen (656.3 nm) on the left, deuterium (656.1 nm) data at the right. Filled diamonds: Vroom and de Heer [65]; empty squares: Khayrallah [66]; hatches: Glass-Maujean [68]; empty diamonds: Karolis and Harting [34]; empty triangles: Kedzierski *et al.* [69]; filled squares: Green *et al.* [20]; triangles: Williams and Yu [21]; filled circles: current results.

4.1.1 Optical excitation cross sections

The intensity data measured here most closely agree with that of Khayrallah [66], but due to the issues discussed in Sec. 2.2, it should not be taken as a definitive result. This data, and that of Green *et al.* [20], have been scaled to match the data of Karolis and Harting [34] at an energy of 34 eV. Karolis and Harting scaled their cross sections to match those of Vroom and de Heer at 500 eV. The results of Khayrallah represent an independent experimental calibration with a reported systematic uncertainty of 12%, which provides good agreement with the work of Karolis and Harting. The data of Vroom and de Heer and that of Green *et al.* exhibit structures that do not appear to agree with the other three H_α cross sections, though Vroom and de Heer did state that their apparatus was not designed for low energy operation.

Three features are observed in the cross section data for H_α and D_α production, with energy thresholds at 16.6 eV, ∼25 eV, and ∼32 eV [34, 66]. Figure 4.3 illustrates some potential curves that correlate to $H(n = 3)$ fragments. The thresholds for the intensity features correspond to the accessing of additional dissociation channels as the energy increases. The first feature is due to the predissociation of precursor singly-excited states. Doppler spectroscopy measurements also confirm that for low incident electron energy, the $H(n=3)$ and $D(n=3)$ outgoing fragments are slow (kinetic energy ∼0.2 eV) [68, 72]. The onset of the second feature starting at ∼25 eV corresponds to the excitation threshold of the so-called Q_1 doubly-excited states [70] that correlate to $H(1l)+H(3l)$ or $D(1l)+D(3l)$ atomic limits. For this energy range, broadened Doppler profiles have been observed and imply faster outgoing fragments with energies ∼6.7 eV. Finally, production of the barely discernible third feature beginning at ∼35 eV in the cross sections of Fig. 4.2 is due to a similar mechanism. Here, however, the repulsive dissociating states are the Q_2 states [70] which correlate to $H(3l)+H(2l)$ or $D(3l)+D(2l)$.

The fact that the average kinetic energies of the H and D fragments is found to be sim-

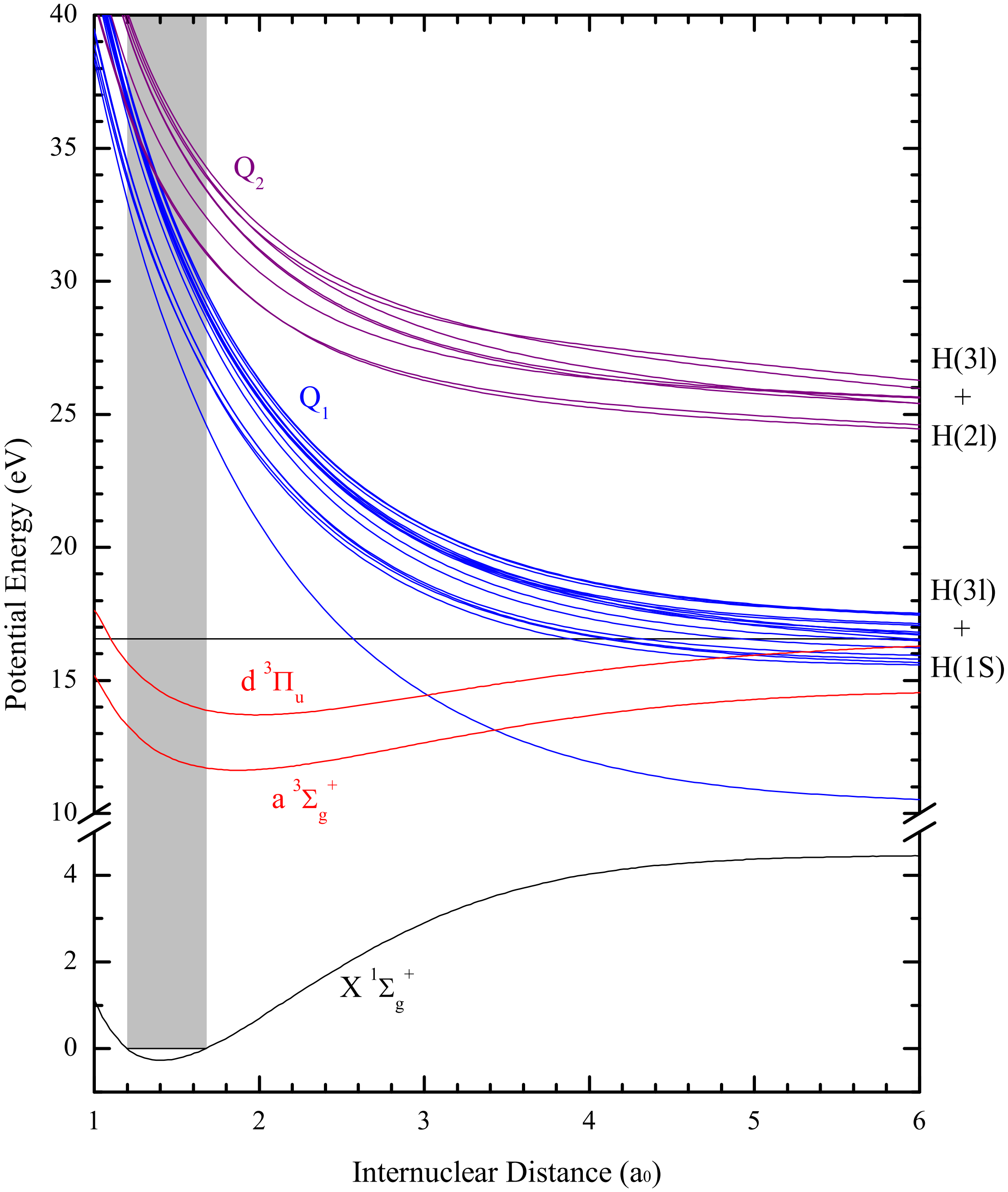

Figure 4.3: Some relevant potential energy curves for molecular hydrogen. The origin is taken to be at $v = 0$ of the ground state. The dissociation threshold of 16.6 eV for H_α (or D_α) production is indicated by a horizontal line, and the Franck-Condon region is shaded. Many more molecular bound states exist but are omitted from the figure. The Q_1 and Q_2 curves were taken from Ref. [70] and the molecular bound curves were taken from Ref. [71]. The state designations of the Q_1 and Q_2 states have been omitted for clarity, but the configurations comprise $^{1,3}\Sigma^+_{g,u}$ and $^{1,3}\Pi_{g,u}$ states.

ilar indicates that the dissociation processes are similar for the two isotopes [72]. However, the H_α and D_α cross sections indicate a H_α/D_α ratio of ∼1.3 [65]. This isotope effect has been attributed to a competition between the autoionization and dissociation processes. Deuterium, being more massive, moves more slowly when dissociating. This allows the probability for autoionization to be larger than that for hydrogen, which translates to a smaller $D(n=3)$ cross section.

4.1.2 Linear polarization P_1

Van Brunt and Zare [64] provided a formula for the angular dependence of the differential cross section for dissociating fragments assuming the axial recoil approximation (dissociation timescale is much less than the rotational period of the molecule). Their result, $f(\theta) \propto [1+\frac{1}{2}\beta(3\cos^2(\theta)-1)]$, contains an anisotropy parameter, β, which characterizes the angular distribution of outgoing atomic fragments. The value of β $(-1 \leqslant \beta \leqslant 2)$ depends on the nature of the dissociating state(s) involved in the dissociation process. For cases where the assignments and contributions of dissociating states are known, β can be related to the observed polarization P_1 [64], so measurement of one parameter could yield the other. However, due to the large number of dissociating pathways in H_2 and D_2 [21, 70, 73], no theoretical predictions of P_1 have been attempted for electron impact induced dissociation. (Computations have been done regarding photodissociation polarization [74], but these are generally less complex due to the dipole selection rules that limit the number of excited states that can be reached.) Thus, the experimental P_1 values in Fig. 4.2 are only qualitatively explained.

The P_1 values from the current work fall between those of Karolis *et al.* and Kedzierski *et al.*, but agree well with the measured values of Williams and Yu for H_α at low energy. Karolis and Harting report that their statistical uncertainties are ∼0.01 (not shown in Fig. 4.2). Kedzierski *et al.* tentatively attribute their low values to electron beam divergence effects in the interaction region. The early data of Glass-Maujean [68] appears very low, but curiously agrees with the reported value by Vroom and de Heer of 0.04 at 50 eV.

The linear polarization falls to ∼0.01 at threshold. Glass-Maujean found that the anisotropy of dissociating fragments is small for low energies, and this is understandable due to the long-lived predissociative Rydberg states that dominate the cross section in this region. This causes an invalidation of the axial recoil assumption, which causes the angular distribution to be smeared out, i.e. $\beta \rightarrow 0$ which implies $P_1 \rightarrow 0$ [64]. At higher energies the double excitation processes become dominant and the axial recoil approximation becomes better, so the value of P_1 increases. The polarizations for D_α are slightly less than those for H_α, which could indicate that the dissociation pathways (and/or their contributions) leading to D_α are somewhat different from those of H_2. Another mechanism which could account for this discrepancy is hyperfine depolarization of the fluorescing atoms, and this will be further discussed in Sec. 4.3.

4.1.3 Linear polarization P_2/P_e

The P_2/P_e and $-P_3/P_e$ data shown in Fig. 4.2 represent the results of experiments with spin-polarized electron beams. For the P_2/P_e case only two data sets exist, that of Williams and Yu [21] and this work. Williams and Yu [21] report statistically significant non-zero values of P_2/P_e within 2 eV of the H_α threshold; remarkably $\sim\frac{1}{2}$ of their total P_2/P_e data is $>2.5\sigma$ away from zero. If their data is not in error, this is indicative of magnetic spin-orbit effects, as discussed in Chaps. 1 and 3. Williams and Yu assert that their observed structures in P_2 are correlated with energy thresholds for accessing dissociation pathways, and mention that the P_2 data exhibits “sharp effects” near the thresholds leading to $n = 4$ (17.23 eV) and $n = 5$ (17.5 eV) state production. However, this is somewhat perplexing as their data near 17.2 eV are consistent with zero. Five data points are $>5\sigma$ from zero, with the 18.55 eV point being a staggering 10.6σ off the zero line. The points surrounding it (0.1 eV energy steps) are only 2.9σ and 0.4σ from zero. This seems to imply that the P_2 structures are narrow, and that their electron beam energy width is small. The authors state that the apparent (unmeasured) beam width is <0.2 eV, though they reported 0.4 eV in a previous paper [75] and mention no improvements to the apparatus. The uncertainties on the current results are too large to confirm the previous results of Williams and Yu, but appear entirely consistent with zero in this near-threshold energy region.

4.1.4 Circular polarization $-P_3/P_e$

The circular polarizations ($-P_3/P_e$) in Fig. 4.2 comprise three data sets. The experiment of Green *et al.* [20] used a detection geometry wherein fluorescence was viewed in a direction parallel to the electron beam (and spin polarization direction) instead of in the traditional perpendicular manner. This explains why there is no accompanying P_2 data from this reference in Fig. 4.2, because for this detection geometry P_2 is required to be zero [8, 13]. The $-P_3/P_e$ value for the low energy point of Green *et al.* appears comparatively small, and this may be related to the fact that the experiment used a 10^{-2} T collimating magnetic field. It's possible that this magnetic collimation effectively increased the detection solid angle at lower electron energies where the transverse electron velocity becomes larger relative to the parallel component, and such an increase in solid angle would lead to depolarization. Green *et al.* [20] also mention that Paschen-Back decoupling of L and S due to the external magnetic field might reduce the value of observed polarization. The Paschen-Back decoupling mechanism involves $\boldsymbol{S}$ decoupling from $\boldsymbol{L}$ such that $\boldsymbol{S}$ and $\boldsymbol{L}$ precess independently in the external magnetic field (J loses its status as a good quantum number). For extreme decoupling in a large magnetic field, orientation of $\boldsymbol{L}$ due to $\boldsymbol{S}$ cannot be achieved and $P_3 \to 0$. For smaller fields, such as the 0.01 T considered here, this effect is expected to be small [20]. The fact that the data was taken at a high pressure (12 mTorr) may also contribute to depolarization because of multiple scattering processes. This issue is compounded by the magnetic field which keeps scattered low energy electrons confined in the detection volume, thus increasing the effect of secondary processes. The data of Williams and Yu actually consists of two data sets taken with different values of P_e, so two points are plotted at each energy. When normalized to the reported values of electron spin, the sets do not appear to be consistent with each other.

The value of the circular polarization implies that exchange excitation of triplet states plays a significant role in the dissociation process. Singlet states contributing more fluorescence at higher energy are likely responsible for the observed drop in polarization because these would provide no circular polarization. In fact, this appears to be a key advantage of using spin-polarized electrons. Measurement of the circular polarization allows more information to be inferred about the relative contributions of different dissociating states. It is hoped that this extra information will be of some aid to future theoretical calculations.

4.2 Dissociative excitation of N

Data was acquired for a dissociated atomic transition in nitrogen to demonstrate that nonzero circular polarization can be achieved, i.e., atomic fragments from N_2 can be oriented similar to the H_α and D_α cases. For this experiment, the 824.24 nm $(3p)^4P_{3/2} \rightarrow (3s)^4P_{5/2}$ fluorescence was investigated. This light was selected using a bandpass filter centered at 824.32 nm with a FWHM of 0.38 nm. The data was acquired at a pressure of 1 mTorr. The Stokes parameters are shown in Fig. 4.4.

The threshold for 824 nm light production is at 21.6 eV [76]. The intensity data show a below-threshold peak, which is likely caused by molecular contamination. The "weak" nitrogen infrared afterglow system, $B'\,^3\Sigma_u^-(v' = 5) \rightarrow B\,^3\Pi_g(v'' = 1)$, at 824.7 nm [77] is within the bandpass filter. The relative contribution (normalized to the transmission

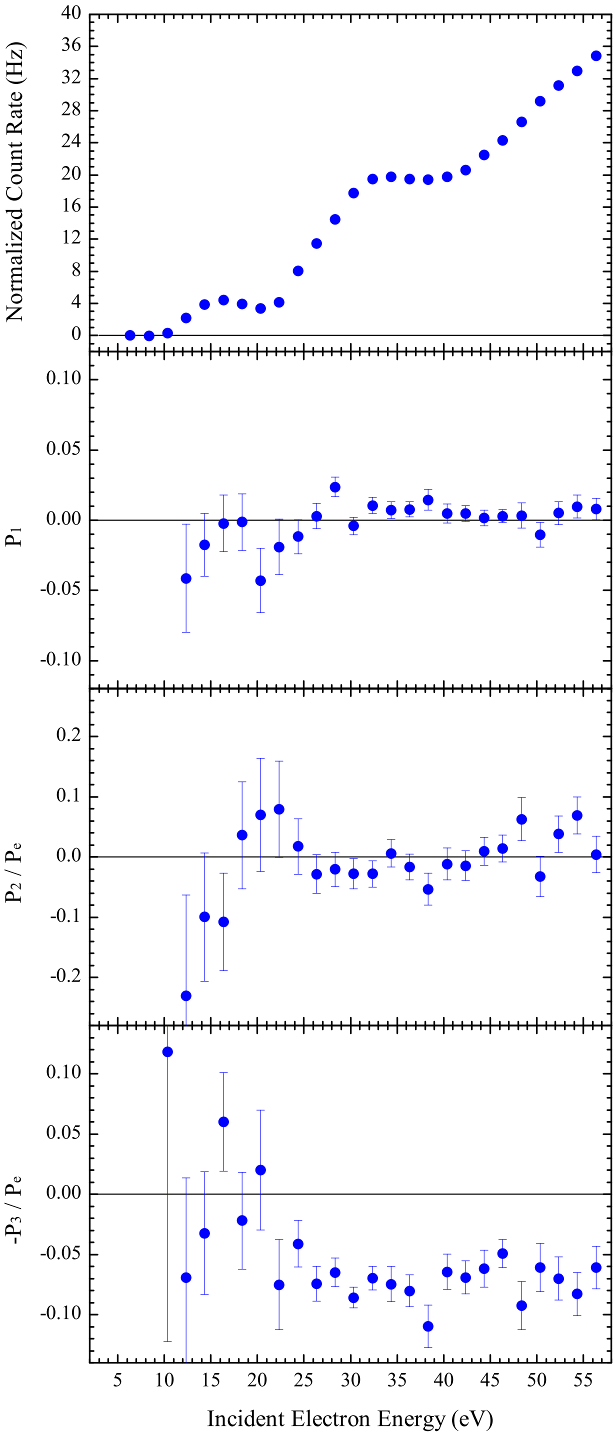

Figure 4.4: Stokes parameters for dissociated nitrogen (824 nm). Threshold for production of the atomic line radiation is at 21.6 eV. Below threshold contribution is likely due to molecular transitions within the interference filter bandpass.

at 824.32 nm) allowed by the filter profile is ∼9%. The possibility that other molecular lines are present in this wavelength region cannot be excluded.

The linear polarization for this transition is small, and appears to be negative at the threshold, though it is is difficult to be sure as the below-threshold contaminant peak dominates the contribution to the Stokes parameters. The P_2/P_e data are not observed to be non-zero. The non-zero circular polarization is found to be negative ($-P_3/P_e < 0$). This appears to be a consequence of the initial and final J values for this specific transition. The final state has a larger J than the initial state, so the initial oriented J values get larger upon decay, which forces the outgoing photons to have helicity opposite that of the incident electron spin due to conservation of angular momentum.

4.3 Comparison with atomic threshold polarizations

Some rudimentary comparisons are made here to better quantify the observed values of the linear polarization P_1 and circular polarization $-P_3/P_e$ observed for the H_α, D_α, and N (824 nm) transitions. Due to the complexity and lack of theoretical predictions for Stokes parameters from molecular dissociation, a completely different situation is considered. The theoretical framework for calculating the threshold Stokes parameters for atomic transitions is well established [13, 18], and it is worthwhile to compare these predictions with the observed values from dissociation experiments. Such a comparison is strictly incorrect for several reasons. The calculation of atomic threshold polarizations requires that the ground state angular momentum is zero, and relies on the fact that only $M_L = 0$ states can be excited at threshold due to conservation of angular momentum. These conditions are not satisfied for molecules. The ground states have a thermal rotational distribution which is generally non-zero at room temperature. However, for light molecules such as the ones considered here, the direction of spin orientation (obtained by exchange excitation) should be conserved in the lab frame if the dissociation timescale is short compared to molecular rotation. Thus, outgoing fragments which have exchanged an electron with one from the incident beam will be oriented similar to experiments with atomic, instead of molecular, targets. The alignment of the fragments will be largely different than in the atomic target situation. However, the circular polarization typically depends strongly on orientation and only weakly on alignment. Thus, it is expected that this comparison will be most useful for values of $-P_3/P_e$.

The calculations of the threshold polarizations for the desired transitions are given in Appendix B. The H_α and D_α cases are treated in Sec. B.3, and the results for N (824 nm) appear in Sec. B.4. For simplicity the hyperfine depolarization in H and D was neglected, and thus the polarizations are identical. In reality, $I = \frac{1}{2}$ for H and $I = 1$ for D, thus the D_α Stokes parameters may be expected to be more depolarized due to the larger nuclear spin. The linear and circular polarizations for atomic hydrogen (and its isotope) are calculated to be $\sim$0.18 and $\sim$0.12, respectively. The comparison of P_1 in this way, as expected, appears to be incorrect (see Fig. 4.2). However, the prediction for $-P_3/P_e$ of $\sim$0.12 seems to provide an upper bound for the observed value of ($\sim$0.10) near threshold. Similarly, for N the linear and circular polarizations are calculated to be -0.062 and -0.098, respectively. The signs agree and the calculated circular polarization again appears to provide an upper bound for the measured values of $-P_3/P_e$, which are around -0.08 (see Fig. 4.4). Thus, at least for these specific cases, it would appear that there is a fair amount of correlation between the circular polarization of dissociated fragments and that of atoms at threshold.

Chapter 5. Stokes Parameters for Molecular Fluorescence

Measurements of Stokes parameters for molecular transitions excited by spin-polarized electron impact are presented for H_2, D_2, and N_2 targets. The results are compared with previous experimental and theoretical work, and significant existing discrepancies are discussed. Generally, the linear and circular polarizations for molecular fluorescence are found to be less than the typical values for atomic transitions. The second positive system of N_2 exhibits circular polarizations which are consistent with zero, as was mentioned in Chap. 1. Emphasis is placed on the mechanisms responsible for causing the circular polarizations from N_2 to be small compared to those observed from H_2 and D_2.

5.1 Molecular fluorescence from H_2 and D_2

Following the Münster group's null result for the circular polarization from nitrogen's second positive system, our group set out to further explore this topic. In an initial report, Green *et al*. presented the first measurements of non-zero circular polarization for molecular fluorescence from H_2 due to spin exchange [20]. During the course of this work these values have been remeasured, as the original measurements were taken on a different apparatus. The measurements were also extended to include the D_2 isotope. The same optical bandpass filter (600±5 nm FWHM) that was used for the previous work was used again here, for the sake of direct comparison. This optical filter profile is relatively wide, and several different ro-vibrational transitions contribute to the measured Stokes parameters [78–81]. However, in this wavelength region the transitions in H_2 (and D_2)

are largely dominated by the triplet Fulcher-α $d\,^3\Pi_u(v'=0) \rightarrow a\,^3\Sigma_g^+(v''=0)$ band,

$$\begin{aligned} \mathrm{e} + \mathrm{H}_2\, X\,^1\Sigma_g^+ &\rightarrow (1\mathrm{s}\sigma 3\mathrm{p}\pi)\ d\,^3\Pi_u(v'=0) + \mathrm{e} \\ &\rightarrow (1\mathrm{s}\sigma 2\mathrm{s}\sigma)\ a\,^3\Sigma_g^+(v''=0) + \mathrm{e} + \gamma(\sim 600\,\mathrm{nm}). \end{aligned} \tag{5.1}$$

(At room temperature, H_2, D_2, and even N_2 can be considered to occupy only the $v = 0$ vibration state [23].) In a recent paper (published in July 2008), Aguilar *et al.* [81] studied the spectra of H_2 with a spectrometer and reported the cross sections of ro-vibrationally isolated lines for an incident electron energy of 20 eV. This data nicely complements the H_2 wavelength tables that G. H. Dieke generated in the course of his career [79]. Although Dieke's results were obtained with a high resolution spectrometer and remain unsurpassed in terms of wavelength resolution (∼0.004 nm), they were also obtained for discharge conditions. This means that the reported relative intensities do not necessarily correspond to those emitted by room-temperature H_2 excited by mono-energetic electrons. Thus, the intensity spectra of Aguilar *et al.* (which was calibrated to Dieke's wavelengths [81]) are very timely. Their data (shown in Fig. 5.1) indicates that the brightest hydrogen line in the 600 ± 5 nm filter bandpass is the $Q(1)$ transition (labeled "a" in Fig. 5.1) with a cross section of 0.77×10^{-19} cm^2 for 20 eV incident electron energy. This $Q(1)$ transition provides ∼50% of the total measured emission. Here the $Q(N'' = 1)$ transition notation means that the total angular momentum quantum number N of the final state for Hund's case (b) coupling is unity; the letter Q indicates that there is no difference between excited and final state N values, i.e. $\Delta N = N' - N'' = 0$. Similarly, transitions corresponding to $\Delta N = -1$ and $\Delta N = 1$ are labeled as P- and R-branch transitions, respectively. Other significant contributions come from the $Q(2,3)$ and $R(0,1,2)$ lines. For D_2, significant contributions likely come from the $P(2,3)$, $Q(1,2,3,4)$ and $R(0,1,2,3)$ lines [78, 80].

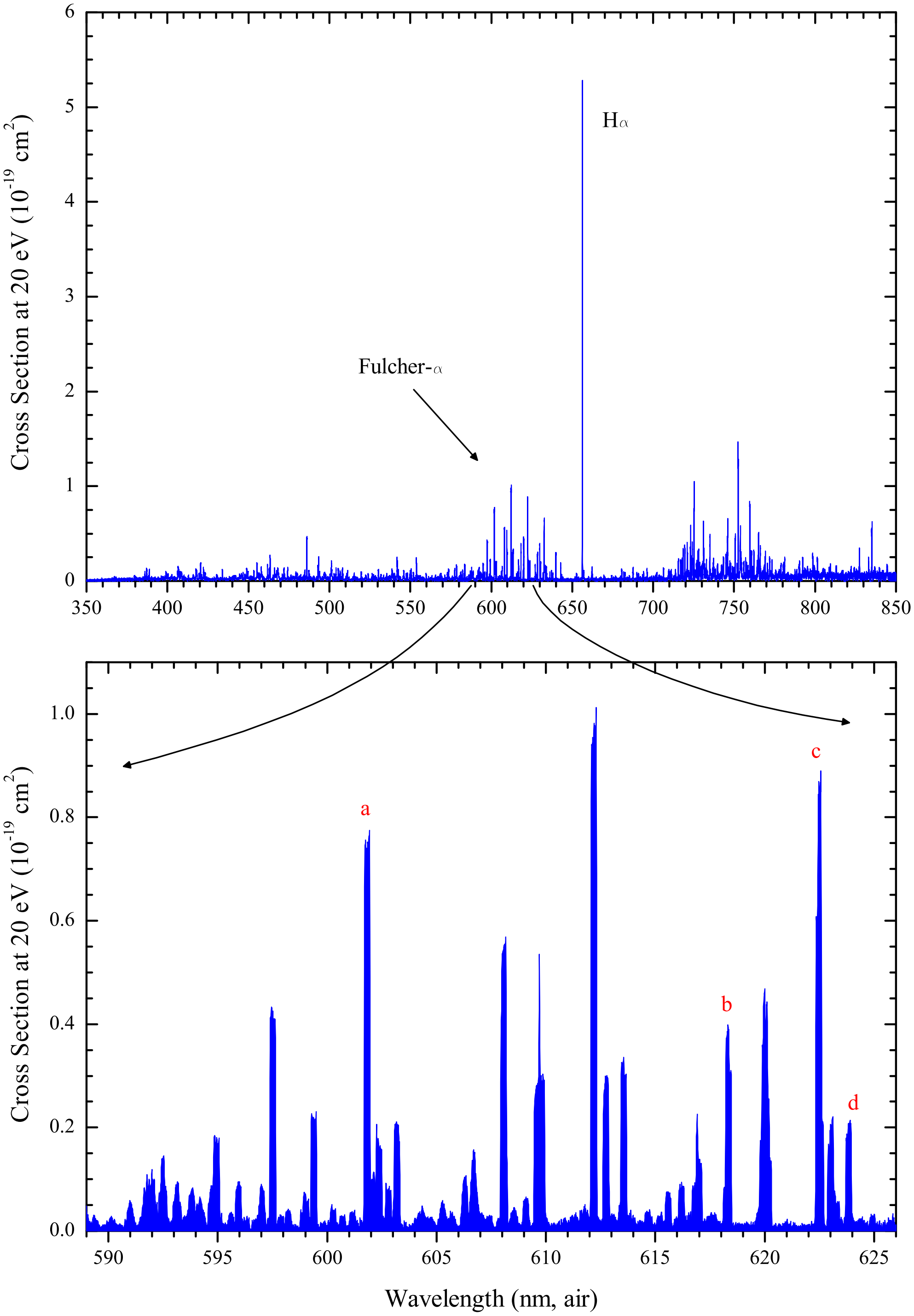

Figure 5.1: Spectra for H_2 excited by 20 eV electron impact [81]. See Table 5.1 for the state assignments of labeled peaks.

Figure 5.2 shows the Stokes parameters for the the H_2 and D_2 lines transmitted by the 600 ± 5 nm bandpass filter. The excitation threshold for the $d\,^3\Pi_u$ ($N' = 1$) state is $\sim$13.9 eV for both H_2 and D_2 [79, 82]. The values of P_2/P_e are consistent with zero. Figure 5.3 provides a comparison of the intensity, P_1, and $-P_3/P_e$ data sets for H_2 and D_2.

The excitation functions decrease sharply at higher energy, characteristic of triplet state (exchange) excitation [83]. A secondary intensity peak appears near 26 eV in the earlier data of Green *et al.*, and this may be due to the fact that the early data was taken at higher pressure (12 mTorr vs 0.5 mTorr) and thus may be susceptible to multiple scattering processes [83]. The linear polarization P_1 is consistent with zero at threshold and is observed to increase with increasing energy. It appears remarkably similar to the observed linear polarization for the H_α line presented in Chap. 4.

The appreciable values of circular polarization for both H_2 and D_2 indicate that significant transfer of spin-to-orbital angular momentum is achieved for these molecules. The earlier $-P_3/P_e$ data for H_2 appears low when compared with the current results. We once again attribute this to the fact that the earlier measurements were taken at a higher pressure and in the presence of a 10^{-2} T magnetic field as discussed in Chap. 4. Direct comparison of the H_2 and D_2 polarization values is problematic due to the fact that several different rotational states are contributing to the measured fluorescence, and the different states will generally exhibit varying degrees of polarization. However, this data does represent a lower bound for $-P_3/P_e$ values from the individual lines with the largest circular polarizations.

5.1.1 Stokes parameters for rotationally-isolated transitions

In order to further explore the Stokes parameters from molecular transitions in H_2 and D_2, isolation of individual ro-vibrational lines was required. This was accomplished by purchasing custom optical interference filters from Andover Corporation designed to

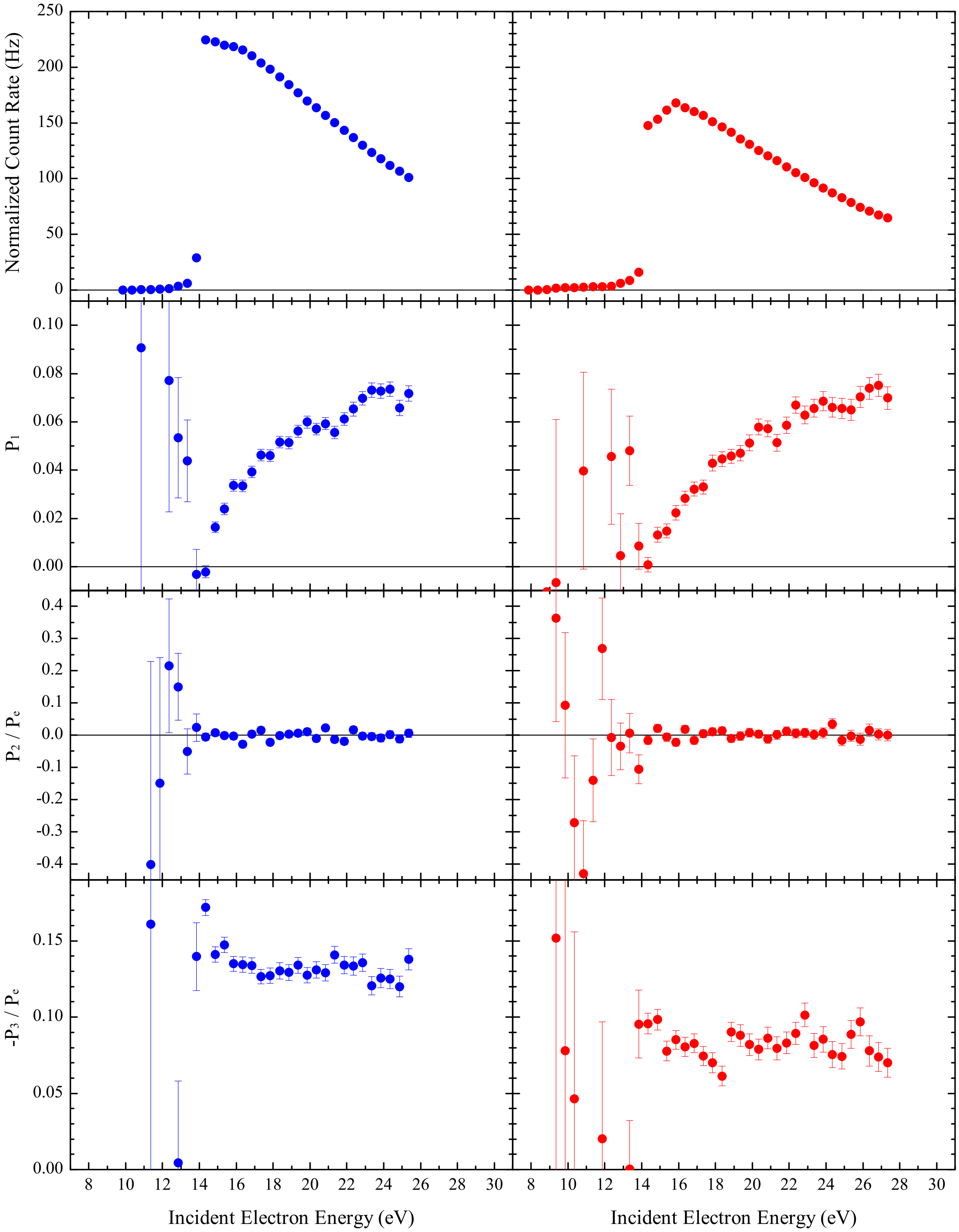

Figure 5.2: Stokes parameters for unresolved H_2 (at left) and D_2 (at right) transitions acquired with a 600±5 nm FWHM optical bandpass filter. The data was acquired at a pressure of 0.5 mTorr. For this wavelength range the fluorescence is largely due to the Fulcher-α $d\,^3\Pi_u(v'=0) \rightarrow a\,^3\Sigma_g^+(v''=0)$ band (see text).

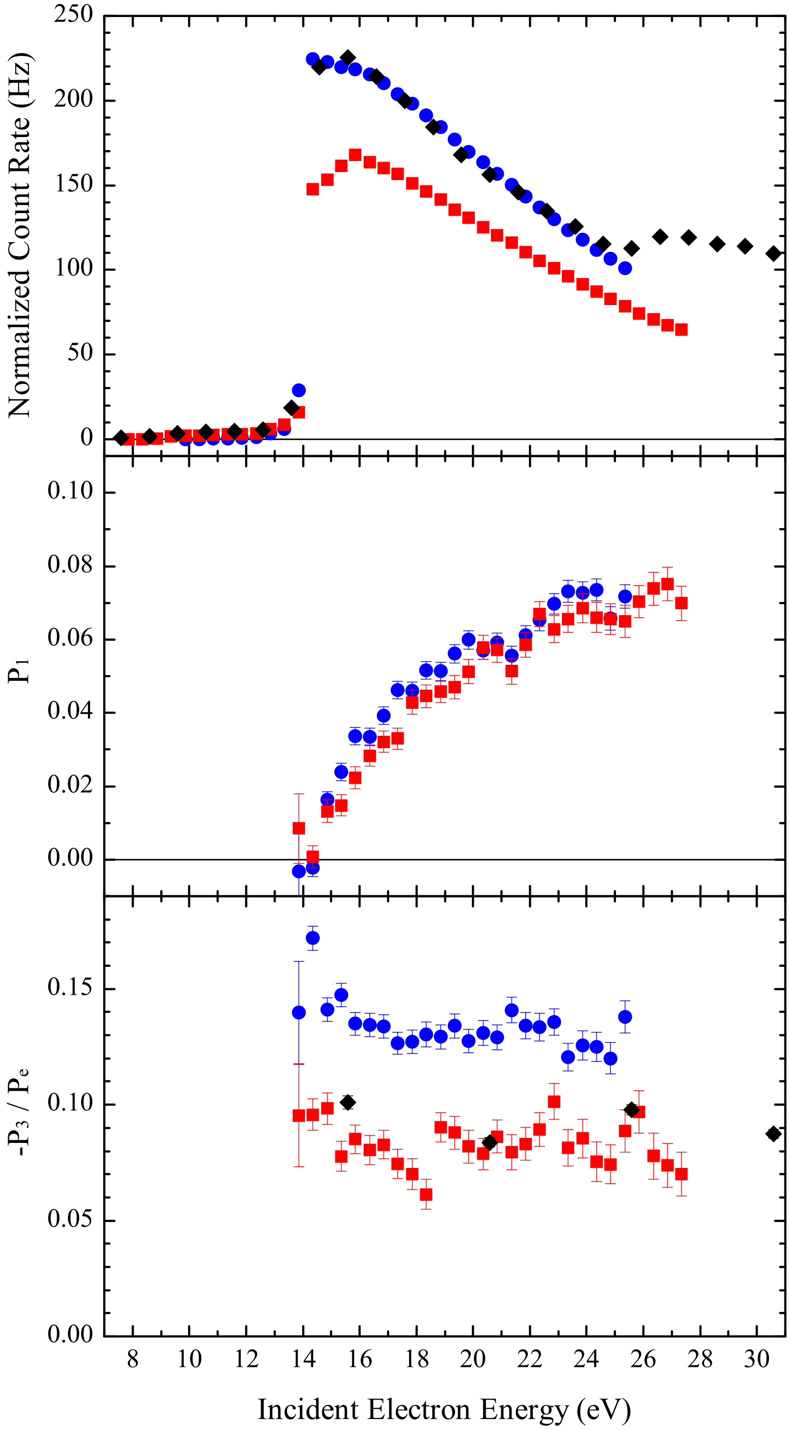

Figure 5.3: Comparison of H_2 (circles) and D_2 (squares) data from Fig. 5.2 with the earlier results of Green *et al.* [20] (diamonds). Polarizations below 13.8 eV are omitted for clarity.

Table 5.1: Rotationally-isolated transitions in the $d\,^3\Pi_u \rightarrow a\,^3\Sigma_g^+$ (0 – 0) and (2 – 2) vibrational bands of H_2 and D_2. Wavelengths were taken from Refs. [79] and [80].

Species	Wavelength (air)	Label in Fig. 5.1	$(v' \rightarrow v'')$, $Q(N'')$, $R(N'')$
D_2	600.681	—	$(0-0)\ Q(3)$
H_2	601.830	a	$(0-0)\ Q(1)$
H_2	618.299	b	$(2-2)\ R(1)$
H_2	622.482	c	$(2-2)\ Q(1)$
H_2	623.839	d	$(2-2)\ Q(3)$

have the narrowest bandpass possible (0.14 nm FWHM). Five transitions (four in H_2 and one in D_2) were chosen for investigation, based on criteria such as the expected intensity and level of achievable isolation from other transitions. The final selected candidates are listed in Table 5.1, and consist of transitions in the $d\,^3\Pi_u \rightarrow a\,^3\Sigma_g^+$ $(0-0)$ and $(2-2)$ vibrational bands of H_2 and D_2. The data acquired for each of the transitions listed in Table 5.1 are shown in Figs. 5.4, 5.5, and 5.6. The energy-averaged value of P_2/P_e for the H_2 $(2-2)$ $Q(3)$ transition is 0.057(26), which is 2.2σ from zero; the other four data sets all have P_2/P_e values consistent with zero. The intensity, P_1, and $-P_3/P_e$ values for the five data sets are compared in Fig. 5.7.

The excited $d\,^3\Pi_u$ state is split due to Λ doubling, and the two levels are denoted as $d\,^3\Pi_u^-$ and $d\,^3\Pi_u^+$ states. Consideration of nuclear spin statistics reveals that the Q-transitions in H_2 and D_2 can only involve the $d\,^3\Pi_u^-$ state while the H_2 R-transitions involve the $d\,^3\Pi_u^+$ state, which is known to be perturbed by the $(1s\sigma 2s\sigma)\ e\,^3\Sigma_u^+$ state [84]. The total nuclear spin T for the five measured H_2 and D_2 transitions is 1, which means that similar hyperfine depolarization should be expected for each case.

The linear polarization comparison in Fig. 5.7 indicates that the data for the two separate $Q(1)$ transitions from different vibrational bands is quite similar, and in fact the polarization is not expected to depend significantly on the vibrational state quantum number [85]. The $Q(3)$ and $R(1)$ transitions appear to have even larger values of P_1, and

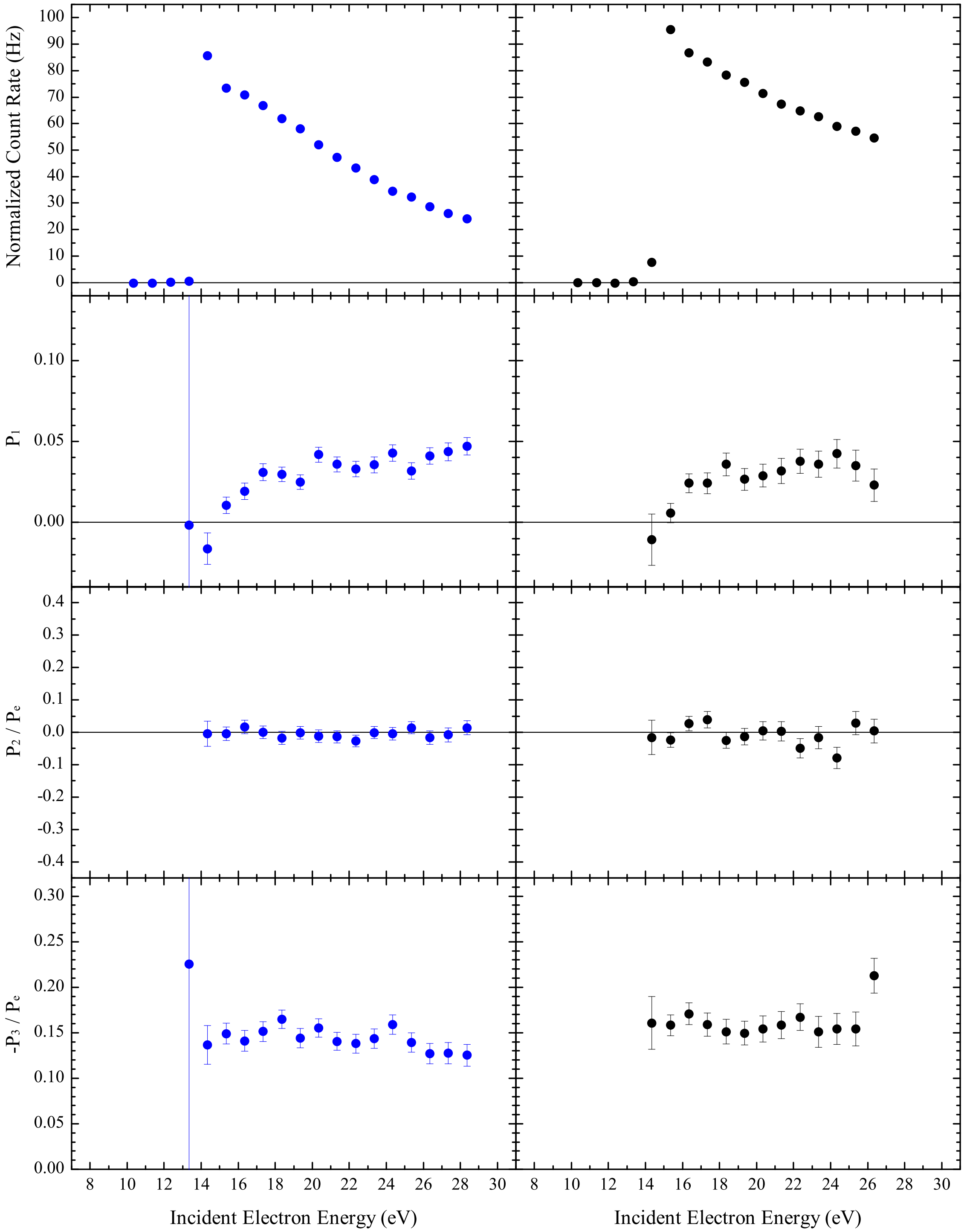

Figure 5.4: Stokes parameters for the H_2 Fulcher-α $d\,^3\Pi_u^- \rightarrow a\,^3\Sigma_g^+$ $Q(1)$ lines: (0 − 0) vibrational band data on the left, (2 − 2) data on the right. Data was acquired at a pressure of 0.7 mTorr.

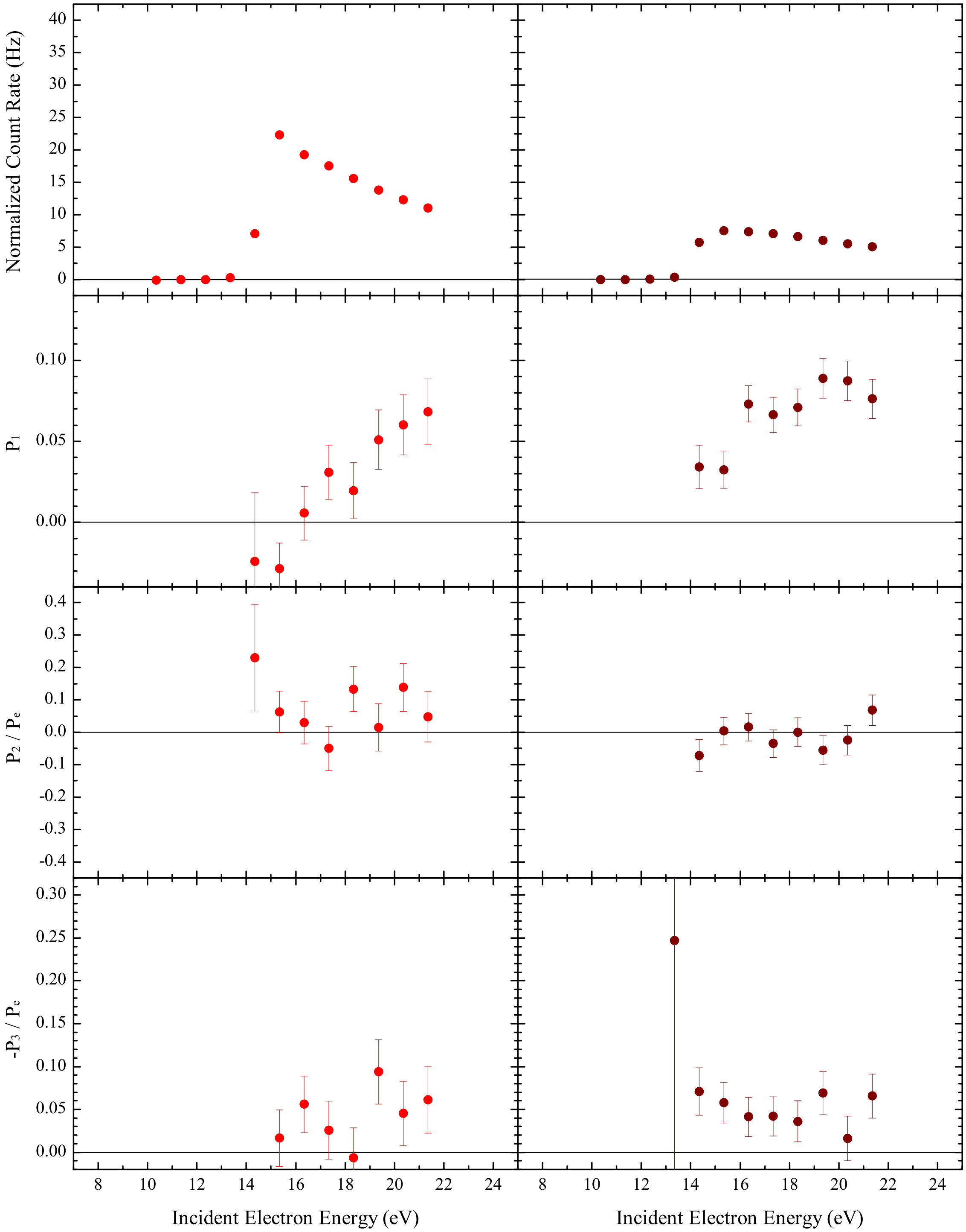

Figure 5.5: Stokes parameters for the Fulcher-α $d\,^3\Pi_u^- \rightarrow a\,^3\Sigma_g^+$ $Q(3)$ lines: H_2 $(2-2)$ vibrational band data on the left, D_2 $(0-0)$ data on the right. Data was acquired at a pressure of 0.7 mTorr.

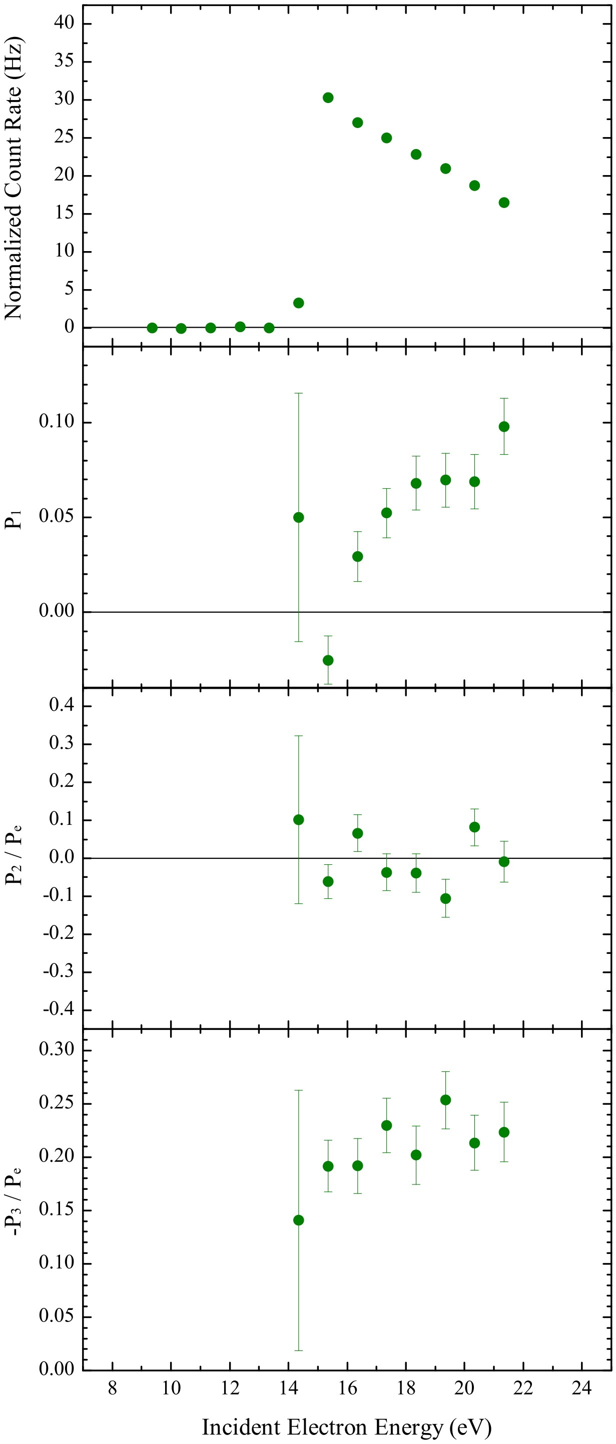

Figure 5.6: Stokes parameters for the Fulcher-α $d\,^3\Pi_u^+ \rightarrow a\,^3\Sigma_g^+$ $(2-2)$ $R(1)$ line. Data was acquired at a pressure of 0.7 mTorr.

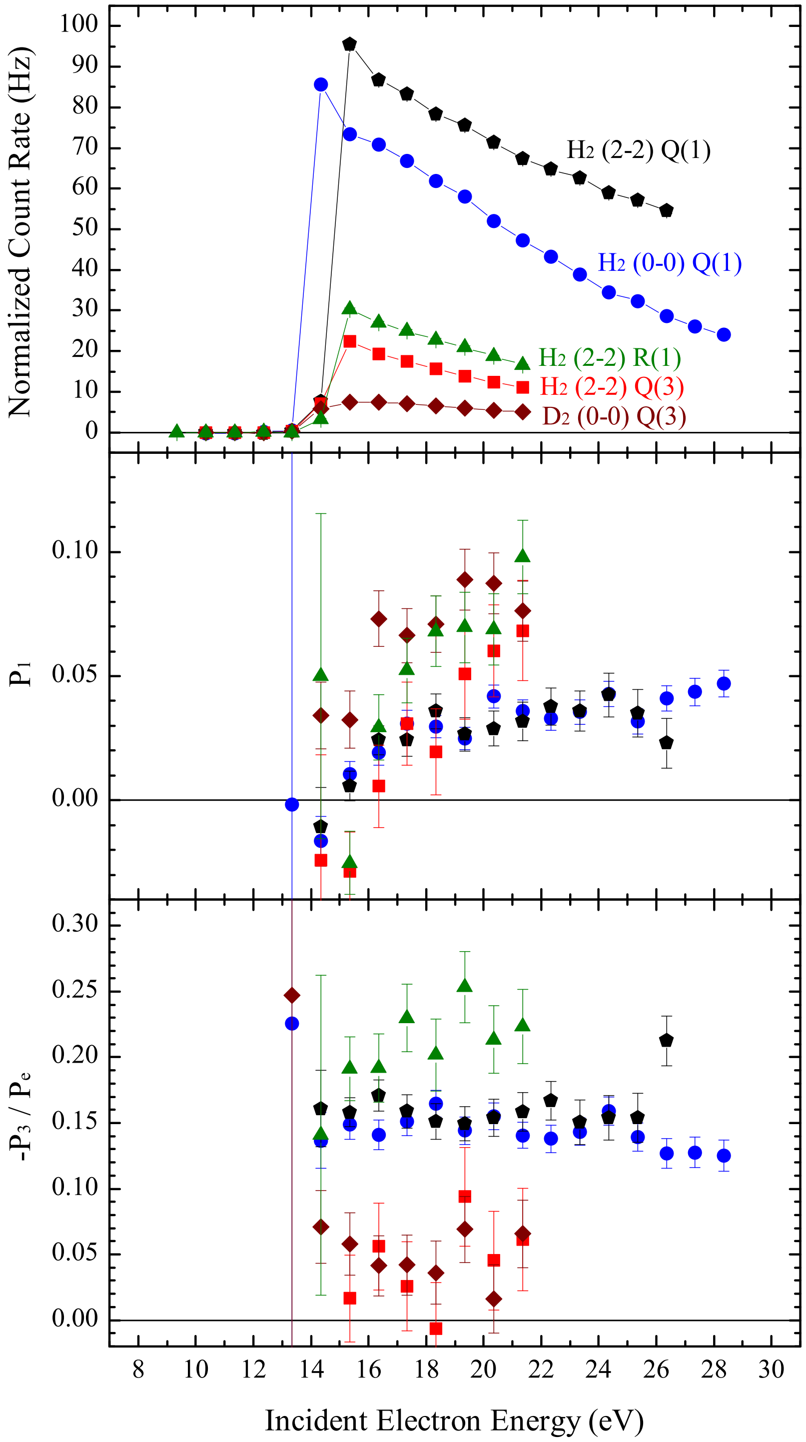

Figure 5.7: Comparison of H_2 and D_2 data from Figs. 5.4, 5.5, and 5.6 for rotationally isolated transitions in the $d\,^3\Pi_u \rightarrow a\,^3\Sigma_g^+$ system. Data sets are labeled in the uppermost plot.

due to the lower cross sections for these lines the statistical uncertainties are larger. Previous experimental results for the linear polarization of the $Q(1)$ transitions are available, as well as a more recent theoretical calculation. The early experimental results (1967) of Cahill *et al*. [86] (which represent the first polarization measurement for single-collision-induced molecular fluorescence) are presented in Figure 5.8 along with the the work of Baltayan *et al*. [84], McConkey *et al*. [87], and the theoretical calculation by Meneses *et al*. [85]. The large P_1 values found by Cahill *et al*. are roughly a factor of two greater than results from the more recent experiments. The polarizations found by this work do not seem to agree well with the theoretical calculation; the experimental values indicate that $-0.01 \leqslant P_1 \leqslant 0.01$ near threshold and increases at higher energy, while the calculation gives a maximum polarization at threshold.

To calculate P_1, Meneses *et al*. have applied the Stokes parameter formalism provided by Blum and Jakubowicz [88]. This is analogous to the atomic formalism for the Stokes parameters reviewed in Appendix B, but deals with Hund's case (b) molecular systems. The Blum and Jakubowicz paper focuses on the theoretical treatment of "coincidence" experiments (where outgoing electrons are detected in coincidence with emitted photons), but also detail the integration over all scattering angles required to predict the linear polarization P_1 which is of interest here. (Unfortunately the Blum and Jakubowicz paper does not account for the use of incident spin-polarized electrons, which would be required to predict the circular polarizations measured here.) As discussed in Appendix B, the atomic formalism allows for the threshold linear and circular polarizations to be computed rather simply. This is due to the fact that all of the magnetic sublevel excitation cross sections Q_M with $M = M_L \neq 0$ are required to vanish at threshold due to angular momentum conservation considerations. Blum and Jakubowicz pointed out that for molecules, the ground state angular momentum is typically non-zero (due to thermal rotational state populations). Thus threshold polarizations cannot be easily calculated

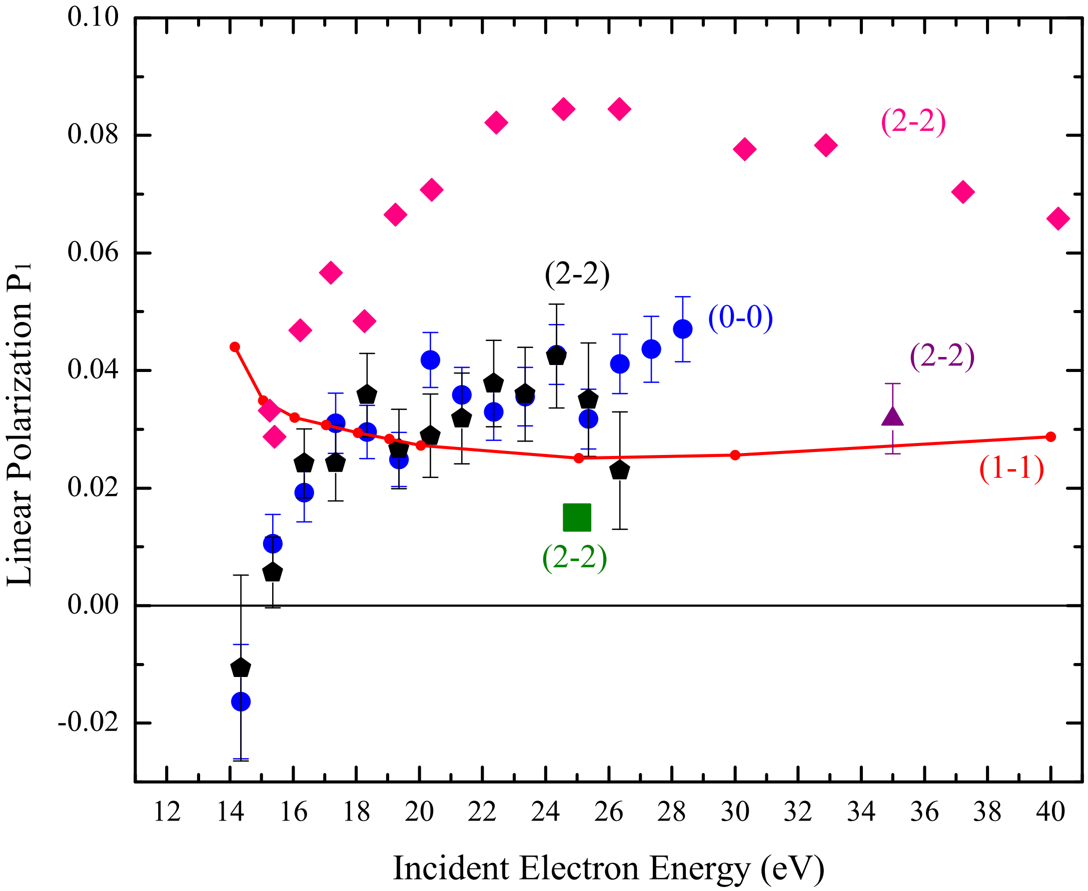

Figure 5.8: Comparison of the experimental results for the H_2 $d\,^3\Pi_u^- \rightarrow a\,^3\Sigma_g^+$ $Q(1)$ lines. Diamonds: Cahill *et al.* [86]; triangle: Baltayan *et al.* [84]; square: McConkey *et al.* [87] (uncertainty not reported); linespoints: theoretical calculation of Meneses *et al.* [85]; current results: circles and pentagons. The quantum numbers for the excited and final vibrational states are labeled as $(v' - v'')$.

like in the atomic case, because the polarizations generally depend on the relative contributions of Q_M cross sections. Meneses *et al.* used the Blum and Jakubowicz formalism to obtain the dependence of P_1 on Q_M (where M now refers to the projection of quantum number N on the electron beam axis):

$$P_1 = \frac{-3G_2(Q_0 - Q_1)}{(4G_0 - G_2)Q_0 + (8G_0 + G_2)Q_1}. \tag{5.2}$$

Here the Gs refer to the time-integrated depolarization perturbation coefficients that account for the effect of fine- and hyperfine-structure depolarization. These were computed by McConkey *et al.* [87] for this H_2 $Q(1)$ transition and found to be $G_0 = 0.962$ and $G_2 = 0.115$. Meneses *et al.* then performed the distorted wave approximation (DWA) technique to calculate the values of Q_0 and Q_1 as a function of incident electron energy. They considered excitation and decay with $N = N' = N'' = 1$ and found that the Q_0 contribution vanishes at threshold, which gives $P_{1\text{thr}} = 0.044$ (see Fig. 5.8). This vanishing of Q_0 is consequence of the $\Sigma \to \Pi$ excitation character, which is referred to as a "perpendicular" transition [89], but should not generally be expected to hold for any excitation process.

The origin of the observed discrepancy between the current experimental P_1 values and the calculation by Meneses *et al.* remains unclear. At threshold, cascade contamination of the polarization cannot come into play. (Note that Baltayan *et al.* [84] have estimated an upper bound on cascade contribution to the $d\,^3\Pi_u$ state of 17% at 35 eV.) It is possible that excitation of $N = 3$ ground states ($N =$even contribution is forbidden due to ortho/para considerations) has a non-zero contribution to the experimental results, but this has historically been discounted for H_2 [90] as it is a non-dipole excitation channel. However, Bingjia *et al.* [91] indicate that the relative amount of $N = 3 \to N' = 1$ state excitation may be ∼8%. It is unclear whether such contribution could account for the discrepancy. It has also been suggested that such discrepancies can be due to depolarizing effects of near-threshold resonances or long-range electron-electron correlations [92]. In any event, the current disagreement highlights the need for further investigation.

The $-P3/Pe$ values shown in Fig. 5.7 represent the first measurements of circular polarization for rotationally-isolated molecular fluorescence. As discussed above, the molecular polarization theory by Blum and Jakubowicz does not account for the use of spin-polarized electrons, and this non-trivial extension of the formalism has not yet been undertaken. Even if such a formalism existed, numerical calculations would still be required in order to obtain the individual magnetic sublevel contributions. Thus, the results are only discussed quantitatively here.

The circular polarizations exhibit a relatively flat energy dependence up to 15 eV above threshold. This suggests that they do not strongly depend on the alignment (which varies significantly over this energy range). The largest spin-normalized circular polarizations are observed for the $R(1)$ line, with an energy-averaged value of $-P_3/P_e \sim 0.21$. The empirical implication is that R-branch fluorescence yields larger circular polarizations than Q-branch fluorescence. However, it should be remembered that the R-lines come from the perturbed $d\,^3\Pi_u^+$ state, and it is unknown as to what the effects of this perturbation mean regarding polarization comparisons with fluorescence from the unperturbed $d\,^3\Pi_u^-$ level. The $Q(1)$ lines from the two different vibrational bands yield circular polarizations which are quite similar: $-P_3/P_e \sim 0.15$. The two $Q(3)$ lines also give similar results, but these values are much smaller: $-P_3/P_e \sim 0.045$. The only apparent difference between the $Q(N'' = 1)$ and $Q(N'' = 3)$ situations is that N is larger for the $Q(3)$ lines. Figure 5.9 illustrates semiclassical angular momentum coupling cases (for small and large $\boldsymbol{N}$) described by Hund's case (b). An initially isotropic $\boldsymbol{N}$ distribution describes the ground state. Upon exchange excitation, the oriented $\boldsymbol{S}$ couples with $\boldsymbol{N}$ (shown as isotropic here, but will generally be aligned by the excitation process) to form

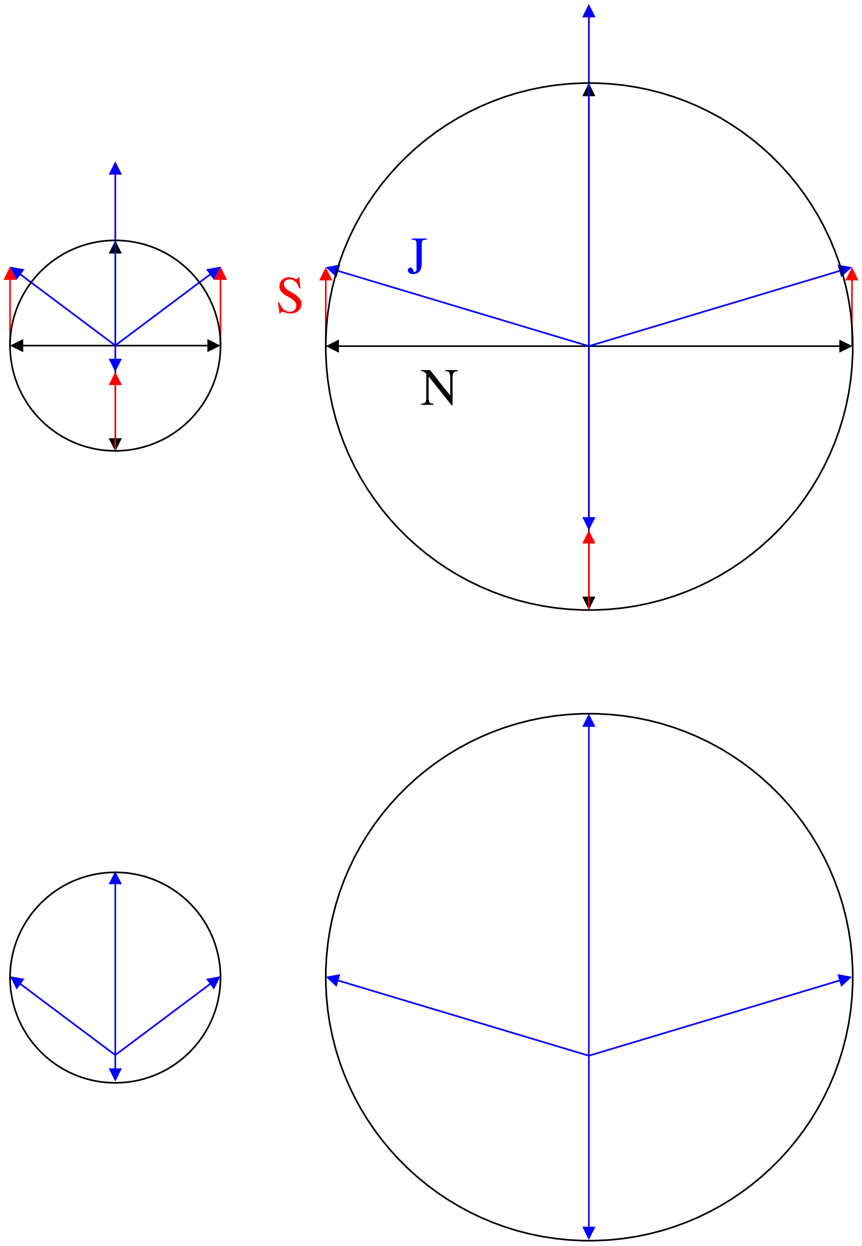

Figure 5.9: Isotropic distributions of angular momenta N (of different magnitudes) couple with oriented electron spin S to form J. Greater orientation of J is achieved for the case where N is smaller.

$\boldsymbol{J}$. Blum [18] has shown that in the high-J limit, the orientation parameter (related to the magnitude of observed circular polarization) is proportional to the value of cos(θ) averaged over the $\boldsymbol{J}$ vector distribution (where θ is taken with respect to the electron beam axis and $0 \leqslant \theta \leqslant \pi$). Thus, from Fig. 5.9, it is apparent that smaller N values yield larger circular polarizations when coupled with oriented $\boldsymbol{S}$. The observed $Q(3)/Q(1)$ polarization ratio (∼0.3) is similar to the ratio of the corresponding N values (∼0.33).

5.2 Molecular fluorescence from N_2

In the first attempt to detect circular polarization from molecules excited by spin polarized electron impact, the Münster group was unable to observe non-zero values of $-P_3/P_e$ from the N_2 second positive system. This original result stands in contrast to the significant circular polarizations observed from H_2 and D_2 molecules. A verification of the original nitrogen experiment is presented here, and some explanation is offered to account for the apparent lack of orientation transfer. The results of two more experiments which have provided non-zero circular polarizations are then detailed.

5.2.1 Stokes parameters for the N_2 second positive system

The Münster group measured the circular polarization for the N_2 $C\,{}^3\Pi_u(v' = 0) \rightarrow B\,{}^3\Pi_g(v'' = 0)$ 337.1 nm band (second positive system) excited by spin-polarized electrons. We have measured the $(0-2)$ band of this system,

$$\begin{aligned} e + N_2 X\,{}^1\Sigma_g^+(v=0) &\rightarrow C\,{}^3\Pi_u(v'=0) + e \\ &\rightarrow B\,{}^3\Pi_g(v''=2) + e + \gamma(\sim 380.5\,\text{nm}). \end{aligned} \tag{5.3}$$

This difference in vibrational bands is not expected to significantly affect the Stokes parameters, or invalidate a comparison with the Münster results. The data was acquired at a pressure of 0.3 mTorr. Figure 5.10 compares the results of the two experiments. The energy-averaged values of $-P_3/P_e$ are -0.004 ± 0.002 and -0.003 ± 0.001 for the present work and the Münster results, respectively.

To understand why the circular polarization is so minuscule, we first recall the discussion for H_2 in which it was noted that large values of N (or J) tended to lower the amount of observed polarization. The large values of rotational angular momenta in room temperature N_2 should be expected to lower the observed polarizations. Figure 5.11 gives the rotational state populations of the H_2, D_2, and N_2 $X\ {}^1\Sigma_g^+$ ground states at room temperature (taken to be 25 °C). The population oscillations observed between even and odd J values are due to the inclusion of nuclear spin statistics. The weighted means of the J values (where the populations are the weighting factors) in H_2, D_2, and N_2 are approximately 1.2, 1.8, and 8.5, respectively.

Next, a consideration of the measured rotational transitions is in order. For this experiment, the interference filter bandpass (380.1 ± 3.5 nm FWHM) transmitted all the rotational lines with only a slight discrimination of R-branch intensities corresponding to large J. Figure 5.12 depicts the spectrum as computed following the method described in Ref. [93], using the updated C and B state molecular constants reported in Ref. [94]. The upper panel shows the wavelength dependence of the $P(J'')$-, $Q(J'')$-, and $R(J'')$-branches. The branches have three sub-branches, corresponding to ${}^3\Pi_0 \rightarrow {}^3\Pi_0$, ${}^3\Pi_1 \rightarrow {}^3\Pi_1$ and ${}^3\Pi_2 \rightarrow {}^3\Pi_2$ transitions (the ${}^3\Pi_0 \rightarrow {}^3\Pi_0$ Q-branch is forbidden [23]). The lower panel shows the intensities as a function of wavelength, and for this plot the transmission profile of the optical filter we used has been taken into account.

Friedrich Hanne has pointed out that orientation of $\boldsymbol{S}$ cannot lead to orientation of $\boldsymbol{J}$ for the Hund's case (a) situations where $\Omega = 0, 1$ (see Figs. 1.1d and 1.1e on p. 7) [96]. Thus, no circular polarization can be produced from the Hund's case (a) ${}^3\Pi_0 \rightarrow {}^3\Pi_0$ and ${}^3\Pi_1 \rightarrow {}^3\Pi_1$ sub-bands. However, orientation of J can be achieved for the case where

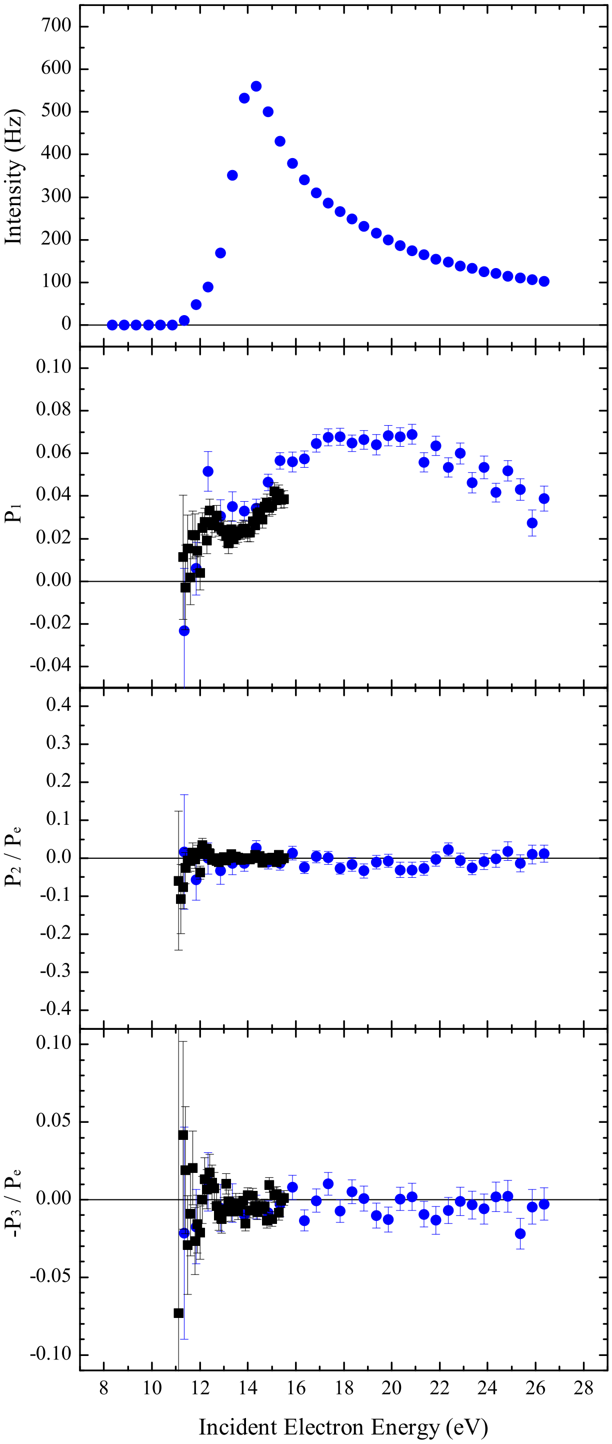

Figure 5.10: Stokes parameters for the N_2 $C\,^3\Pi_u \rightarrow B\,^3\Pi_g$ second positive system. Data of this work for the $(0-2)$ 380.5 nm band is represented by circles and was acquired at a pressure of 0.3 mTorr. The Münster result for the $(0-0)$ 337.1 nm band is shown in squares [19].

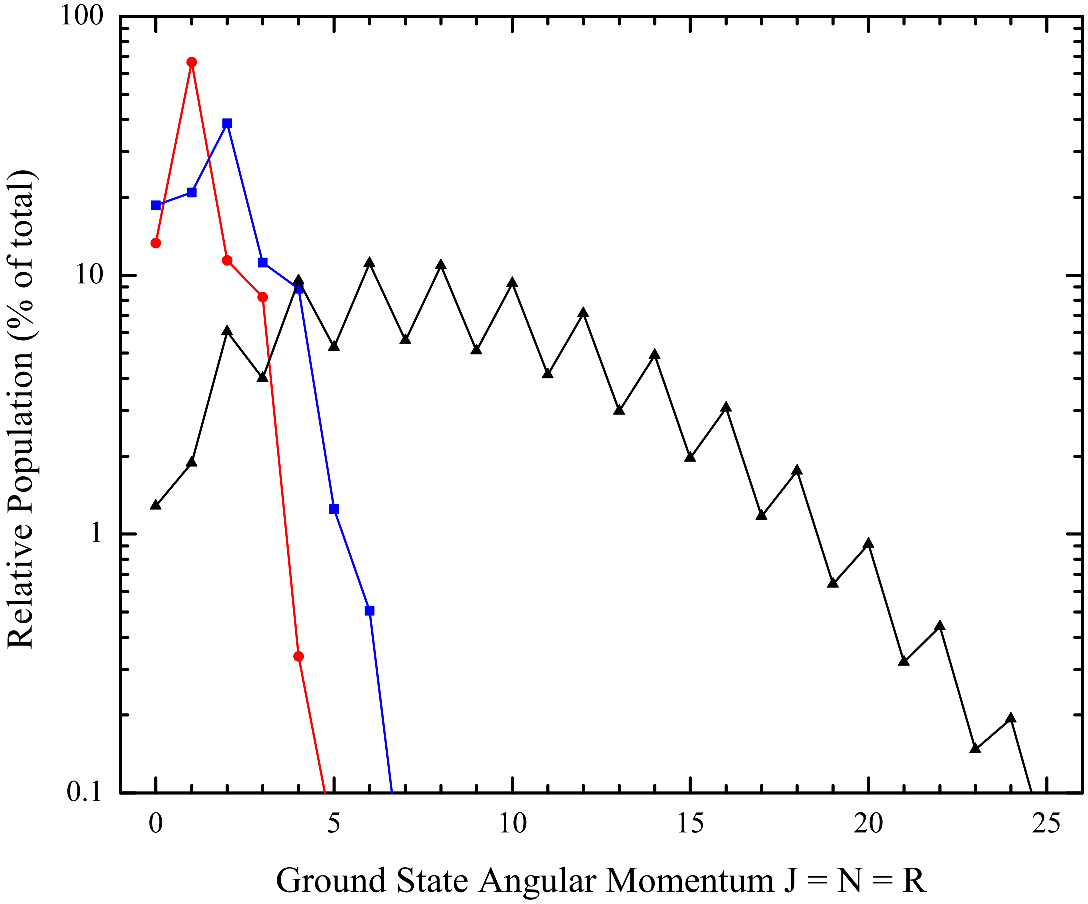

Figure 5.11: Ground state $X\,^1\Sigma_g^+$ population distributions at room temperature (298.16 K) for H_2 (circles), D_2 (squares), and N_2 (triangles). Nuclear spin statistics are included. The smaller alternating population values correspond to para nuclear spin states, and larger values represent ortho states. The mean-intensity values of J for H_2, D_2, and N_2 are 1.2, 1.8, and 8.5, respectively.

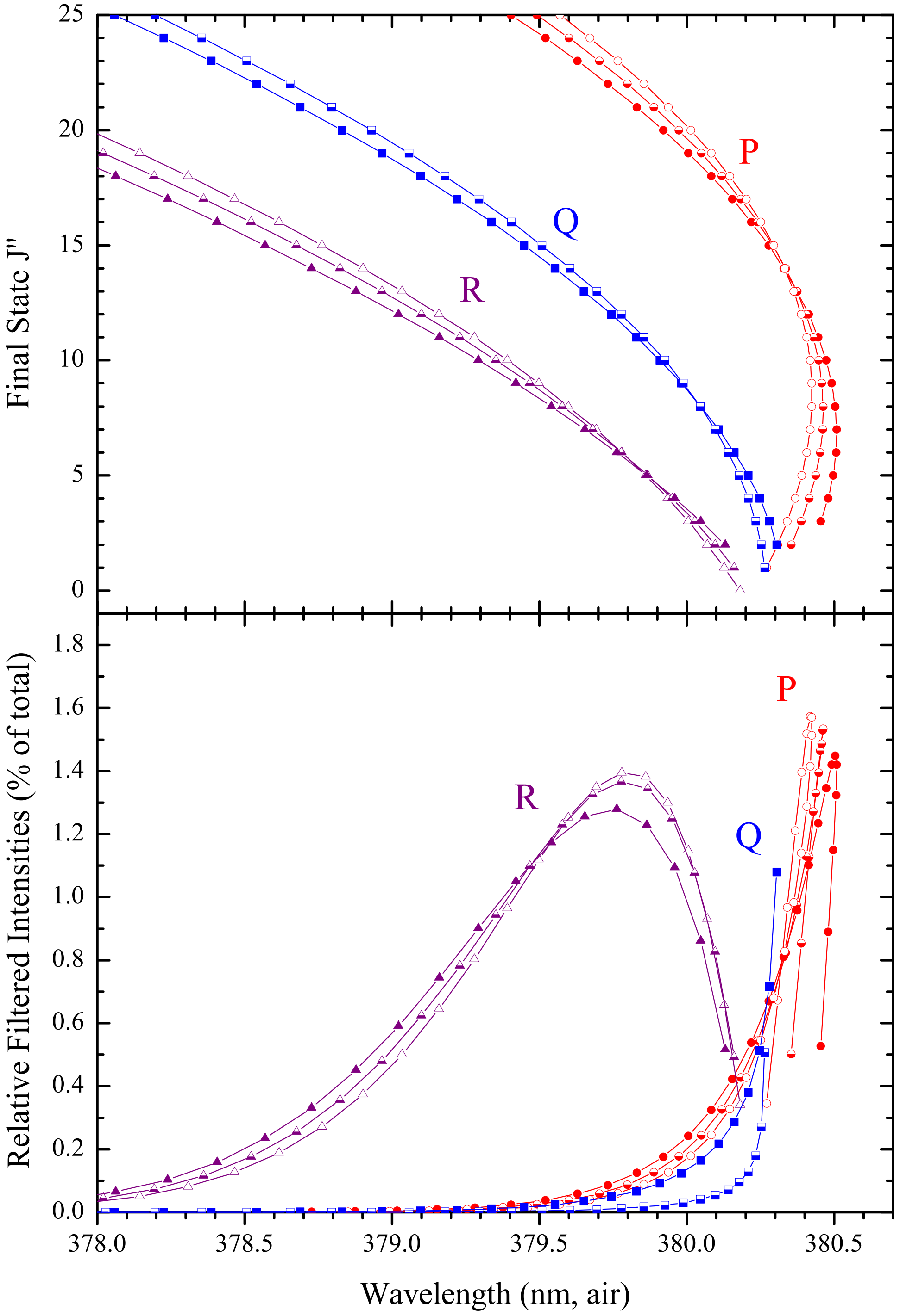

Figure 5.12: Upper panel: $P(J'')$, $Q(J'')$, and $R(J'')$ branches for the N_2 second positive $(0-2)$ 380.5 nm system. The empty, half-filled, and filled points correspond to the $\Omega = 0, 1, 2$ sub-bands, respectively (see text). Lower panel: Intensities for branch J'' values (modified by the bandpass filter transmission) as computed using the method described in Ref. [93] for room-temperature N_2. This simplified spectra neglects Λ-doubling and weak $\Delta\Omega \neq 0$ transitions [95].

$\Omega = 2$; thus non-zero P_3 was expected [19], even though it was realized that it would be lowered by a factor of ~ 3 due to the unoriented $^3\Pi_0 \rightarrow {}^3\Pi_0$ and $^3\Pi_1 \rightarrow {}^3\Pi_1$ sub-bands. (Due to spin uncoupling, or the transition of the C and B states from Hund's case (a) to Hund's case (b) with increasing J [23], it is likely that the $^3\Pi_0 \rightarrow {}^3\Pi_0$ and $^3\Pi_1 \rightarrow {}^3\Pi_1$ sub-bands actually can contribute non-zero circular polarization for large J.) The Q-branches are weak (see Fig. 5.12): their relative intensity contributions are only ~5% of the total emission. Thus, the measured Stokes parameters are mainly due to the R- and P-branches. The P- to R-branch intensity ratios are ~1.3, meaning they have similar contributions.

We now consider the sign of $-P_3/P_e$ values for P- vs. R-branch fluorescence. The definition of P- and R-branches in conjunction with conservation of angular momentum suggests that $-P_3/P_e$ for the P- and R-branches should have opposite signs. For a P-branch transition, $\Delta J(\text{or } \Delta N) = -1$, while the R-branch case has $\Delta J(\text{or } \Delta N) = 1$. The molecular angular momentum $\boldsymbol{J}$ is oriented due to $\boldsymbol{S}$ in a direction parallel to that of the spin polarization of the incident electron beam. Figure 5.13 illustrates an initially oriented $\boldsymbol{J}$ which yields outgoing photon helicities of opposite sign for the P- and R-branches upon fluorescence. This indicates that the sign of $-P_3/P_e$ should be positive for R-branch transitions and negative for P-branch fluorescence.

So it appears that several effects can work to prohibit a net transfer of spin angular momentum to photon circular polarization. Depolarization occurs due to the relatively large values of angular momentum (with which the oriented spin couples to). Also,

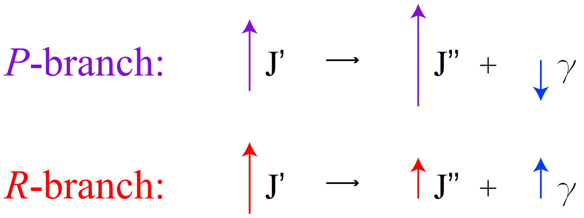

Figure 5.13: Initially oriented angular momentum $\boldsymbol{J}$ yielding photons with opposite helicites from the P- and R-branches upon fluorescence.

Hund's case (a) states are less oriented than those of Hund's case (b), because some of the sub-bands cannot acquire orientation due to the initially oriented $\boldsymbol{S}$. Finally, P-/R-branch averaging tends to force P_3 values to zero. Here we note that if the Q-branch was brighter, P-/R- branch averaging would not be able to nullify the net circular polarization. For this experiment wherein the entire rotation structure was detected and the Q-branch did not play a large role, no net orientation of the emitted photons was observed.

5.2.2 Stokes parameters for the N_2 first negative system

To further address the question of whether circularly polarized fluorescence can be observed in molecular nitrogen, the first negative band was studied, with the aim of partial rotational isolation. This band is accessed by the excitation-ionization reaction

$$\begin{aligned} \mathrm{e} + \mathrm{N}_2\, X\, {}^1\Sigma_g^+(v=0) &\rightarrow \mathrm{N}_2^+\, B\, {}^2\Sigma_u^+(v'=0) + 2\mathrm{e} \\ &\rightarrow \mathrm{N}_2^+\, X\, {}^2\Sigma_g^+(v''=0) + 2\mathrm{e} + \gamma(\sim 391.4\,\mathrm{nm}). \end{aligned} \tag{5.4}$$

Since the molecular states of interest are all of Σ character, the angular momentum coupling is described by Hund's case (b). Figure 1.1b depicts this coupling scheme, wherein the vectors $\boldsymbol{N}$ and $\boldsymbol{S}$ couple to form the spatially-fixed $\boldsymbol{J}$ (total angular momentum excluding nuclear spin). Vectors $\boldsymbol{N}$ and $\boldsymbol{S}$ precess about the spatially-fixed $\boldsymbol{J}$ with a period of <0.1 ns (N=1) corresponding to the $\gamma(\boldsymbol{N} \cdot \boldsymbol{S})$ "spin-doubling" term in the molecular Hamiltonian [97]. This spin-rotation coupling timescale is much less than the lifetime of the $B\, {}^2\Sigma_u^+$ system (61 ns [98]), so time-averaged orientation of $\boldsymbol{N}$ can develop.

This experiment demonstrates that the collision-induced orientation of $\boldsymbol{N}$, and hence P_3 production, is possible even in the absence of electronic orbital angular momentum along the internuclear axis ($\Lambda = 0$ and $\boldsymbol{N} = \boldsymbol{R}$). The mechanisms responsible for this torque on the molecular nuclei are the direct coupling of $\boldsymbol{S}$ to the magnetic field produced by the "current loop" of nuclear rotation, as well as the coupling of $\boldsymbol{S}$ to the residual electronic orbital angular momentum perpendicular to the internuclear axis, which also produces a magnetic field along $\boldsymbol{N}$ [99–101]. (The latter mechanism can also be attributed to nuclear rotation, however, in that it requires uncoupling of the total electron orbital angular momentum, $\boldsymbol{L}$, from the internuclear axis.) To date, the effects of these rotational couplings have only been observed as spin doubling in molecular spectra [23], although they have been discussed as a possible mechanism for spin relaxation in triplet alkali dimers [102, 103].

The polarization of molecular fluorescence depends on the rotational transitions observed. To illustrate the optical sensitivity, Fig. 5.14 shows a spectrum for the N_2^+ $B\,{}^2\Sigma_u^+(v' = 0) \rightarrow X\,{}^2\Sigma_g^+(v'' = 0)$ band excited by electron bombardment [104]. As expected, there is a 2:1 intensity alternation of even N'' vs. odd N'' rotational transitions due to the nuclear spin statistics of ${}^{14}N_2$ [23]. The effect of the narrow bandpass filter (391.6 ± 0.92 nm FWHM) used for this experiment is shown in the lower plot, indicating that the data is due only to P-branch ($N' - N'' = -1$) fluorescence, the R-branch ($N' - N'' = +1$) being almost completely suppressed. Also, transitions near the band head $P(N''{\sim}14)$ are preferentially detected. No significant contaminant molecular or atomic lines are expected to co-exist in the profile of the bandpass filter. A transition in the N_2 Goldstein-Kaplan $C'\,{}^3\Pi_u(v' = 0) \rightarrow B\,{}^3\Pi_g(v'' = 8)$ system at 391.5 nm exists, but it is apparently much weaker than the transition under study, as negligible intensity from this band appears below the threshold for $B\,{}^2\Sigma_u^+$ state production.

The Stokes parameters presented in Fig. 5.15 were acquired at a pressure of 0.3 mTorr to avoid potential effects of radiation trapping. Cascade contributions from higher-lying states are not expected [107]. The P_1 values are consistent with those of Ref. [105], but the interference filter used in that work transmitted both the P- and most of the R-branch fluorescence. It is difficult to assess what the kinematically-required threshold

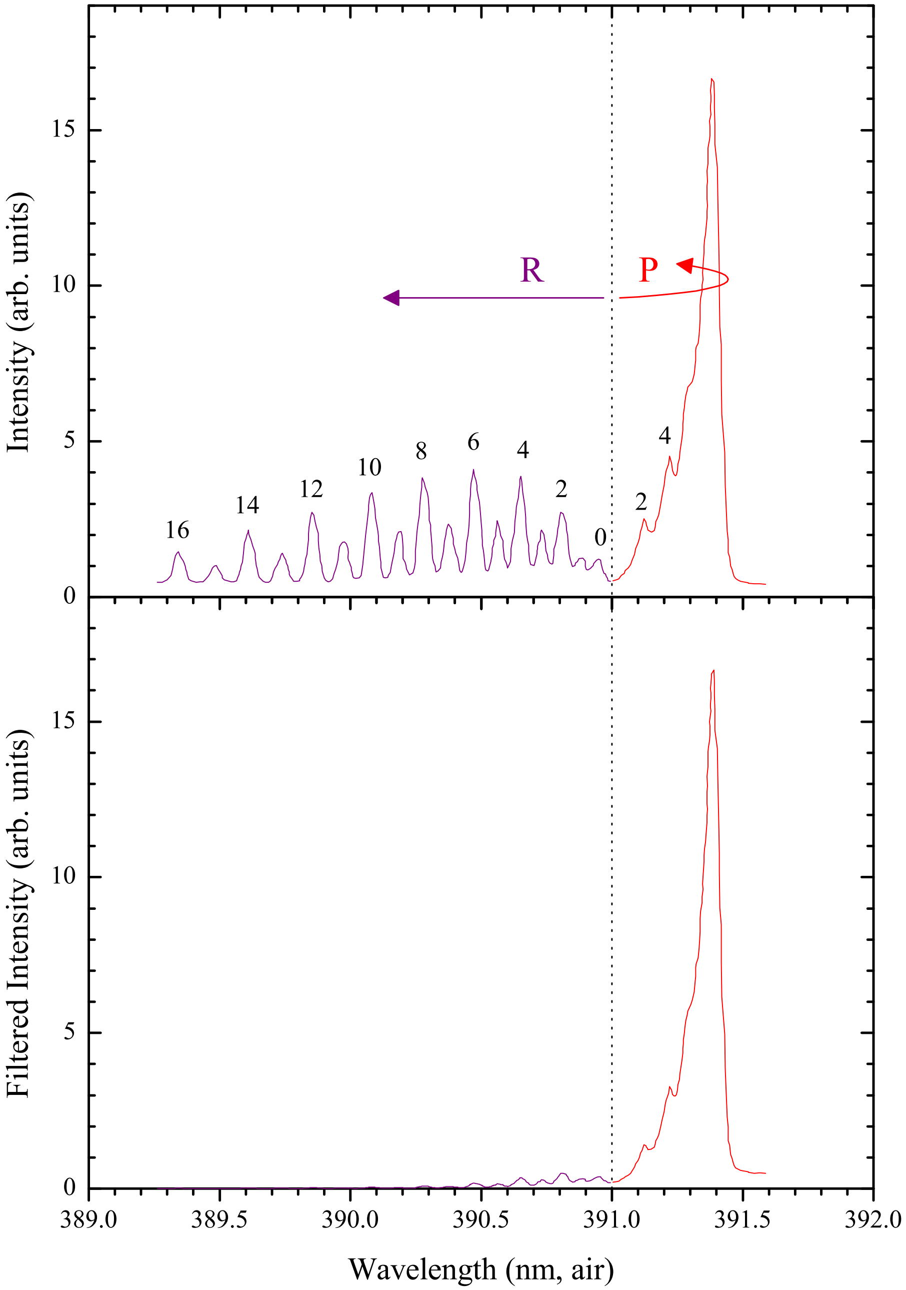

Figure 5.14: Upper figure: rotational spectrum for the 391.4 nm band taken from Ref. [104]; some final rotational states for the $P(N'')$- and $R(N'')$-branches are labeled. Lower figure: spectrum modified by the transmission of the bandpass filter used for this experiment.

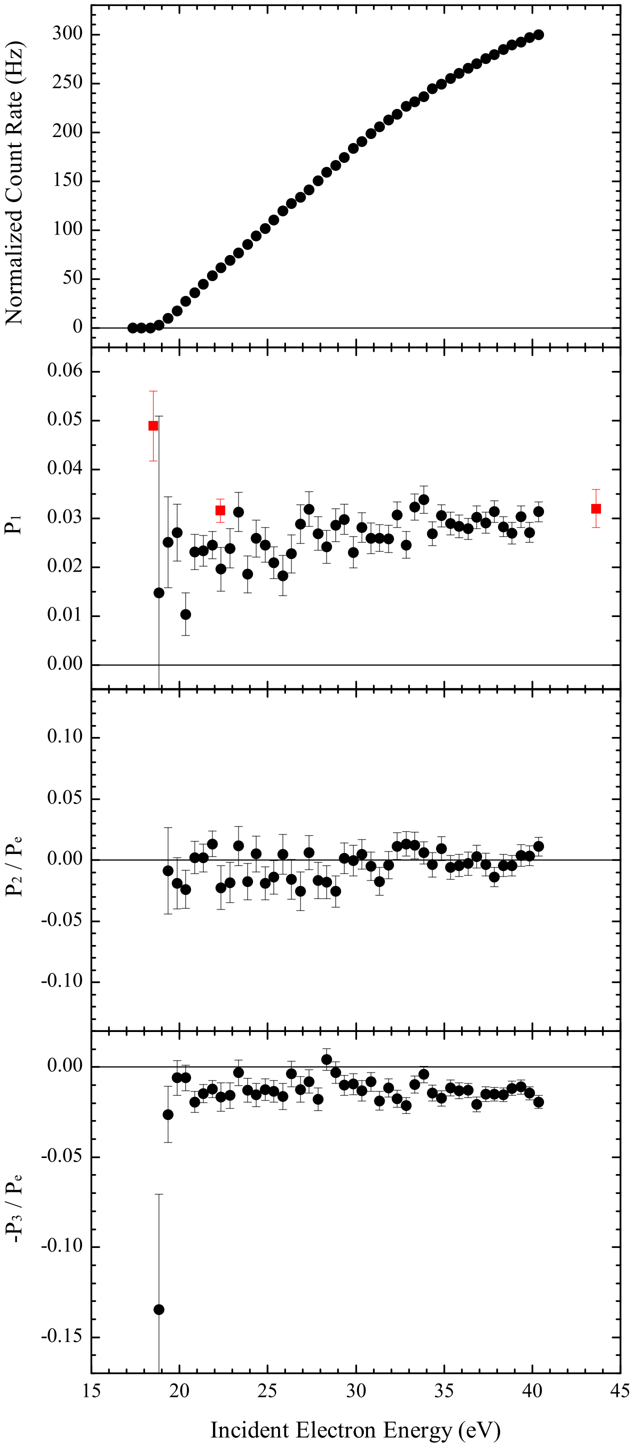

Figure 5.15: Stokes parameters for the $N_2^+ \; B\,^2\Sigma_u^+ \rightarrow X\,^2\Sigma_g^+$ (0 − 0) 391.4 nm first negative system (acquired at 0.3 mTorr). Data of this work is represented by circles (1σ errors); linear polarization data of Ref. [105] is shown in squares (errors represent 98% confidence level). Threshold is at 18.75 eV [106].

value of P_1 should be. For production of the $B\,^2\Sigma$ state, preferential excitation of $M_J = \pm\frac{1}{2}$ levels is expected [108]. This would yield positive P_1 values for the thermal ensemble of rotational states present in a room-temperature target, which are observed. In addition, the effects of hyperfine and fine-structure depolarization are significant [109], leading to an overall reduction in the degree of linear polarization at all energies. The measured values of P_2/P_e are consistent with zero. This is expected, as the total spin of the collision system should be a good quantum number due to the low Z of the target nuclei [17].

The non-zero value of $-P_3/P_e$ for the 391.4 nm fluorescence provides direct evidence of molecular orientation due to the coupling of $\boldsymbol{N}$ with $\boldsymbol{S}$. Fitting a constant to the data gives an energy-averaged value of $-0.0133(8)$, with a reduced $\chi^2 = 1.04$. However, the observed values are relatively small when compared to the circular polarizations detected for atomic and even molecular H_2 triplet-state fluorescence. There are several reasons that may explain the small values of circular polarization we observe. The first is related to the fact that the B state is a doublet, so electron exchange is not guaranteed, and the initial spin orientation may be diluted relative to a triplet state by an exchange-to-direct excitation cross section ratio. Another factor to consider is the relative magnitude of rotational state angular momenta in N_2 vs. H_2, as previously mentioned. For larger values of N, spin orientation is less effective at producing appreciable nuclear orbital orientation, resulting in smaller P_3 values. Room temperature rotational states in nitrogen are populated up to $N\sim 20$, while for hydrogen the maximum N is ~ 3 (see Fig. 5.11). Thus the doublet state spin momentum of $\frac{1}{2}\hbar$ is small compared with the rotational angular momentum of $\sqrt{N(N+1)}\hbar$. In fact, this ratio ($\sim\frac{1}{40}$ for maximum N) is roughly an order of magnitude less than that for triplet-state H_2 ($\sim\frac{1}{3}$ for maximum N). This effect alone could account for the differences in the observed $-P_3/P_e$ from these two molecular species. Finally, the results are susceptible to both fine and hyperfine depolarization [88, 109]. Typical hyperfine splittings in the excited states of atomic nitrogen are of the order of 10^8 Hz [110], so molecular depolarization should occur in ∼10 ns.

This study of the Stokes parameters for the first negative system in N_2^+ confirms the idea that P-branch fluorescence should give negative values of $-P_3/P_e$. For this N_2^+ Hund's case (b) $B\,^2\Sigma_u^+(v' = 0) \rightarrow X\,^2\Sigma_g^+(v'' = 0)$ band, our interference filter isolated the P-branch fluorescence from the R-branch contribution and we measured a non-zero energy-averaged value of $-P_3/P_e = -0.0133(8)$. Furthermore, the angular momentum coupling scheme for the excited and final states closely resembles atomic LS-coupling (compare Figs. 1.1a with 1.1b on p. 7). With the substitution $N \rightarrow L$, the atomic formalism can be used to compute the threshold circular polarization (hyperfine depolarization is neglected) for the $R(N''=0)$ and $P(N''=2)$ transitions excited from the $N=0$ molecular ground state. This results in $-P_3/P_e = 0.29$ for the $R(0)$ line and $-P_3/P_e = -0.16$ for the $P(2)$ transition (see Appendix B, Sec. B.5), which again confirms that the circular polarizations from P- and R-branches have opposite signs.

5.2.3 Stokes parameters for the N_2 first positive system

Stokes parameter measurements are presented for some rotationally isolated lines in the first positive band of N_2,

$$\begin{aligned} e + N_2\,X\,^1\Sigma_g^+(v=0) &\rightarrow B\,^3\Pi_g(v'=7) + e \\ &\rightarrow A\,^3\Sigma_u^+(v''=3) + e + \gamma(\sim 601.4\,\text{nm}). \end{aligned} \tag{5.5}$$

This data was taken using a 601.30 ± 0.16 nm FWHM bandpass filter. To determine which rotational transitions this filter transmitted, the spectra was computed using the molecular parameters from Ref. [111] and the energy levels of the $^3\Pi$ and $^3\Sigma$ levels given in Ref. [23]. Following historical convention, Hund's case (b) notation was used for notating the 27 different branches [112]. Seven branches which are transmitted by the bandpass filter are plotted in Fig. 5.16. Of these, three appear to provide the dominant contribution. These three are the P_{11}, P_{12}, and P_{13} branches. The P_{11} main branch is bright for large rotational quantum numbers [113, 114]. (Other lines from neighboring bands should not be completely discounted, however [115].) The subscript notation refers to the upper and lower state multiplets. Note that N, O, S, and T rotational branches are allowed (and correspond to $\Delta K = -3, -2, 2$, and 3, respectively) in addition the usual P, Q, and R lines. This is due to the inaccuracy of Hund's case (b) for low J values of the excited $B\,^3\Pi_g$ state (which is better described by Hund's case (a) [23]). This means that K is not strictly a good quantum number, but the strict selection rule $\Delta J = 0, \pm 1$ still applies [112].

The measured Stokes parameters are plotted in Figure 5.17. The second threshold near 11 eV in the intensity data is known to be due to cascade contribution from the second positive system [115]. The linear polarization P_1 is small and the P_2/P_e data is consistent with zero. Due to the dominant P-branch character of the fluorescence, negative values of $-P_3/P_e$ are expected, as discussed in the previous sections. Figure 5.17 shows that negative values were actually measured. The observed $-P_3/P_e$ values are ~ -0.05, with a peak value of -0.07 occurring near 10 eV. These circular polarizations represent the largest values measured for N_2 excited by spin-polarized electrons.

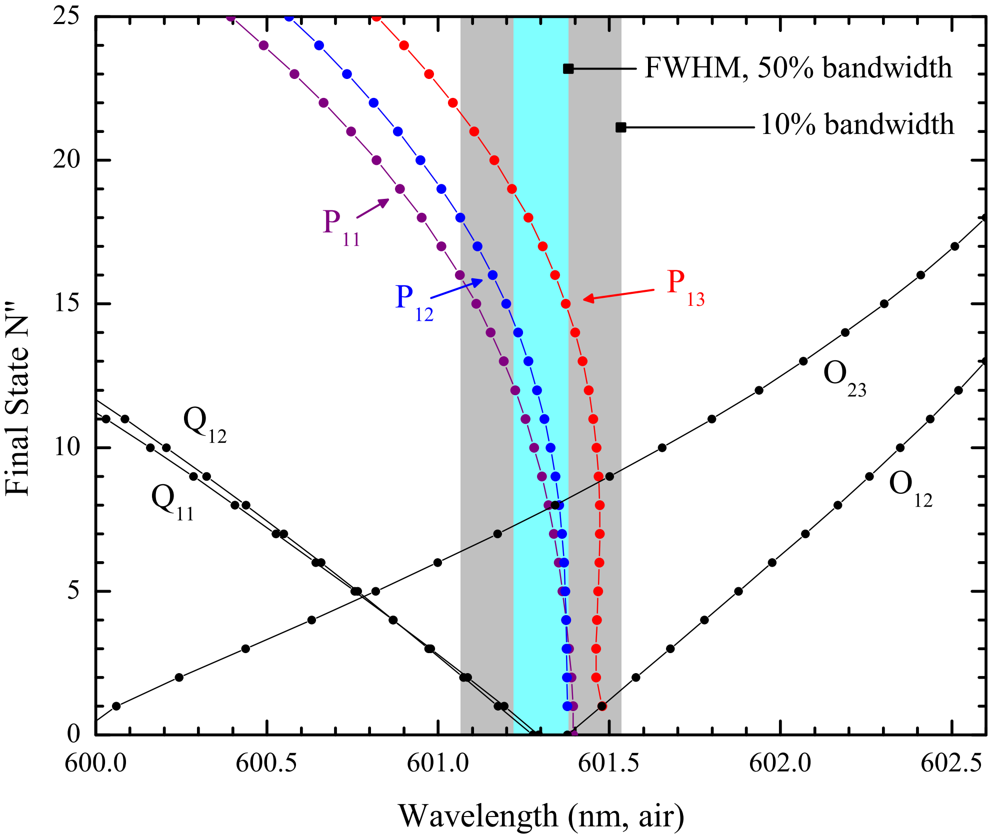

Figure 5.16: Calculated wavelengths for branches in the N_2 $(7-3)$ 601.4 nm first positive system using spectral constants from [111] with the $^3\Pi$ and $^3\Sigma$ energy level expressions given in Ref. [23]. The observed overlap with the interference filter bandpass indicates that the fluorescence is dominated by *P*-branch emission.

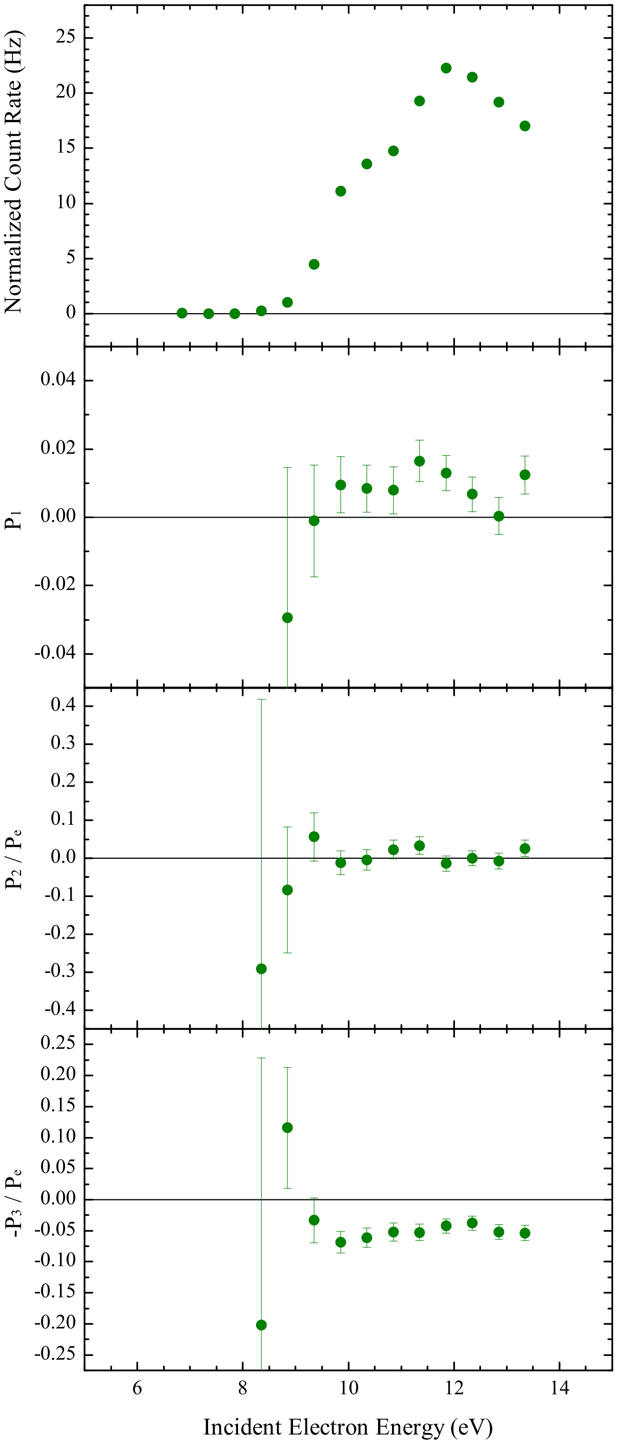

Figure 5.17: Stokes parameters for the N_2 $B\,^3\Pi_g \rightarrow A\,^3\Sigma_u^+$ $(7-3)$ 601.4 nm first positive system. Data was acquired at a pressure of 0.5 mTorr.

Chapter 6. Summary

In this dissertation measurements of the Stokes parameters are presented for atomic, dissociated atomic, and molecular transitions excited by spin-polarized electron impact. Since the targets (He, H_2, D_2, and N_2) were investigated using spin-polarized electrons, the observed fluorescence polarizations contain information about the angular momentum coupling dynamics at work in the excited systems. Significant new improvements to the apparatus made during the course of this work are described in Chap. 2.

For the helium negative-ion resonances discussed in Chap. 3, the failure to see discernable resonance effects in P_2 indicates that even though the lifetime of these resonances is significant (∼10 fs), magnetic forces acting on the temporarily-captured electron are not observable. Resonant structures in the values of P_1 and P_3 were observed due to polarization contributions from the resonant states. Further, these P_1 and P_3 polarization contributions to the detected $3\,^3D \rightarrow 2\,^3P$ transition were found to be consistent with the threshold values for direct excitation of this channel, indicating that the resonances act as cascade-free intermediate states that serve to populate the $3\,^3D$ state.

Data is presented in Chap. 4 regarding the Stokes parameters for atomic transitions resulting from the dissociation of simple diatomic molecules (H_2, D_2, and N_2). The results are compared with previous measurements where available. Currently there are no theoretical calculations to compare with the data, but these results could be of some aid if such calculations are undertaken in the future as the observed circular polarization quantifies contributions from states with different multiplicities. Contributions from singlet states yield no circular polarization, while states with higher multiplicities exhibit nonzero $-P_3/P_e$. Due to the present lack of theory describing atomic polarizations from electron induced dissociation of molecules, threshold values of P_1 and $-P_3/P_e$ were computed for the hypothetical case of atomic excitation. It was discovered that these threshold numbers represent an upper bound for the observed polarizations due to dissociation processes. Also, the measured values of $-P_3/P_e$ were found to be similar to the circular polarization calculated for atomic-threshold excitation. Thus although the net linear polarization is typically small due to the averaging over all molecular orientations, the circular polarization is not. This suggests that orientation depends only weakly on alignment for the studied systems.

Chapter 5 includes data which represents the first observation of rotationally-resolved circular polarizations for molecular transitions due to electron impact processes. The Q-branch $-P_3/P_e$ data for H_2 and D_2 provide experimental verification that the coupling of oriented electron spin to larger values of molecular angular momenta yields smaller values of orientation. In order to explain the observed null results for the circular polarization from the second positive band in N_2, we have proposed that the circular polarizations for P- and R-branch transitions exhibit $-P_3/P_e$ values of opposite sign. To verify this, experiments with partial rotational-selection were performed in the first negative and first positive bands of N_2. It was indeed discovered that the P-branch fluorescence yields negative values of $-P_3/P_e$; the H_2 and D_2 experiments show that the Q- and R-branches give positive values of $-P_3/P_e$.

It is noted here that investigations of molecules by spin-polarized electrons could aid in the identification of molecular spectra. The assignments of several molecular transitions in H_2, for example, remain ambiguous [79]. For cases where Dieke's proposed assignments include both singlet and triplet states, measurement of the circular polarization could be used to unambiguously verify which multiplicity is correct. If no circular polarization is observed, the lines must be of singlet character, while non-zero values of $-P_3/P_e$ would imply triplet character.

6.1 Future experiments

Further investigations of molecular transitions would benefit from the addition of a spectrometer to the experimental apparatus. The narrowest bandpass filters (~0.15 nm FWHM in the 600 nm range) are often still too wide when rotational isolation is desired (especially for larger molecules such as N_2). The addition of a spectrometer could increase the wavelength resolution by more than an order of magnitude when compared to bandpass filters, and could allow for measurement of rotationally-isolated lines across entire bands (see Fig. 5.14 for example). This would enable a more comprehensive quantitative study of the dependence of the Stokes parameters on rotational states. The effects of spin-uncoupling in N_2 (the shift from Hund's case (a) at low J values to Hund's case (b) and higher values) could be investigated. For such experiments it would be advisable to develop a means by which to alter the target cell temperature, so that the thermal distribution of ground state rotational populations could be manipulated to maximize intensities in the rotational area of interest (e.g., when measuring low rotational states the gas could be cooled and when measuring large J-values the gas could be heated). The dependence of the polarizations on the character of states should also be explored, i.e., what differences in the Stokes parameters should be expected for $\Sigma - \Sigma$, $\Pi - \Sigma$, $\Pi - \Pi$, and even $\Delta - \Pi$ transitions?

If future experimental work is to be performed concerning spin-polarized excitation of molecules, a descriptive theory is desirable. The theoretical formalism of Blum and Jakubowicz needs to be extended to account for spin-polarized excitation [88]. Also, the theory for Stokes parameters from systems described by Hund's case (a) remains to be developed.

Appendix A. Data Analysis Software

The following code was written for the GNU Fortran g77 (gcc version 3.4.6) compiler.

```
!======================================================================!
!     Stokes program                                                   !
!======================================================================!
      program main
      implicit none
      integer*4 nx,counter,i,j,k,m,ii,jj,bad,thresh,limit
      integer*4 energies,angles,rotations,spin
      integer*4 recu,sorts,switch,bsw,ibsw

      real*8 ki,d,pe,pi,cpi,dE,avg,stddev,stddevm,avg1,stddev1
      real*8 shift,b_offset,a0,a0e,b0,b0e,b0_a0,b0_a0e,a0_p1,a0_p1e
      real*8 avg_c,avg_p,avgc,avgp,pslope,poffset,bg
      real*8 ti,tie,tp1,tp1e,tp2,tp2e,tp3,tp3e,tempor

      real*8 ENERGY,ANGLE,SANGLE,COUNTS,DWELL,CCUR,TCUR,OCUR
      real*8 ICUR,SIG,OIG,TCG,CR,CUP,CRA,TCGA,CUPA
      real*8 ARRAY,TEMP,TEMPE
      real*8 SI,SIE,SP1,SP1E,SP2,SP2E,NSP2,NSP2E,SP3,SP3E
      real*8 SII,SIIE,SP11,SP11E,SP22,SP22E,SP33,SP33E
      real*8 BACK,DUMMY,DUMMYY,DUMMY1,DUMMYY1
      real*8 ARR,ARRE

      parameter (nx=100000)
      dimension ENERGY(nx),ANGLE(nx),SANGLE(nx),COUNTS(nx),DWELL(nx)
      dimension CCUR(nx),TCUR(nx),OCUR(nx),ICUR(nx),SIG(nx),OIG(nx)
      dimension TCG(nx),CR(nx),CUP(nx)
      dimension CRA(121,8,401,2),TCGA(121,8,401,2),CUPA(121,8,401,2)
      dimension ARRAY(121,8,401,2),TEMP(8),TEMPE(8)
      dimension SI(121),SIE(121),SP1(121),SP1E(121),SP2(121),SP2E(121)
      dimension NSP2(121),NSP2E(121),SP3(121),SP3E(121)
      dimension SII(121,2),SIIE(121,2),SP11(121,2),SP11E(121,2)
      dimension SP22(121,2),SP22E(121,2),SP33(121,2),SP33E(121,2)
      dimension BACK(8),DUMMY(nx),DUMMYY(nx),DUMMY1(nx),DUMMYY1(nx)
      dimension ARR(121,8,2),ARRE(121,8,2)

!=====define parameters================================================!
      ki=0.9998d0 !value of k for linear polarizer
      d=95.92d0   !value of delta in degrees for retarder
      pe=0.25d0   !value of electron spin polarization, positive

      pslope=0.709d0*214d0 !true pressure = pslope*(OIG-poffset)
      poffset=1.d-8

      b_offset=90.d0 !0 if fast axis is aligned to e-beam, 90 for slow

```

```
      shift=3.65d0 !true energy is lab-shift
      recu=0 !Apply Chauvenet's criterion successively? NO(0), YES(1)
      pi  = 4.d0*atan(1.d0)
      cpi = pi/180.d0
      spin=2
      angles=8
      write(*,*)'Scanned energy first (0), or rotated qwp first (1)?'
      read*,sorts
      open(unit=10,file='percentbad')

!=====load the data==================================================!
      call input(ENERGY,ANGLE,SANGLE,COUNTS,DWELL,CCUR,TCUR,OCUR,
     &ICUR,SIG,OIG,TCG,counter)

      if(sorts.eq.0)then

      dE=abs(ENERGY(2)-ENERGY(1))
      do i=1,counter
      if(ENERGY(i+1).gt.ENERGY(1))then
      continue
      else
      goto 11
      endif
      enddo!i
 11   energies=i

      elseif(sorts.eq.1)then

      dE=abs(ENERGY(2*angles+1)-ENERGY(1))
      tempor=0
      do i=1,counter
      if(ENERGY(i).ge.tempor)then
      tempor=ENERGY(i)
      else
      goto 12
      endif
      enddo!i
 12   energies=((tempor-ENERGY(1))/dE)+1

      else
      write(*,*)'Unexpected value of sorts...stop.'
      stop
      endif

      rotations=counter/(2*angles*energies)
      write(*,*)energies,' energies,',rotations,' rotations, and',
     &counter,' lines found in input.'
      if(2*angles*energies*rotations.ne.counter)then
      write(*,*)'Input file is not of proper length...stop.'
      stop
      endif
```

```
!=====compute pressure, count rate, and current========================!
      avg_p    = 0.d0
      avg_c    = 0.d0
      do i=1,counter
      CR(i)=COUNTS(i)/DWELL(i)
      TCG(i)=pslope*(OIG(i)-poffset)
      CUP(i)=-1.d0*(OCUR(i)+ICUR(i))
      avg_p=avg_p+TCG(i)/counter
      avg_c=avg_c+CUP(i)/counter
      enddo!i
      write(*,*)’avg pressure :’,avg_p
      write(*,*)’avg current  :’,avg_c

!=====resort the data into some arrays=================================!
      if(sorts.eq.0)then
      call sore(CR,TCG,CUP,energies,angles,rotations,spin,CRA,TCGA,CUPA)
      elseif(sorts.eq.1)then
      call sorr(CR,TCG,CUP,energies,angles,rotations,spin,CRA,TCGA,CUPA)
      endif

!=====just plot the average count rates================================!
      open(unit=11,file=’avgcr’)
      do i=1,energies
      ii=0
      do j=1,angles
      do m=1,spin
      do k=1,rotations
      ii=ii+1
      DUMMY(ii)=CRA(i,j,k,m)
      enddo!k
      enddo!m
      enddo!j
      call chauvenet(DUMMY,ii,recu,bad,avg,stddev,stddevm)
      write(10,*)100.d0*bad/ii
      write(11,*)ENERGY(1)+(i-1)*dE-shift,avg,stddevm
      enddo!i
      close(11)
      write(*,*)’Please look in avgcr file and decide where thresh is.’
      write(*,*)’Threshold is? (Enter integer point number > 1)’
      read*,thresh
      write(*,*)’Limit is? (#pts above thresh to exclude for a0,b0 fit)’
      read*,limit

!=====background fork==================================================!
      write(*,*)’Manually enter background? (0)NO, (1)YES’
      read*,bsw
      if(bsw.eq.0)then
      goto 13
      elseif(bsw.eq.1)then
      write(*,*)’Background count rate is? (Hz)’
      read*,bg
```

```
      goto 17
      else
      write(*,*)'Unexpected value of bsw...stop.'
      stop
      endif

!=====fit and subtract backgrounds=====================================!
 13   ii=0
      avgp=0.d0
      avgc=0.d0
      do j=1,angles
      do m=1,spin
      do k=1,rotations
      ii=ii+1
      DUMMY(ii)=TCGA(thresh,j,k,m)
      DUMMYY(ii)=CUPA(thresh,j,k,m)
      enddo!k
      enddo!m
      enddo!j
      call chauvenet(DUMMY,ii,recu,bad,avg,stddev,stddevm)
      write(*,*)'Threshold pressure :',avg,stddevm,100.d0*bad/ii
      avgp=avg
      call chauvenet(DUMMYY,ii,recu,bad,avg,stddev,stddevm)
      write(*,*)'Threshold current  :',avg,stddevm,100.d0*bad/ii
      avgc=avg

      write(*,*)'Fit retarder orientions individually? (0)No, (1)Yes'
      read*,ibsw
      if(ibsw.eq.0)then
      goto 14
      elseif(ibsw.eq.1)then
      goto 15
      else
      write(*,*)'Unexpected value of ibsw...stop.'
      stop
      endif

 14   ii=0
      do j=1,angles
      do m=1,spin
      do k=1,rotations
      do i=1,thresh-1
      ii=ii+1
      DUMMY(ii)=CRA(i,j,k,m)
      enddo!i
      enddo!k
      enddo!m
      enddo!j
      call chauvenet(DUMMY,ii,recu,bad,avg,stddev,stddevm)
      write(10,*)100.d0*bad/ii
      do j=1,angles
```

```
     BACK(j)=avg
     enddo!j
     write(*,*)'Background rate is',avg,stddevm,100.d0*bad/ii
     goto 16

15   open(unit=12,file='backgrounds')
     do j=1,angles
     ii=0
     do m=1,spin
     do k=1,rotations
     do i=1,thresh-1
     ii=ii+1
     DUMMY(ii)=CRA(i,j,k,m)
     enddo!i
     enddo!k
     enddo!m
     call chauvenet(DUMMY,ii,recu,bad,avg,stddev,stddevm)
     write(10,*)100.d0*bad/ii
     BACK(j)=avg
     write(*,*)'Background rate',j,' is',avg,stddevm,100.d0*bad/ii
     write(12,*)j,avg,stddevm
     enddo!j
     close(12)
     goto 16

16   do i=1,energies
     do j=1,angles
     do k=1,rotations
     do m=1,spin
     CRA(i,j,k,m)=CRA(i,j,k,m)-BACK(j)
     enddo!m
     enddo!k
     enddo!j
     enddo!i

     do j=1,angles
     do k=1,rotations
     do m=1,spin
     do i=1,thresh-1
     ARRAY(i,j,k,m)=CRA(i,j,k,m)
     enddo!i
     do i=thresh,energies
     ARRAY(i,j,k,m)=CRA(i,j,k,m)*(avgc*avgp)
    &/(TCGA(i,j,k,m)*CUPA(i,j,k,m))
     enddo!i
     enddo!m
     enddo!k
     enddo!j
```

```
      do i=1,energies
      do j=1,angles
      do m=1,spin
      do k=1,rotations
      DUMMY(k)=ARRAY(i,j,k,m)
      enddo!k
      call chauvenet(DUMMY,rotations,recu,bad,avg,stddev,stddevm)
      write(10,*)100.d0*bad/rotations
      ARR(i,j,m)=avg
      ARRE(i,j,m)=stddevm
      enddo!m
      enddo!j
      enddo!i
      goto 18

!=====subtract background manually=====================================!
 17   do i=1,energies
      do j=1,angles
      do m=1,spin
      do k=1,rotations
      DUMMY(k)=((CRA(i,j,k,m)-bg)*(avg_c*avg_p))
     &/(TCGA(i,j,k,m)*CUPA(i,j,k,m))
      enddo!k
      call chauvenet(DUMMY,rotations,recu,bad,avg,stddev,stddevm)
      write(10,*)100.d0*bad/rotations
      ARR(i,j,m)=avg
      ARRE(i,j,m)=stddevm
      enddo!m
      enddo!j
      enddo!i
      goto 18

!=====find a0 and b0 fork==============================================!
 18   write(*,*)'Manually input a0 and b0? (0 for NO, 1 for YES)'
      read*,switch
      if(switch.eq.0)then
      goto 19
      elseif(switch.eq.1)then
      write(*,*)'a0 is: (degrees)'
      read*,a0
      write(*,*)'b0 is: (degrees; b_offset will be added to input b0)'
      read*,b0
      b0=b0+b_offset
      goto 70
      else
      write(*,*)'Unexpected value of switch...stop.'
      stop
      endif
```

```
!=====find a0 and b0===================================================!
 19   open(unit=13,file='checkb0_p3')
      open(unit=14,file='checka0_p1')
      open(unit=15,file='checka0_p2')

!=====get b0_a0 (which includes b_offset)
      do i=1,energies
      DUMMY(i)=0.d0
      enddo!i
      do jj=1,181
      a0=0.d0
      b0=b_offset+((jj-1)-90.d0)/4.d0

      do m=1,spin
      do i=1,energies
      do j=1,angles
      TEMP(j)=ARR(i,j,m)
      TEMPE(j)=ARRE(i,j,m)
      enddo!j
      call stokes(TEMP,TEMPE,a0,b0,ki,d,ti,tie,tp1,tp1e,tp2,tp2e,tp3,
     &tp3e)
      SP33(i,m)=tp3
      SP33E(i,m)=tp3e
      enddo!i
      enddo!m
      do i=1,energies
      SP3(i)=(SP33(i,1)/SP33E(i,1)**2-SP33(i,2)/SP33E(i,2)**2)/
     &(1.d0/SP33E(i,1)**2+1.d0/SP33E(i,2)**2)
      SP3E(i)=sqrt(1.d0/(1.d0/SP33E(i,1)**2+1.d0/SP33E(i,2)**2))
      enddo!i

      do i=thresh+limit,energies
      write(13,*)b0,SP3(i),SP3E(i)
      if(abs(SP3(i)).gt.DUMMY(i))then
      DUMMY(i)=abs(SP3(i))
      DUMMYY(i)=b0
      endif
      enddo!i
      enddo!jj

      avg=0.d0
      stddev=0.d0
      do i=thresh+limit,energies
      avg=avg+DUMMYY(i)
      enddo!i
      b0_a0=avg/(energies-(thresh+limit)+1)
      do i=thresh+limit,energies
      stddev=stddev+(DUMMYY(i)-b0_a0)**2
      enddo!i
      stddev=sqrt(stddev/(energies-(thresh+limit)))
      b0_a0e=stddev/sqrt(1.d0*(energies-(thresh+limit)+1))
```

```
!=====get a0 (then b0 = a0 + b0_a0)
      do i=1,energies
      DUMMY1(i)=0.d0
      DUMMY(i)=1000.d0
      enddo!i
      do ii=1,181
      a0=((ii-1)-90.d0)/4.d0
      b0=a0+b0_a0

      do m=1,spin
      do i=1,energies
      do j=1,angles
      TEMP(j)=ARR(i,j,m)
      TEMPE(j)=ARRE(i,j,m)
      enddo!j
      call stokes(TEMP,TEMPE,a0,b0,ki,d,ti,tie,tp1,tp1e,tp2,tp2e,tp3,
     &tp3e)
      SP11(i,m)=tp1
      SP11E(i,m)=tp1e
      SP22(i,m)=tp2
      SP22E(i,m)=tp2e
      enddo!i
      enddo!m
      do i=1,energies
      SP1(i)=(SP11(i,1)/SP11E(i,1)**2+SP11(i,2)/SP11E(i,2)**2)/
     &(1.d0/SP11E(i,1)**2+1.d0/SP11E(i,2)**2)
      SP1E(i)=sqrt(1.d0/(1.d0/SP11E(i,1)**2+1.d0/SP11E(i,2)**2))
      SP2(i)=(SP22(i,1)/SP22E(i,1)**2+SP22(i,2)/SP22E(i,2)**2)/
     &(1.d0/SP22E(i,1)**2+1.d0/SP22E(i,2)**2)
      SP2E(i)=sqrt(1.d0/(1.d0/SP22E(i,1)**2+1.d0/SP22E(i,2)**2))
      enddo!i

      do i=thresh+limit,energies
      write(14,*)a0,SP1(i),SP1E(i)
      write(15,*)a0,SP2(i),SP2E(i)

      if(abs(SP1(i)).gt.DUMMY1(i))then
      DUMMY1(i)=abs(SP1(i))
      DUMMYY1(i)=a0
      endif
      if(abs(SP2(i)).lt.DUMMY(i))then
      DUMMY(i)=abs(SP2(i))
      DUMMYY(i)=a0
      endif

      enddo!i

      enddo!ii
      avg1=0.d0
      avg=0.d0
      stddev1=0.d0
```

```
      stddev=0.d0
      do i=thresh+limit,energies
      avg1=avg1+DUMMYY1(i)
      avg=avg+DUMMYY(i)
      enddo!i
      a0_p1=avg1/(energies-(thresh+limit)+1)
      a0=avg/(energies-(thresh+limit)+1)
      do i=thresh+limit,energies
      stddev1=stddev1+(DUMMYY1(i)-a0_p1)**2
      stddev=stddev+(DUMMYY(i)-a0)**2
      enddo!i
      stddev1=sqrt(stddev1/(energies-(thresh+limit)))
      stddev=sqrt(stddev/(energies-(thresh+limit)))

      a0_p1e=stddev1/sqrt(1.d0*(energies-(thresh+limit)+1))
      a0e=stddev/sqrt(1.d0*(energies-(thresh+limit)+1))
      b0=a0+b0_a0
      b0e=b0_a0e
      write(*,*)'avg a0_p1',a0_p1,a0_p1e
      write(*,*)'avg a0_p2',a0,a0e
      write(*,*)'avg b0_p3',b0,b0e
      close(13)
      close(14)
      close(15)

!=====calculate stokes parameters=====================================!
 70   do m=1,spin
      do i=1,energies
      do j=1,angles
      TEMP(j)=ARR(i,j,m)
      TEMPE(j)=ARRE(i,j,m)
      enddo!j
      call stokes(TEMP,TEMPE,a0,b0,ki,d,ti,tie,tp1,tp1e,tp2,tp2e,tp3,
     &tp3e)
      SII(i,m)=ti
      SIIE(i,m)=tie
      SP11(i,m)=tp1
      SP11E(i,m)=tp1e
      SP22(i,m)=tp2
      SP22E(i,m)=tp2e
      SP33(i,m)=tp3
      SP33E(i,m)=tp3e
      enddo!i
      enddo!m
      do i=1,energies
      SI(i)=(SII(i,1)/SIIE(i,1)**2+SII(i,2)/SIIE(i,2)**2)/
     &(1.d0/SIIE(i,1)**2+1.d0/SIIE(i,2)**2)
      SIE(i)=sqrt(1.d0/(1.d0/SIIE(i,1)**2+1.d0/SIIE(i,2)**2))
      SP1(i)=(SP11(i,1)/SP11E(i,1)**2+SP11(i,2)/SP11E(i,2)**2)/
     &(1.d0/SP11E(i,1)**2+1.d0/SP11E(i,2)**2)
      SP1E(i)=sqrt(1.d0/(1.d0/SP11E(i,1)**2+1.d0/SP11E(i,2)**2))
```

```
      SP2(i)=(SP22(i,1)/SP22E(i,1)**2+SP22(i,2)/SP22E(i,2)**2)/
     &(1.d0/SP22E(i,1)**2+1.d0/SP22E(i,2)**2)
      SP2E(i)=sqrt(1.d0/(1.d0/SP22E(i,1)**2+1.d0/SP22E(i,2)**2))
      NSP2(i)=(SP22(i,1)/SP22E(i,1)**2-SP22(i,2)/SP22E(i,2)**2)/
     &(1.d0/SP22E(i,1)**2+1.d0/SP22E(i,2)**2)/pe
      NSP2E(i)=sqrt(1.d0/(1.d0/SP22E(i,1)**2+1.d0/SP22E(i,2)**2))/pe
      SP3(i)=(SP33(i,1)/SP33E(i,1)**2-SP33(i,2)/SP33E(i,2)**2)/
     &(1.d0/SP33E(i,1)**2+1.d0/SP33E(i,2)**2)/pe
      SP3E(i)=sqrt(1.d0/(1.d0/SP33E(i,1)**2+1.d0/SP33E(i,2)**2))/pe
      enddo!i

!=====write the data and shift the energies=============================!
      open(unit=20,file='dataup')
      m=1
      do i=1,energies
      write(20,80)ENERGY(1)+(i-1)*dE-shift,SII(i,m),SIIE(i,m),SP11(i,m),
     &SP11E(i,m),SP22(i,m),SP22E(i,m),SP33(i,m),SP33E(i,m)
 80   format(f7.3,1x,e12.6,1x,e12.6,1x,e12.6,1x,e12.6,1x,e12.6,1x,e12.6,
     &1x,e12.6,1x,e12.6)
      enddo!i
      close(20)

      open(unit=21,file='datadown')
      m=2
      do i=1,energies
      write(21,81)ENERGY(1)+(i-1)*dE-shift,SII(i,m),SIIE(i,m),SP11(i,m),
     &SP11E(i,m),SP22(i,m),SP22E(i,m),SP33(i,m),SP33E(i,m)
 81   format(f7.3,1x,e12.6,1x,e12.6,1x,e12.6,1x,e12.6,1x,e12.6,1x,e12.6,
     &1x,e12.6,1x,e12.6)
      enddo!i
      close(21)

      open(unit=22,file='data')
      do i=1,energies
      write(22,82)ENERGY(1)+(i-1)*dE-shift,SI(i),SIE(i),SP1(i),SP1E(i),
     &SP2(i),SP2E(i),NSP2(i),NSP2E(i),SP3(i),SP3E(i)
 82   format(f7.3,1x,e12.6,1x,e12.6,1x,e12.6,1x,e12.6,1x,e12.6,1x,e12.6,
     &1x,e12.6,1x,e12.6,1x,e12.6,1x,e12.6,1x,e12.6,1x,e12.6)
      enddo!i
      close(22)

      close(10)
      stop
      end!main

!=======================================================================!
      subroutine input(A1,A2,A3,A4,A5,A6,A7,A8,A9,A10,A11,A12,counter)
      implicit none
      character*64 infname
      integer*4 nx,counter,done,i
      real*8 A1,A2,A3,A4,A5,A6,A7,A8,A9,A10,A11,A12
```

```
      parameter (nx=100000)
      dimension A1(nx),A2(nx),A3(nx),A4(nx),A5(nx),A6(nx),A7(nx),
     &A8(nx),A9(nx),A10(nx),A11(nx),A12(nx)

      open(unit=8,file='input')
      read(8,*)infname
      close(8)

      open(unit=9,file=infname)
      read(9,*)!skipping a header line
      read(9,*)!skipping a header line
      counter=0
      do i=1,nx
      read(9,*,iostat=done)A1(i),A2(i),A3(i),A4(i),A5(i),A6(i),
     &A7(i),A8(i),A9(i),A10(i),A11(i),A12(i)
      if(done.ne.0)goto 100
      counter=counter+1
      enddo!i
      if(counter.eq.nx)then
      write(*,*)'error in input subroutine, arrays not long enough!'
      stop
      endif
 100  close(9)
      return
      end!input

!======================================================================!
      subroutine sore(A1,A2,A3,energies,angles,rotations,spin,A4,A5,A6)
      implicit none!this is for data taken by scanning E first
      integer*4 i,j,k,kk,m,energies,rotations,angles,spin,arg
      real*8 A1,A2,A3,A4,A5,A6
      dimension A1(100000),A2(100000),A3(100000)
      dimension A4(121,8,401,2),A5(121,8,401,2),A6(121,8,401,2)
      do i=1,energies
      do j=1,angles
      do k=1,rotations/spin
      do kk=1,spin
      do m=1,spin
      arg=i+(m-1)*2*angles*energies+(j-1)*energies+(kk-1)
     &*angles*energies+(k-1)*4*angles*energies
      A4(i,j,1+2*(k-1)+(kk-1),m)=A1(arg)
      A5(i,j,1+2*(k-1)+(kk-1),m)=A2(arg)
      A6(i,j,1+2*(k-1)+(kk-1),m)=A3(arg)
      enddo!m
      enddo!kk
      enddo!k
      enddo!j
      enddo!i
      return
      end!sore
```

```
!======================================================================!
      subroutine sorr(A1,A2,A3,energies,angles,rotations,spin,A4,A5,A6)
      implicit none!this is for data taken by rotating the QWP first
      integer*4 i,j,k,kk,m,energies,rotations,angles,spin,arg
      real*8 A1,A2,A3,A4,A5,A6
      dimension A1(100000),A2(100000),A3(100000)
      dimension A4(121,8,401,2),A5(121,8,401,2),A6(121,8,401,2)
      do j=1,angles
      do kk=1,spin
      do i=1,energies
      do m=1,spin
      do k=1,rotations/spin
      arg=j+(i-1)*2*angles+(kk-1)*angles
     &+(k-1)*4*angles*energies+(m-1)*energies*angles*2
      A4(i,j,1+2*(k-1)+(kk-1),m)=A1(arg)
      A5(i,j,1+2*(k-1)+(kk-1),m)=A2(arg)
      A6(i,j,1+2*(k-1)+(kk-1),m)=A3(arg)
      enddo!k
      enddo!m
      enddo!i
      enddo!kk
      enddo!j
      return
      end!sorr

!======================================================================!
      subroutine chauvenet(A1,length,recu,bad,avg,stddev,stddevm)
      implicit none
      integer*4 i,length,bad,dumi,recu
      real*8 A1,A2,avg,stddev,stddevm,cha,flag,dum
      dimension A1(100000),A2(100000)
      flag = -123456789.d0
      cha  = 0.5d0
      do i=1,length
      A2(i)=A1(i)
      enddo!i
      if(recu.eq.0)then
      goto 410
      elseif(recu.eq.1)then
      goto 420
      else
      write(*,*)'unexpected value of recu...stop'
      stop
      endif
 410  bad=0
      avg=0.d0
      stddev=0.d0
      do i=1,length
      avg=avg+A2(i)
      enddo!i
      avg=avg/length
```

```
      do i=1,length
      stddev=stddev+(A2(i)-avg)**2
      enddo!i
      stddev=sqrt(stddev/(length-1))
      do i=1,length
      if(length*erfc(abs(A2(i)-avg)/(sqrt(2.d0)*stddev)).lt.cha)then
      A2(i)=flag
      bad=bad+1
      endif
      enddo!i
      avg=0.d0
      stddev=0.d0
      do i=1,length
      if(A2(i).ne.flag)then
      avg=avg+A2(i)
      endif
      enddo!i
      avg=avg/(length-bad)
      do i=1,length
      if(A2(i).ne.flag)then
      stddev=stddev+(A2(i)-avg)**2
      endif
      enddo!i
      stddev=sqrt(stddev/(length-bad-1))
      stddevm=stddev/sqrt(1.d0*(length-bad))
      goto 430
420   bad=0
421   avg=0.d0
      stddev=0.d0
      do i=1,length
      if(A2(i).ne.flag)then
      avg=avg+A2(i)
      endif
      enddo!i
      avg=avg/(length-bad)
      do i=1,length
      if(A2(i).ne.flag)then
      stddev=stddev+(A2(i)-avg)**2
      endif
      enddo!i
      stddev=sqrt(stddev/(length-bad-1))
      dum=0.d0
      do i=1,length
      if(A2(i).ne.flag)then
      if(abs(A2(i)-avg).gt.dum)then
      dum=abs(A2(i)-avg)
      dumi=i
      endif
      endif
      enddo!i

```

```
      if((length-bad)*erfc(abs(A2(dumi)-avg)/(sqrt(2.d0)*stddev)).lt.
     &cha)then
      bad=bad+1
      A2(dumi)=flag
      goto 421
      else
      goto 422
      endif
 422  stddevm=stddev/sqrt(1.d0*(length-bad))
      goto 430
 430  return
      end!chauvenet

!=========================================================================!
      subroutine stokes(TEMP,TEMPE,a0,b0,ki,d,ti,tie,tp1,tp1e,tp2,tp2e,
     &tp3,tp3e)
      implicit none
      integer*4 i,j,k
      real*8 TEMP,TEMPE,a0,b0,ki,d,ti,tie,tp1,tp1e,tp2,tp2e,tp3,tp3e
      real*8 tp4,tp4e,pi,cpi,f0,f1,f2,f3,f4,f5,T,TE,TIA,TP1A,TP2A,TP3A
      real*8 sumi,sum1,sum2,sum3
      dimension TEMP(8),TEMPE(8),T(8),TE(8)
      dimension TIA(8,2),TP1A(8,2),TP2A(8,2),TP3A(8,2)
      pi  = 4.d0*atan(1.d0)
      cpi = pi/180.d0

      do i=1,8
      T(i)=TEMP(i)
      TE(i)=TEMPE(i)
      enddo!i
      f0=0.d0
      f1=0.d0
      f2=0.d0
      f3=0.d0

      do i=1,8
      f0=f0+T(i)
      f1=f1+T(i)*cos(cpi*4.d0*(22.5d0*(i-1)+b0))
      f2=f2+T(i)*sin(cpi*4.d0*(22.5d0*(i-1)+b0))
      f3=f3+T(i)*sin(cpi*2.d0*(22.5d0*(i-1)+b0-a0))
      enddo!i
      f0=f0/8.d0
      f1=f1/2.d0
      f2=f2/2.d0
      f3=f3/4.d0

      ti=f0-0.5d0*((1.d0+cos(cpi*d))/(1.d0-cos(cpi*d)))
     &*(f1*cos(cpi*4.d0*a0)+f2*sin(cpi*4.d0*a0))
      tp1=(f1*cos(cpi*2.d0*a0)+f2*sin(cpi*2.d0*a0))/
     &(ti*ki*(1.d0-cos(cpi*d)))
      tp2=(f2*cos(cpi*2.d0*a0)-f1*sin(cpi*2.d0*a0))/
```

```
     &(ti*ki*(1.d0-cos(cpi*d)))
      tp3=-f3/(ti*ki*sin(cpi*d))
      ti=ti*(1.d0-tp1/3.d0)

!=====calculate error bars
      do k=1,2
      do j=1,8
      do i=1,8
      T(i)=TEMP(i)
      TE(i)=TEMPE(i)
      enddo!i
      T(j)=T(j)+TE(j)*((-1)**(k-1))

      f0=0.d0
      f1=0.d0
      f2=0.d0
      f3=0.d0

      do i=1,8
      f0=f0+T(i)
      f1=f1+T(i)*cos(cpi*4.d0*(22.5d0*(i-1)+b0))
      f2=f2+T(i)*sin(cpi*4.d0*(22.5d0*(i-1)+b0))
      f3=f3+T(i)*sin(cpi*2.d0*(22.5d0*(i-1)+b0-a0))
      enddo!i
      f0=f0/8.d0
      f1=f1/2.d0
      f2=f2/2.d0
      f3=f3/4.d0

      TIA(j,k)=f0-0.5d0*((1.d0+cos(cpi*d))/(1.d0-cos(cpi*d)))
     &*(f1*cos(cpi*4.d0*a0)+f2*sin(cpi*4.d0*a0))
      TP1A(j,k)=(f1*cos(cpi*2.d0*a0)+f2*sin(cpi*2.d0*a0))/
     &(TIA(j,k)*ki*(1.d0-cos(cpi*d)))
      TP2A(j,k)=(f2*cos(cpi*2.d0*a0)-f1*sin(cpi*2.d0*a0))/
     &(TIA(j,k)*ki*(1.d0-cos(cpi*d)))
      TP3A(j,k)=-f3/(TIA(j,k)*ki*sin(cpi*d))
      TIA(j,k)=TIA(j,k)*(1.d0-TP1A(j,k)/3.d0)
      enddo!j
      enddo!k

      sumi=0.d0
      sum1=0.d0
      sum2=0.d0
      sum3=0.d0

      do j=1,8
      if(abs(TIA(j,1)-ti).gt.abs(TIA(j,2)-ti))then
      sumi=sumi+(TIA(j,1)-ti)**2
      else
      sumi=sumi+(TIA(j,2)-ti)**2
      endif
```

```
      if(abs(TP1A(j,1)-tp1).gt.abs(TP1A(j,2)-tp1))then
      sum1=sum1+(TP1A(j,1)-tp1)**2
      else
      sum1=sum1+(TP1A(j,2)-tp1)**2
      endif
      if(abs(TP2A(j,1)-tp2).gt.abs(TP2A(j,2)-tp2))then
      sum2=sum2+(TP2A(j,1)-tp2)**2
      else
      sum2=sum2+(TP2A(j,2)-tp2)**2
      endif
      if(abs(TP3A(j,1)-tp3).gt.abs(TP3A(j,2)-tp3))then
      sum3=sum3+(TP3A(j,1)-tp3)**2
      else
      sum3=sum3+(TP3A(j,2)-tp3)**2
      endif
      enddo!j
      tie=sqrt(sumi)
      tp1e=sqrt(sum1)
      tp2e=sqrt(sum2)
      tp3e=sqrt(sum3)
      return
      end!stokes

!=======================================================================!
```

Appendix B. Stokes Parameters for Atoms

B.1 Polarization of atomic emission

The relation between the Stokes parameters of fluorescence and the angular momentum of atomic states excited by spin-polarized electron impact is considered here for the specific detection geometry pertaining to this work (photons emitted perpendicular to the electron beam and parallel to the electron spin polarization are collected and the scattered electrons are not detected). The Stokes parameters can be expressed in terms of the time-integrated state multipoles $\overline{\langle T(X)^{\dagger}_{KQ}\rangle}$ (where $-K \leqslant Q \leqslant K$) by

$$
\begin{aligned}
I &= C\left[\frac{2(-1)^{X+X_f}}{3\sqrt{2X+1}}\overline{\langle T(X)^{\dagger}_{00}\rangle} + \sqrt{\frac{1}{6}}\begin{Bmatrix} 1 & 1 & 2 \\ X & X & X_f \end{Bmatrix}\overline{\langle T(X)^{\dagger}_{20}\rangle}\right], \\
IP_1 &= \sqrt{\frac{3}{2}}C\begin{Bmatrix} 1 & 1 & 2 \\ X & X & X_f \end{Bmatrix}\overline{\langle T(X)^{\dagger}_{20}\rangle}, \\
IP_2 &= -2C\begin{Bmatrix} 1 & 1 & 2 \\ X & X & X_f \end{Bmatrix}\mathrm{Re}\left[\overline{\langle T(X)^{\dagger}_{21}\rangle}_{P_e}\right], \text{ and} \\
IP_3 &= -2C\begin{Bmatrix} 1 & 1 & 1 \\ X & X & X_f \end{Bmatrix}\mathrm{Im}\left[\overline{\langle T(X)^{\dagger}_{11}\rangle}_{P_e}\right]. \qquad \text{(B.1)}
\end{aligned}
$$

Equation (B.1) was obtained by evaluating Eq. 13 of Ref. [13] at the angles $\Theta = \Phi = 90°$. Here C is a constant, X and X_f are replaced with the excited and final state angular momentum (J, J_f or L, L_f depending on which states are resolved), and the P_e subscripts on the $\overline{\langle T(X)^{\dagger}_{21}\rangle}$ and $\overline{\langle T(X)^{\dagger}_{11}\rangle}$ state multipoles indicate that these are dependent on the incident electron spin polarization and thus vanish for unpolarized electron impact. The

{} brackets represent Wigner 6-j symbols.

Formulas for the state multipoles $\overline{\langle T(X)^{\dagger}_{KQ}\rangle}$ are discussed in the following sections as required for specific cases. Generally, they depend on perturbation coefficients that can account for the time-averaged effect of fine- and hyperfine-structure depolarization, as well as the product of orbital angular momentum state multipoles $\langle T(L)^{\dagger}_{KQ}\rangle$ and spin angular momentum state multipoles $\langle T(S)^{\dagger}_{KQ}\rangle$ (see Sec. B.1.1).

B.1.1 Some useful statistical tensors

This section provides a convenient collection of state multipoles used for this work, as well as a derivation of the spin tensor for quartet ($S=\frac{3}{2}$) states (as required for the nitrogen case discussed in Sec. B.4).

The state multipoles for orbital angular momentum L are given by Sec. 4.6.3 of Ref. [18] for the situation where the scattered electrons are not detected. The $\langle T(L)^{\dagger}_{KQ}\rangle$ state multipoles with index $Q\neq 0$ vanish, and

$$\begin{aligned}
\langle T(L)^{\dagger}_{00}\rangle &= \frac{\sum_M Q_M}{\sqrt{2L+1}},\\
\langle T(L)^{\dagger}_{10}\rangle &= 0, \text{ and}\\
\langle T(L)^{\dagger}_{20}\rangle &= \sqrt{\frac{5}{(2L+3)(L+1)(2L+1)(2L-1)L}}\sum_M \left[3M^2-L(L+1)\right]Q_M,
\end{aligned} \tag{B.2}$$

where $Q_M = Q_{-M}$ are the magnetic sublevel cross sections for electron orbital angular momentum.

The general spin statistical tensor is defined by Eq. (4.3.3) of Ref. [18] with $J'=J=S$:

$$\langle T(S)^{\dagger}_{KQ}\rangle = \sum_{M'M}(-1)^{S-M'}\sqrt{2K+1}\begin{pmatrix} S & S & K \\ M' & -M & -Q \end{pmatrix}\langle SM'|\rho|SM\rangle, \tag{B.3}$$

where the () brackets represent a Wigner 3-j symbol. The spin density matrix needed for Eq. (B.3) is obtained using Eq. (1.1.45) of Ref. [18],

$$\rho = \frac{1}{2S+1}(\mathbf{1} + \sum_j P_{ej}\sigma_j), \tag{B.4}$$

where the normalization factor of $2S+1$ has been introduced in the denominator so that the density matrix remains normalized ($\mathrm{tr}\,\rho = 1$) for different values of S. The identity matrix appears as $\mathbf{1}$ in Eq. (B.4), the subscript j represents the coordinates x, y, and z, P_{ej} is the electron beam spin polarization with respect to the j-axis, and σ_j are the Pauli spin matrices (of dimension $2S+1$). For this experiment, only $P_{ey} \neq 0$. For the case of $S = \frac{3}{2}$, the σ_y Pauli matrix is

$$\sigma_y = \frac{i}{3}\begin{pmatrix} 0 & -\sqrt{3} & 0 & 0 \\ \sqrt{3} & 0 & -2 & 0 \\ 0 & 2 & 0 & -\sqrt{3} \\ 0 & 0 & \sqrt{3} & 0 \end{pmatrix}. \tag{B.5}$$

The density matrix is then given by

$$\rho = \tfrac{1}{4}(\mathbf{1} + P_{ey}\sigma_y). \tag{B.6}$$

The spin tensors $\langle T(S = \frac{3}{2})^{\dagger}_{KQ}\rangle$ are obtained by inserting Eqs. (B.5) and (B.6) into (B.3), where the basis states $|SM\rangle$ are taken to be the normalized eigenvectors of the S_z operator, with $S_z = S\hbar\sigma_z$ and

$$\sigma_z = \frac{1}{3}\begin{pmatrix} 3 & 0 & 0 & 0 \\ 0 & 1 & 0 & 0 \\ 0 & 0 & -1 & 0 \\ 0 & 0 & 0 & -3 \end{pmatrix}. \tag{B.7}$$

Combining these results with existing expressions for the spin tensors $\langle T(S)^{\dagger}_{KQ}\rangle$ gives (for the case where $P_{ey} \neq 0$ and $P_{ex} = P_{ez} = 0$):

$$\begin{aligned}
&\langle T(S)^{\dagger}_{00}\rangle = \frac{1}{\sqrt{2S+1}}, \\
&\langle T(S)^{\dagger}_{10}\rangle = 0, \\
&\langle T(S=0)^{\dagger}_{11}\rangle = \langle T(S=0)^{\dagger}_{1-1}\rangle = 0, \\
&\langle T(S=\tfrac{1}{2})^{\dagger}_{11}\rangle = \langle T(S=\tfrac{1}{2})^{\dagger}_{1-1}\rangle = \frac{iP_{ey}}{2}, \\
&\langle T(S=1)^{\dagger}_{11}\rangle = \langle T(S=1)^{\dagger}_{1-1}\rangle = \frac{iP_{ey}}{3}, \\
&\langle T(S=\tfrac{3}{2})^{\dagger}_{11}\rangle = \langle T(S=\tfrac{3}{2})^{\dagger}_{1-1}\rangle = \frac{\sqrt{10}iP_{ey}}{12}, \text{ and} \\
&\langle T(S)^{\dagger}_{2Q}\rangle = 0.
\end{aligned} \tag{B.8}$$

The results presented in Eq. (B.8) have been compiled from Eqs. (4.3.14, 4.4.3b, and 4.4.4) in Ref. [18], Eq. (3) in Ref. [116], and this work.

B.2 Threshold polarizations for He 588 nm

For the helium $3\,{}^3\mathrm{D}_J \rightarrow 2\,{}^3\mathrm{P}_J$ transition, the fine structure is unresolved and there is no hyperfine depolarization due to the spinless nature of ^{4}He nuclei. Stokes parameters P_1, P_2, and $-P_3/P_e$ can be computed using $X = L = 2$, $X_f = L_f = 1$, $S = 1$ in Eq. (B.1) and the statistical tensors defined in Ref. [116], which are

$$\begin{aligned}\overline{\langle T(X)^{\dagger}_{KQ}\rangle} &= \overline{\langle T(L)^{\dagger}_{KQ}\rangle}\\ &= G_K\langle T(L)^{\dagger}_{KQ}\rangle + \sum_{K'=0,2} G^{0QQ}_{K'1K}\langle T(L)^{\dagger}_{K'0}\rangle\langle T(S)^{\dagger}_{1Q}\rangle,\end{aligned} \tag{B.9}$$

where

$$G_K = \frac{1}{2S+1}\sum_J (2J+1)^2 \begin{Bmatrix} L & J & S \\ J & L & K \end{Bmatrix}^2, \tag{B.10}$$

and

$$\begin{aligned}G^{0QQ}_{K'1K} &= (-1)^{L+S+Q}\sum_J (-1)^J (2J+1)^2\sqrt{3(2K'+1)(2K+1)}\\ &\quad\times \begin{pmatrix} K' & 1 & K \\ 0 & -Q & Q \end{pmatrix}\begin{Bmatrix} L & J & S \\ J & L & K \end{Bmatrix}\begin{Bmatrix} L & S & J \\ L & S & J \\ K' & 1 & K \end{Bmatrix}.\end{aligned} \tag{B.11}$$

The final {} brackets in Eq. (B.11) represent a Wigner 9-j symbol. This formalism is only a good approximation for cases where the unresolved fine-structure splitting is much greater than the natural linewidth, which in turn must be much greater than the hyperfine-structure splitting.

The resulting linear polarization P_1 (P_2 is found to be zero) is

$$P_1 = \frac{213(Q_0 + Q_1 - 2Q_2)}{671Q_0 + 1271Q_1 + 1058Q_2}, \tag{B.12}$$

where the $Q_{|M_L|}$ values refer to the excitation cross sections for individual magnetic sublevels. (Equation (B.12) is identical to that obtained by Percival and Seaton [6].) At threshold, only $M_L = 0$ states can be populated due to conservation of angular momentum. The initial total electron orbital angular momentum of the incoming electron and target ground state atom is zero with respect to the z-axis; thus the final angular momentum must also be zero. The "outgoing" electron has vanishingly small kinetic energy at threshold, and thus no angular momentum about the z-axis. This permits only one nonzero magnetic sub-level excitation cross section at threshold: Q_0. Setting $Q_1 = Q_2 = 0$ in Eq. (B.12) gives the threshold value of linear polarization

$$P_{1\text{thr}} = \frac{213}{671} \approx 0.317. \tag{B.13}$$

The spin-normalized circular polarization can be calculated and expressed in terms of the linear polarization P_1 as

$$-\frac{P_3}{P_e} = \frac{11}{36}\left[1 - \left(\frac{1981}{2343}\right)P_1\right] \approx 0.306(1 - 0.845P_1). \tag{B.14}$$

Inserting Eq. (B.13) into Eq. (B.14) yields the threshold circular polarization fraction

$$-\frac{P_{3\text{thr}}}{P_e} = \frac{150}{671} \approx 0.224. \tag{B.15}$$

The polarizations given by Eqs. (B.12) and (B.14) generally do not represent the experimentally observed values due to cascade contributions from higher lying states, except near threshold where the energy of the incoming electrons is below the excitation thresholds for such higher-lying states.

B.3 Threshold polarizations for H (and D) 656 nm

For the $n = 3 \rightarrow 2$ transitions in atomic hydrogen, the fine structure is not optically resolved (similar to the above case for helium). Also, light from three different multiplets is detected (3s–2p, 3p–2s, and 3d–2p). The situation is further complicated because of the non-zero nuclear spin ($I = \frac{1}{2}$ for H and $I = 1$ for D), which causes hyperfine depolarization. For the 3p state in hydrogen, the hyperfine splitting is slightly less than the linewidth [6]. If the splitting were much smaller than the linewidth, hyperfine depolarization could strictly be neglected [18]. The physical meaning of this situation is that the precession timescale of I and J about F is much shorter than the lifetime of the state, so the effects of hyperfine depolarization are not observed. For the actual intermediate case in hydrogen where the hyperfine splitting and linewidth are of the same order, a more detailed calculation is strictly required [18, 117]. However, as pointed out by McConkey [118], the relative error of the linear polarization due to this neglecting of the hyperfine depolarization is small for the 3p–2s multiplet (1.8% as given by Percival and Seaton [6]). For this reason, McConkey neglected the hyperfine structure for all multiplets when considering the linear polarizaiton of Balmer-α fluorescence. For simplicity, hyperfine depolarization is also neglected here, but it should be remembered that some small error will be incurred by doing so. Since these calculations are only being used in a qualitative manner, this approximation seems acceptable. Due to this simplification, the formalism in Sec. B.2 can be applied here separately for each multiplet (L=0,1,2). The resulting polarizations for the 3s–2p multiplet are all zero, and P_2 is found to be zero for the 3p–2s and 3d–2p multiplets as well. For the 3p–2s multiplet, the linear polarization P_1 is

$$P_1 = \frac{3(Q_0 - Q_1)}{7Q_0 + 11Q_1}, \text{ and } P_{1\text{thr}} = \frac{3}{7} \approx 0.429. \tag{B.16}$$

For the circular polarization,

$$-\frac{P_3}{P_e} = \frac{4}{9}\left[1 - \left(\frac{5}{6}\right)P_1\right] \approx 0.444(1 - 0.833P_1), \text{ and } -\frac{P_{3\text{thr}}}{P_e} = \frac{2}{7} \approx 0.286. \tag{B.17}$$

Consideration of the 3d–2p multiplet gives the linear polarization

$$P_1 = \frac{57\sqrt{2}(Q_0 + Q_1 - 2Q_2)}{238Q_0 + 438Q_1 + 324Q_2}, \text{ and } P_{1\text{thr}} = \frac{57\sqrt{2}}{238} \approx 0.339, \tag{B.18}$$

and the circular polarization is

$$-\frac{P_3}{P_e} = \frac{6}{25}\left[1 - \left(\frac{2\sqrt{2}(47 - 25\sqrt{3})}{57}\right)P_1\right] \approx 0.240(1 - 0.184P_1), \text{ and}$$
$$-\frac{P_{3\text{thr}}}{P_e} = \frac{6(2\sqrt{3}+1)}{119} \approx 0.225. \tag{B.19}$$

In order to obtain the observed polarizations, the polarizations for the individual multiplets must be combined. Adding Stokes vectors gives the relation

$$P_i = \frac{I_{(3p-2s)}P_{i(3p-2s)} + I_{(3d-2p)}P_{i(3d-2p)}}{I_{(3s-3p)} + I_{(3p-2s)} + I_{(3d-2p)}}. \tag{B.20}$$

Using the intensities (obtained from Fig. 5 of Ref. [69]) $I_{(3s-2p)} \approx 28.9$, $I_{(3p-2s)} \approx 4.91$, and $I_{(3d-2p)} \approx 24.0$, the polarizations for Hα radiation at threshold may be expected to be

$$P_{1\text{thr}} \approx 0.177, \tag{B.21}$$

and

$$-\frac{P_{3\text{thr}}}{P_e} \approx 0.118. \tag{B.22}$$

B.4 Threshold polarizations for N 824 nm

For the ${}^4P_{3/2} \rightarrow {}^4P_{5/2}$ transition in atomic N, expressions for P_1, P_2, and $-P_3/P_e$ can be obtained using the formalism described in Refs. [15, 27]. For this transition, the fine structure is resolved but there is depolarization due to the hyperfine interaction (the nuclear spin of ^{14}N is $I=1$). The relevant statistical tensors for this case are ($X=J=\frac{3}{2}$, $X_f=J_f=\frac{5}{2}$, $L=1$, $S=\frac{3}{2}$)

$$\begin{aligned}\langle\overline{T(X)^\dagger_{KQ}}\rangle &= \langle\overline{T(J)^\dagger_{KQ}}\rangle \\ &= G^I_K(J)\sum_{K'=0,2}\sqrt{(2K'+1)(2Q+1)(2J+1)}\,(K'0QQ|KQ) \\ &\quad\times\begin{Bmatrix}K' & Q & K\\ L & S & J\\ L & S & J\end{Bmatrix}\langle T(L)^\dagger_{K'0}\rangle\langle T(S)^\dagger_{QQ}\rangle,\end{aligned}\tag{B.23}$$

where

$$G^I_K(J)=\frac{1}{\gamma}\frac{1}{2I+1}\sum_F(2F+1)^2\begin{Bmatrix}J & F & I\\ F & J & K\end{Bmatrix}^2,\tag{B.24}$$

and the $(K'0QQ|KQ)$ Clebsch-Gordon coefficient is related to the 3-j symbol by

$$(K'0QQ|KQ)=\sqrt{2K+1}\begin{pmatrix}K' & Q & K\\ 0 & Q & -Q\end{pmatrix}.\tag{B.25}$$

The resulting linear polarization P_1 (P_2 is found to be zero) is

$$P_1=-\frac{66\sqrt{3}(Q_0-Q_1)}{1853Q_0+3772Q_1},\ \text{and}\ P_{1\text{thr}}=-\frac{66\sqrt{3}}{1853}\approx-0.0617.\tag{B.26}$$

The spin-normalized circular polarization expressed in terms of the linear polarization

P_1 is then given by

$$-\frac{P_3}{P_e} = -\frac{5137}{20250}\left[1 - \left(\frac{6254\sqrt{3}}{1089}\right)P_1\right] \approx -0.254(1 + 9.95P_1), \text{ and}$$
$$-\frac{P_{3\mathrm{thr}}}{P_e} = -\frac{3269}{33354} \approx -0.0980. \tag{B.27}$$

B.5 Threshold polarizations for N_2^+ $R(0)$ and $P(2)$ lines

The expressions for atomic polarizations are not generally applicable to molecular targets. However, there do appear to be special cases for which polarizations can be computed for molecular transitions using Eq. (B.1). Due to the similarity between the angular momentum coupling in atoms with that of molecular Σ states (compare Fig. 1.1a with Fig. 1.1b), it appears that the substitution $N \to L$ can be made. The conservation of orbital (or, in this case, rotational) angular momentum in initial and excited states at threshold must still be satisfied. In order to ensure that the sublevel cross section Q_0 is the only non-zero contributor at threshold, the application of the atomic equations is limited to the case where the ground molecular state has $J = N = 0$ (this restriction then guarantees that $M_N = 0$ in the excited state). Thus, the excitation process N_2^+ $X\,{}^1\Sigma_g^+(N=0) \to B\,{}^2\Sigma_u^+(N=1)$ is considered. Upon subsequent fluorescence, the excited state can either decay to the $X\,{}^2\Sigma_g^+(N=0)$ state via an $R(0)$ transition, or to the $X\,{}^2\Sigma_g^+(N=2)$ state via a $P(2)$ transition. These two cases can be treated using the formalism for unresolved fine-structure detailed in Sec. B.2 (in the excited state, $J = \frac{1}{2}, \frac{3}{2}$). Hyperfine depolarization will be ignored here for simplicity (the total combined nuclear spin T for the case of ortho N_2 is either 0 or 2). The $R(0)$ polarizations are then identical to the 3p–2s treatment of atomic hydrogen (see Sec. B.3), so Eqs. (B.16) and (B.17) are reproduced here. For the linear polarization P_1 ($P_2 = 0$),

$$P_1 = \frac{3(Q_0 - Q_1)}{7Q_0 + 11Q_1}, \text{ and } P_{1\text{thr}} = \frac{3}{7} \approx 0.429. \tag{B.28}$$

For the circular polarization,

$$-\frac{P_3}{P_e} = \frac{4}{9}\left[1 - \left(\frac{5}{6}\right)P_1\right] \approx 0.444(1 - 0.833P_1), \text{ and } -\frac{P_{3\text{thr}}}{P_e} = \frac{2}{7} \approx 0.286. \tag{B.29}$$

Additional calculation for the $P(2)$ transition (with the substitution $N \rightarrow L$) then yields

$$P_1 = \frac{3(Q_0 - Q_1)}{61Q_0 + 119Q_1}, \text{ and } P_{1\text{thr}} = \frac{3}{61} \approx 0.0492. \tag{B.30}$$

The linear polarization P_2 is zero as usual and the circular polarization is found to be

$$-\frac{P_3}{P_e} = -\frac{2}{9}\left[1 - \left(\frac{16}{3}\right)P_1\right] \approx -0.222(1 - 5.33P_1), \text{ and } -\frac{P_{3\text{thr}}}{P_e} = -\frac{10}{61} \approx -0.164. \tag{B.31}$$

Comparison of Eqs. (B.29) and (B.31) shows that the threshold circular polarizations for the R and P branches are of opposite sign.

References

[1] J. W. Maseberg and T. J. Gay, J. Phys. B **39**, 4861 (2006).

[2] J. W. Maseberg, J. Opt. Soc. Am. B **25**, 680 (2008).

[3] J. W. Maseberg and T. J. Gay, Phys. Rev. A **79**, 022705 (2009).

[4] J. B. Boffard, R. O. Jung, L. W. Anderson, and C. C. Lin, Adv. Atom. Mol. Opt. Phys. **54**, 319 (2006).

[5] D. W. O. Heddle and J. W. Gallagher, Rev. Mod. Phys. **61**, 221 (1989).

[6] I. C. Percival and M. J. Seaton, Phil. Trans. R. Soc. A **251**, 113 (1958).

[7] K. Bartschat and K. Blum, Z. Phys. A **304**, 85 (1982).

[8] J. Kessler, *Polarized Electrons*, 2nd ed. (Springer-Verlag, Berlin, 1985).

[9] N. Andersen and K. Bartschat, *Polarization, Alignment, and Orientation in Atomic Collisions*, (AIP Press, Springer-Verlag, New York, 2001).

[10] P. S. Farago and J. S. Wykes, J. Phys. B **2**, 747 (1969).

[11] J. Wykes, J. Phys. B **4**, L91 (1971).

[12] M. Eminyan and G. Lampel, Phys. Rev. Lett. **45**, 1171 (1980).

[13] K. Bartschat, K. Blum, G. F. Hanne, and J. Kessler, J. Phys. B **14**, 3761 (1981).

[14] T. J. Gay, J. Phys. B **16**, L553 (1983).

[15] J. E. Furst, W. M. K. P. Wijayaratna, D. H. Madison, and T. J. Gay, Phys. Rev. A **47**, 3775 (1993).

[16] T. J. Gay, J. E. Furst, K. W. Trantham, and W. M. K. P. Wijayaratna, Phys. Rev. A **53**, 1623 (1996).

[17] J. E. Furst, T. J. Gay, W. M. K. P. Wijayaratna, K. Bartschat, H. Geesmann, M. A. Khakoo, and D. H. Madison, J. Phys. B **25**, 1089 (1992).

[18] K. Blum, *Density Matrix Theory and Applications*, 2nd ed. (Plenum, New York, 1996).

[19] G. F. Hanne, in *Novel Aspects of Electron-Molecule Collisions*, edited by K. Becker (World Scientific, Singapore, 1998); C. Mette *et al.*, Verh. Dtsch. Phys. Ges. (IV) **29**, 462 (1994), obtained data via private communication.

[20] A. S. Green, G. A. Gallup, M. A. Rosenberry, and T. J. Gay, Phys. Rev. Lett. **92**, 093201 (2004).

[21] J. F. Williams and D. F. Yu, Phys. Rev. Lett. **93**, 073201 (2004).

[22] B. H. Bransden and C. J. Joachain, *Physics of Atoms and Molecules*, 2nd ed. (Prentice Hall, 2003).

[23] G. Herzberg, *Molecular Spectra and Molecular Structure I. Spectra of Diatomic Molecules*, 2nd ed. (D. Van Nostrand Company, Inc., Princeton, New Jersey, 1967).

[24] H. M. Al-Khateeb, Ph.D. thesis, University of Nebraska-Lincoln (2000).

[25] B. G. Birdsey, Ph.D. thesis, University of Nebraska-Lincoln (2003).

[26] H. M. Al-Khateeb, B. G. Birdsey, T. C. Bowen, A. S. Green, M. E. Johnston, and T. J. Gay, Rev. Sci. Instrum. **70**, 3882 (1999).

[27] K. P. Wijayaratna, Ph.D. thesis, University of Missouri-Rolla (1993).

[28] D. T. Pierce *et al.*, Rev. Sci. Instrum. **51**, 478 (1980).

[29] F. C. Tang, M. S. Lubell, K. Rubin, A. Vasilakis, M. Eminyan, and J. Slevin, Rev. Sci. Instrum. **57**, 3004 (1986).

[30] B. Birdsey *et al.*, Phys. Rev. A **60**, 1046 (1999).

[31] C. K. Sinclair *et al.*, Phys. Rev. ST Accel. Beams **10**, 023501 (2007).

[32] T. Kaisheng, Journal of Electronics (China) **5**, 53 (1988).

[33] M. Baylac *et al.*, Phys. Rev. ST Accel. Beams **8**, 123501 (2005).

[34] C. Karolis and E. Harting, J. Phys. B **11**, 357 (1988).

[35] J. D. Ingle, Jr., and S. R. Crouch, Anal. Chem. **44**, 777 (1972).

[36] R. M. A. Azzam and N. M. Bashara, *Ellipsometry and Polarized Light*, (North Holland, 1989).

[37] J. M. Daniels, Rev. Sci. Instrum., **57**, 1570 (1986).

[38] H. G. Berry, G. Gabrielse, and A. E. Livingston, Appl. Opt. **16**, 3200 (1977).

[39] P. C. Logofătu, Opt. Eng. **41**, 3316 (2002).

[40] B. L. Moiseiwitsch and S. J. Smith, Rev. Mod. Phys. **40**, 238 (1968); B. L. Moiseiwitsch and S. J. Smith, Rev. Mod. Phys. **41**, 574 (1969).

[41] P. N. Clout and D. W. O. Heddle, J. Opt. Soc. Am. **59**, 715 (1969).

[42] L. J. Curtis, *Atomic Structure and Lifetimes: A Conceptual Approach*, (Cambridge, 2003).

[43] C. H. Greene and R. N. Zare, Ann. Rev. Phys. Chem. **33**, 119 (1982).

[44] V. J. Ehlers and A. Gallagher, Phys. Rev. A **7**, 1573 (1973); V. J. Ehlers and A. Gallagher, Phys. Rev. A **9**, 1026 (1974).

[45] I. Humphrey, Meas. Sci. Technol. **10**, 403 (1999).

[46] P. R. Bevington, *Data Reduction and Error Analysis*, 3rd ed. (McGraw-Hill, Boston, 2003).

[47] C. E. Kuyatt, J. A. Simpson, and S. R. Mielczarek, Phys. Rev. **138**, A385 (1965).

[48] U. Fano and J. W. Cooper, Phys. Rev. **138**, A400 (1965).

[49] K. W. Trantham, M. Jacka, A. R. P. Rau, and S. J. Buckman, J. Phys. B **32**, 815 (1999).

[50] C. A. Nicolaides and N. A. Piangos, Phys. Rev. A **64**, 052505 (2001).

[51] P. J. Hicks, S. Cvejanović, J. Comer, J. M. Read, and J. M. Sharp, Vacuum **24**, 573 (1974).

[52] D. Roy, Phys. Rev. Lett. **38**, 1062 (1977).

[53] M. Bylicki and C. A. Nicolaides, Phys. Rev. A **51**, 204 (1995).

[54] S. J. Buckman and C. W. Clark, Rev. Mod. Phys. **66**, 539 (1994).

[55] A. Defrance and G. de Froment, Proc. 10th Int. Conf. on Physics of Electronic and Atomic Collisions **2**, 692 (1977).

[56] A. Defrance, J. Phys. B **13**, 1229 (1980).

[57] P. J. M. van der Burgt, J. van Eck, and H. G. M. Heideman, J. Phys. B **19**, 2015 (1986).

[58] H. Batelaan, J. van Eck, and H. G. M. Heideman, J. Phys. B **24**, 5151 (1991).

[59] D. Cvejanović, K. Clague, D. Fursa, K. Bartschat, I. Bray, and A. Crowe, J. Phys. B **33**, 2265 (2000); A. Crowe, personal communication to obtain data with corrected energy scale (2006).

[60] U. Fano and J. W. Cooper, Phys. Rev. **137**, A1364 (1965).

[61] U. Fano, Phys. Rev. **124**, 1866 (1961).

[62] J. Jimenez-Mier, J. Quant. Spectrosc. Radiat. **51**, 741 (1994).

[63] D. W. O. Heddle, R. G. W. Keesing, and A. Parkin, Proc. R. Soc. Lond. A **352**, 419 (1977).

[64] R. J. Van Brunt and R. N. Zare, J. Chem. Phys. **48**, 4304 (1968).

[65] D. A. Vroom and F. J. de Heer, J. Chem. Phys. **50**, 580 (1969).

[66] G. A. Khayrallah, Phys. Rev. A **13**, 1989 (1976).

[67] Y. P. Zhang, C. H. Cheng, J. T. Kim, J. Stanojevic, and E. E. Eyler, Phys. Rev. Lett. **92**, 203003 (2004).

[68] M. Glass-Maujean, J. Phys. B **11**, 431 (1978).

[69] W. Kedzierski, A. Abdellatif, J. W. McConkey, K. Bartschat, D. V. Fursa, and I. Bray, J. Phys. B **34**, 3367 (2001).

[70] S. L. Guberman, J. Chem. Phys. **78**, 1404 (1983).

[71] U. Fantz and D. Wünderlich, At. Data Nucl. Data Tables **92**, 853 (2006).

[72] N. Kouchi, M. Ukai, and Y. Hatano, J. Phys. B **30**, 2319 (1997).

[73] J. D. Bozek *et al.*, J. Phys. B **39**, 4871 (2006).

[74] A. P. Clark, M. Brouard, F. Quadrini and C. Vallance, Phys. Chem. Chem. Phys. **8**, 5591 (2006).

[75] D. H. Yu, J. F. Williams, X. J. Chen, P. A. Hayes, K. Bartschat, and V. Zeman, Phys. Rev. A **67**, 032707 (2003).

[76] X. Tang, Y. Hou, C. Y. Ng, and B. Ruscic, J. Chem. Phys. **123**, 074330 (2005).

[77] R. W. B. Pearse and A. G. Gaydon, *The Identification of Molecular Spectra*, 4th ed. (Wiley, New York, 1976).

[78] G. H. Dieke, J. Mol. Spectrosc. **2**, 494 (1958).

[79] H. M. Crosswhite, *The Hydrogen Molecule Wavelength Tables of G. H. Dieke*, (Wiley Interscience, New York, 1972).

[80] R. S. Freund, J. A. Schiavone, and H. M. Crosswhite, J. Phys. Chem. Ref. Data **14**, 235 (1985).

[81] A. Aguilar, J. M. Ajello, R. S. Mangina, G. K. James, H. Abgrall, and E. Roueff, ApJS **177**, 388 (2008); obtained data via private communication with Messrs. Aguilar and Ajello.

[82] B. P. Lavrov and I. S. Umrikhin, J. Phys. B **41**, 105103 (2008).

[83] G. R. Möhlmann and F. J. de Heer, Chem. Phys. Lett. **43**, 240 (1976).

[84] P. Baltayan and O. Nedelec, J. Physique **36**, 125 (1975).

[85] G. D. Meneses, L. M. Brescansin, M. T. Lee, S. E. Michelin, L. E. Machado, and C. Csanak, Phys. Rev. A **52**, 404 (1995).

[86] P. Cahill, R. Schwartz, and A. N. Jette, Phys. Rev. Lett. **19**, 283 (1967).

[87] J. W. McConkey, S. Trajmar, J. C. Nickel, and G. Csanak, J. Phys. B **19**, 2377 (1986).

[88] K. Blum and H. Jakubowicz, J. Phys. B **11**, 909 (1978).

[89] H. W. Dassen and J. W. McConkey, J. Phys. B **14**, 3777 (1981).

[90] J. W. McConkey, S. Trajmar, J. C. Nickel, and R. McAdams, J. Phys. B **18**, L207 (1985).

[91] X. Bingjia, S. Kado, S, Kajita, D. Yamasaki, and S. Tanaka, Plasma Sci. Technol. **7**, 2773 (2005).

[92] K. Becker, H. W. Dassen, and J. W. McConkey, J. Phys. B **16**, L177 (1983).

[93] G. Hartmann and P. C. Johnson, J. Phys. B **11**, 1597 (1978).

[94] F. Roux, F. Michaud, and M. Vervloet, J. Mol. Spectrosc. **158**, 270 (1993).

[95] F. Roux, F. Michaud, and M. Vervloet, Can. J. Phys. **67**, 143 (1989).

[96] G. F. Hanne, private communication (2005).

[97] E. A. Colbourn and A. E. Douglas, J. Mol. Spectrosc. **65**, 332 (1977).

[98] H. Schmoranzer, P. Hartmetz, D. Marger, and J. Dudda, J. Phys. B **22**, 1761 (1989).

[99] J. H. Van Vleck, Phys. Rev. **33**, 477 (1929).

[100] S. Green and R. N. Zare, J. Mol. Spectrosc. **64**, 217 (1977).

[101] C. H. Townes and A. L. Schawlow, *Microwave Spectroscopy*, (Dover, New York, 1975).

[102] C. J. Erickson, D. Levron, and W. Happer, Phys. Rev. Lett. **85**, 4237 (2000).

[103] R. A. Bernheim, J. Chem. Phys. **36**, 135 (1962).

[104] W. W. Hunter Jr., Ph.D. thesis, The College of William and Mary in Virginia (1965); NASA Report No. NASA-TM-X-66993.

[105] D. H. Crandall, W. E. Kauppila, R. A. Phaneuf, P. O. Taylor, and G. H. Dunn, Phys. Rev. A **9**, 2545 (1974).

[106] Wm. B. Peatman, B. Gotchev, P. Gürtler, E. E. Koch, and V. Saile, J. Chem. Phys. **65**, 2089 (1978).

[107] J. T. Fons, J. S. Allen, R. S. Schappe, and C. C. Lin, Phys. Rev. A **49**, 927 (1994).

[108] I. C. Malcolm, H. W. Dassen, and J. W. McConkey, J. Phys. B **12**, 1003 (1979).

[109] J. A. Guest, K. H. Jackson, and R. N. Zare, Phys. Rev. A **28**, 2217 (1983).

[110] P. Cangiano, M. de Angelis, L. Gianfrani, G. Pesce, and A. Sasso, Phys. Rev. A **50**, 1082 (1994).

[111] F. Roux, F. Michaud, and J. Verges, J. Mol. Spectrosc. **97**, 253 (1983).

[112] G. H. Dieke and D. F. Heath, Johns Hopkins Spectroscopic Report 17 (1959).

[113] P. Nolan and F. A. Jenkins, Phys. Rev. **50**, 943 (1936).

[114] I. Kovacs, *Rotational Structure in the Spectra of Diatomic Molecules*, (American Elsevier, New York, 1969).

[115] P. N. Stanton and R. M. St. John, J. Opt. Soc. Am. **59**, 252 (1969).

[116] T. Fischer and J. Kessler, Rev. Sci. Instrum. **66**, 4885 (1995).

[117] U. Fano and J. H. Macek, Rev. Mod. Phys. **45**, 553 (1973).

[118] J. W. McConkey, J. Phys. B **21**, L317 (1988).